ABSTRACT

Title of Dissertation: INVESTIGATING THE X-RAY TEMPORAL AND SPECTRAL PROPERTIES OF BLAZARS AND BEAMED AGN IN THE SWIFT-BAT HARD X-RAY SURVEY

Sergio A. Mundo
Doctor of Philosophy, 2023

Dissertation Directed by: Professor Richard Mushotzky
Department of Astronomy

Blazars are generally known to exhibit high-amplitude, rapid variations in flux, polarization, and in their spectra across most timescales and wavelengths. While the consensus for these objects is that their emission is indeed "highly variable", a more specific characterization of the variability may depend on the timescales considered. In this dissertation, I investigate the nature of the variability of these objects and the physical processes involved in producing it, through the lens of blazars that have been detected by the *Swift* Burst Alert Telescope.

My foray into the high-energy astrophysics of blazars begins with a case study of a blazar-like AGN. For the first time for this source, I definitively measure X-ray reflection features and help determine the origin of its broadband X-ray emission, suggesting that the X-rays from this object predominantly come from regions in the vicinity of the black hole, while also finding evidence of jetted emission in the hard X-rays. I further explore blazar X-ray emission by investigating the rest of the blazars in the *Swift*-BAT survey, and in doing so I conduct the first study

in the time domain dedicated to the hard X-ray variability behavior of blazars on long timescales based on $\sim$13 years of continuous X-ray data in the 14-195 keV band. In this study, I find that a significant portion of the blazars in the sample ($\sim$37%) do not show statistically significant variability on monthly timescales, which is in tension with the expected high variability of blazars seen in previous studies. In addition, I show that for some of the brightest blazars, the long-term spectra in the hard X-rays may be described in a relatively simple way, with a power law that changes slope on monthly timescales.

Since the BAT data are not sensitive to changes on shorter timescales, or to low-amplitude variability on monthly timescales, I follow up on the supposedly "non-variable" blazars from the previous investigation by using recent *NICER* observations of a sub-sample of 4 such "quiescent" BAT blazars over 5 months, allowing for insight into the short-timescale and lower amplitude variability while also representing some of the longer timescales sampled by the BAT survey. I show that variations in the *NICER* band are in fact detected on several timescales, but that the fractional variability appears to decrease with longer timescales, implying generally low-amplitude variability across all sources and showing very low variability on monthly timescales, which is once again at odds with studies that have shown that blazars are highly variable in the X-rays on a wide range of timescales. I also show through a spectral analysis that the broadband X-ray spectra (0.3-195 keV) of these sources can be described with different power law models, with one source requiring significant absorption in the soft X-rays to fully describe its observed curvature, possibly due to absorption in the intergalactic medium. Additional observations from a new follow-up *NICER* campaign will further facilitate probing the variability of these BAT blazars for up to timescales of a year, serving as an additional stepping stone towards our ultimate goal of characterizing the X-ray variability of blazars and beamed AGN.

INVESTIGATING THE X-RAY TEMPORAL AND SPECTRAL PROPERTIES OF BLAZARS AND BEAMED AGN IN THE SWIFT-BAT HARD X-RAY SURVEY

by

Sergio A. Mundo

Dissertation submitted to the Faculty of the Graduate School of the
University of Maryland, College Park in partial fulfillment
of the requirements for the degree of
Doctor of Philosophy
2023

Advisory Committee:
Professor Richard Mushotzky, Chair/Advisor
Dr. Brad Cenko
Professor Lee Mundy
Dr. Bindu Rani. External Examiner
Professor Gregory Sullivan, Dean's Representative

Preface

The work presented in Chapters 2-4 of this dissertation has either been published or submitted for publication in the Monthly Notices of the Royal Astronomical Society (MNRAS) and has been minimally modified from the original versions for this thesis. The chapters correspond to the following papers:

- Chapter 2: S.A. **Mundo**, E. Kara, E.M. Cackett et al., "The origin of X-ray emission in the gamma-ray emitting narrow-line Seyfert 1 1H 0323+342", *MNRAS* 496, 2922–2931 (2020).

- Chapter 3: S.A. **Mundo** & R. Mushotzky. "Long-term hard X-ray variability properties of *Swift*-BAT blazars", *submitted to MNRAS*.

- Chapter 4: S.A. **Mundo** & R. Mushotzky, "Investigating the variability of *Swift*-BAT blazars with *NICER*", *MNRAS* 520, 1044–1054 (2023).

The contents of this dissertation follow a logical order that reflects the progression of my research over the years. My work as a graduate student began with a case study of a peculiar blazar-like AGN that aimed to pinpoint the origin and nature of the broadband X-ray emission from this source. This project piqued my interest in beamed AGN, and from there, my research evolved into studying a significantly higher number of blazars from the *Swift*-BAT hard X-ray survey simultaneously, with a focus on the X-ray variability of these objects on longer timescales.

This dissertation builds on the extensive research that has been conducted on blazars and AGN in the past, while also providing a few novel methods and insights to help characterize the X-ray emission from these objects.

Dedication

Le dedico esta tesis a mi familia, cuya presencia ha brillado aún más que un núcleo galáctico.

Acknowledgments

This dissertation represents the culmination of a long, difficult journey as an astronomy and astrophysics Ph.D. student at the University of Maryland. I owe my gratitude to a number of people, without whom this work would not have been possible.

First and foremost, I would like to thank my advisor, Professor Richard Mushotzky, for his invaluable guidance and mentorship. Through his insight, I have been able to refine my research abilities and have learned to ask the right science questions relevant to our field. He has also taught me to find joy in the prospect of new results and discoveries while working on challenging and interesting projects over the years. In addition, he was extremely understanding when times were tough for me, and he has demonstrated that he cares about the well-being and success of his students. It has truly been an honor and a privilege to work with him these past few years.

I would also like to thank my first mentor at the University of Maryland, Professor Erin Kara. She introduced me to research on AGN, and her palpable excitement for this sub-field inspired in me a passion for the high-energy astrophysics studied in these objects. Her guidance during my first two years of graduate school was instrumental in my early development as a scientist, and helped make me the researcher I am today. It was a pleasure to work with such a brilliant scientist and human being, and I will forever be grateful for her mentorship. In addition, I owe my gratitude to Dr. Brad Cenko, Principal Investigator of the *Swift* Observatory, for providing funding when there were gaps in funding between my grants. Thanks are also in order for Dr. Cenko, Professor Sylvain Veilleux, Professor Lee Mundy, Dr. Bindu Rani, and Professor Gregory Sullivan for at one point or another agreeing to serve on my thesis committee, providing invaluable feedback, and taking the time to review my manuscript.

I must also thank the staff at the UMD Department of Astronomy for working tirelessly to make sure that we had the smoothest experience with administrative tasks, and in particular I'd like to thank Natalie Rowe, Susan Lehr, and Dorinda Kimbrell for their immense help when it came to setting up budgets for grants and navigating/completing travel forms. My graduate school experience would also not have been the same without the classmates in my cohort and the rest of the graduate student body, who upon starting the program, made me feel welcome at a time when I felt somewhat out of place in the field.

I would like to specifically thank two people who had major impacts on my time at UMD, Dr. Amy Steele and Dr. Sara Frederick. Amy, I am forever grateful that you took me under your wing and showed me the ropes of the department and of the field. Your wisdom and experience were unparalleled for a graduate student, and you have always been there for me as both a mentor and a friend, even during the times when I hit rock bottom; I would not have made it here without your unwavering support. Sara, the conversations and the bonding we shared as roommates were a major source of relief, comfort, laughter, and general happiness during a period when the coronavirus pandemic was at its absolute worst. Our friendship was still able to flourish during this time, and you (and Lumi) were somehow always able to bring a smile to my face at a time of "doom and gloom". Your advice and support over the past few years have been constant, and you kept believing in me even when I thought it was impossible to cross the finish line. I would not have come this far without you.

Finally, to my family, Papi, Mami, Diego y Abuela: Es difícil expresar con palabras cuánto

les debo. Abuela, gracias por siempre pensar en mí y por mandarme aguacates, platanutres, recetas y otras cosas a través de los años que me transportaban a mis raíces. Tu actitud positiva ha sido un apoyo enorme y me ha dado ánimo para seguir adelante.

Diego, además de ser mi hermano y mi mejor amigo, también eres un ejemplo a seguir. Siempre me has defendido y siempre has estado a mi lado, hasta cuando yo te molestaba hace ya tantos años. Siempre aprendo tanto de ti, sea a través de nuestra música o de nuestras conversaciones. Gracias por ser un hermano tan especial y por apoyarme en todo momento.

Mientras escribía esta sección, me puse a pensar en aquel nenito rubio que a veces decía: "quiero ser abogado como Papi", y en lo equivocado que estaba. Papi y Mami, desde chiquito ustedes me enseñaron que uno no siempre tiene que ser abogado o médico y me motivaron a explorar otras disciplinas. Pero el mensaje más importante que me han transmitido acerca de todo esto también ha sido el más simple: "busca algo que disfrutes". Esa búsqueda no ha tenido una trayectoria perfecta, y he sufrido bastante, pero creo que ahora sí puedo decir con certeza que, aun si no continúo en astrofísica, me da alegría ser científico. Gracias por ser mi guía a lo largo de los años y por su paciencia infinita, sus consejos y su amor. Esta tesis también les pertenece a ustedes.

Table of Contents

List of Tables

List of Figures

List of Abbreviations

AGN	Active galactic nucleus/nuclei
BAT	Burst Alert Telescope
BL Lac	BL Lacertae
BLR	Broad line region
CCD	Charged-coupled device
EC	External Compton
EW	Equivalent width
Fermi-LAT	*Fermi* Large Area Telescope
FPMA	Focal plane module A
FPMB	Focal plane module B
FSRQ	Flat-spectrum radio quasar
FWHM	Full width at half maximum
GRB	Gamma-ray burst
HEASOFT	High Energy Astrophysics Software
HSP	High-synchrotron peaked
ISP	Intermediate-synchrotron peaked
KS	Kolmogorov-Smirnov
LSP	Low-synchrotron peaked
NED	NASA/IPAC Extragalactic Database
NICER	Neutron Star Interior Composition Explorer
NLR	Narrow line region
NLS1	Narrow-line Seyfert 1
NuSTAR	Nuclear Spectroscopic Telescope Array

PSD	Power spectral density
QSO	Quasi-stellar object
RL	Radio-loud
RMS	Root-mean-square
RQ	Radio-quiet
SAS	Scientific Analysis System
SED	Spectral energy distribution
SSC	Synchrotron self-Compton
SIMBAD	Set of Identifications, Measurements and Bibliography for Astronomical Data
UV	Ultraviolet
WHIM	Warm-hot intergalactic medium
ZTF	Zwicky Transient Facility

Chapter 1: Introduction

Active galaxies provide some of the most interesting laboratories in the universe with which to study high-energy astrophysical phenomena. Over the decades, the powerful and variable multi-wavelength emission from these objects has shed light on not only the nature of the supermassive black holes hosted at their cores, but also on the behavior of the processes occurring in their surroundings and in the spaces between galaxies.

A small subset of active galaxies, known as blazars, produce strong jets of relativistic particles that are aimed close to our line of sight; these objects in particular have been known to exhibit some of the most luminous and variable emission in the universe, even when compared to other types of active galaxies. While the characterization of the behavior of this emission over time has often involved many investigations across different timescales, energy bands, and blazar types, it is not always straightforward to define the variability behavior in these objects, nor to identify the physical processes producing it. The overarching goal of my research has been to more specifically characterize the variability and the nature of the emission from blazars, with a particular focus on the hard X-ray emission from blazars that have been detected by the *Swift* Burst Alert Telescope (BAT).

This chapter begins with a review of active galactic nuclei and the properties of their emission, as well as an overview of the variable emission from blazars and the radiative processes associated with them. I then describe the Burst Alert Telescope aboard the *Swift* observatory and its archival data, which serve as a focal point for most of this thesis. The chapter closes with a thesis outline and a list of the software used for the research conducted.

The primary aim of this thesis is to study the X-ray temporal and spectral properties of the blazars that appear in the *Swift*-BAT catalog by analyzing the catalog data in tandem with data that was acquired from other X-ray observatories (e.g. *XMM-Newton*, *NuSTAR*, *NICER*), with an overall goal of better understanding the physical processes and mechanisms that may drive the X-ray emission in these objects, thus providing a small contribution to the already vast array of existing studies that have allowed us to grasp the complex nature of active galaxies and blazars.

1.1 Active Galactic Nuclei

Active galactic nuclei (AGN) are compact regions in the centers of galaxies that are the most powerful and persistent objects in the universe, emitting radiation across the entire electromagnetic spectrum with luminosities often far exceeding those of the emission from the rest of the host galaxy. AGN often exhibit large variations in their emission on timescales of minutes to years. These characteristics are widely considered to be intrinsic and to result from non-stellar processes, with the primary mechanism being the accretion of matter by a supermassive black hole ($\sim 10^6 - 10^9 M_\odot$) at the center of the host galaxy (Lynden-Bell 1969; Fabian 1979).

Observations of AGN have been accumulated at every wavelength since around the mid-20th century, contributing to the creation of the so-called unified model of AGN. This model consists of the aforementioned supermassive black hole as the central engine for the system, as well as an accretion disk encircling the black hole; the disk is itself surrounded by an obscuring

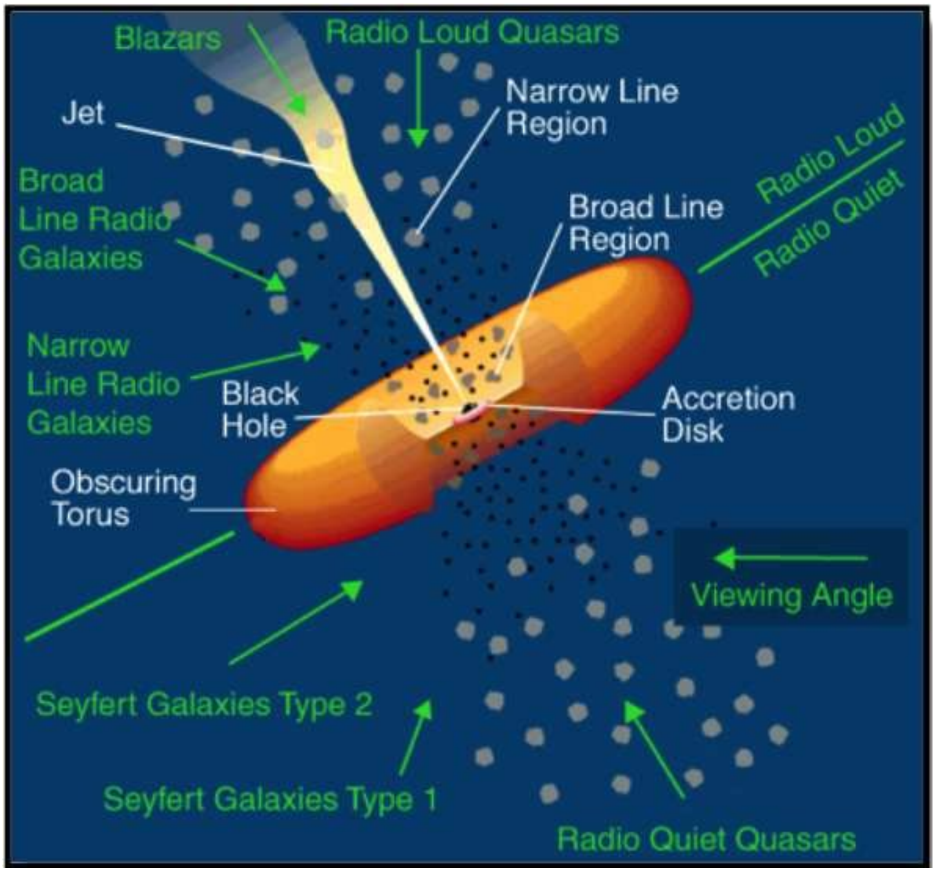

Figure 1.1: Schematic showing the different structures of AGN as well as terms used to describe AGN depending on the line of sight (based on Urry & Padovani 1995). The main focus of this thesis will be radio-loud AGN, specifically blazars.

dusty torus at the parsec scale. Thermal emission from the disk ionizes gas that orbits the black hole, and in turn the gas produces line emission at optical and ultraviolet (UV) wavelengths to form the broad line and narrow line regions (BLR and NLR, respectively; see Figure 1.1 for a schematic). Different types of AGN arise due to the angle at which the observer is viewing the system: if the system is seen face-on, the observer has direct access to the central regions and the vicinity of the black hole, whereas if the system is seen edge-on, these regions are instead obscured by the torus.

The innermost region of an AGN usually consists of a hot plasma, referred to as the corona, that lies above the accretion disk in the vicinity of the black hole and inverse-Compton scatters seed photons from the disk, resulting in a significant amount of continuum X-ray emission whose spectrum can be described with a power law of the form $N(E) \propto E^{-\Gamma}$, where $N(E)$ is the photon flux in units of photons s^{-1} cm^{-2} keV^{-1} and Γ is the photon index (or the "slope" of the spectrum on a logarithmic scale). Since, except for a few limited/nearby cases (Event Horizon Telescope Collaboration et al. 2019; Gravity Collaboration et al. 2018; GRAVITY Collaboration et al. 2020), the angular size of most AGN is too small to be spatially resolved, variability and timing studies have emerged over the past several decades as key tools that give insight into the different AGN components and the physical processes that power AGN. Time-domain and Fourier-based variability analyses in the X-ray band in particular have become almost synonymous with the study of AGN due to the fact that a significant fraction ($\sim$3-30%, Ho 1999) of the bolometric luminosity is comprised of X-ray emission (see e.g. Mushotzky et al. 1993; Ulrich et al. 1997; Vaughan et al. 2003; Uttley et al. 2014 for reviews).

While many AGN are essentially the same type of object viewed from different angles, there is in fact one major split in the classification of these sources. Roughly 10% of AGN exhibit collimated, relativistic jets that are launched along the poles of the black hole (perpendicular to the accretion disk) and which produce relatively strong non-thermal emission in the radio band. For this reason, these objects are called "radio-loud" (RL) AGN, as opposed to the more common "radio-quiet" (RQ) AGN. Astrophysical jets in AGN can reach the Mpc scale, meaning that they often extend well beyond the visible structure of the galaxy hosting the AGN. Significant jetted emission has been detected not only in the radio, but also in the optical, X-rays, and γ-rays (e.g. Butcher et al. 1980; Marshall et al. 2005; Abdo et al. 2010a). The emission from jets can therefore span the whole electromagnetic spectrum, even for a particular source at a time, providing a rich collection of resources with which to study the jet physics.

1.2 Blazars and Beamed AGN

When a relativistic jet is oriented close to the observer's line of sight, the RL AGN is termed a "beamed AGN" or "blazar"[1] (Urry & Padovani 1995). In this case, the jet moves towards the observer with a bulk relativistic speed $v = \beta c$, with an associated bulk Lorentz factor $\Gamma = (1-\beta^2)^{-0.5}$ and viewing angle θ. A few characteristics in blazars emerge as a direct result of this relativistic motion. Firstly, in the observer's frame, the relativistic particles in the jet will be seen as having a transverse apparent superluminal bulk speed $\beta_{\rm T} > 1$ because the emitter "catches up" with its own radiation. This transverse speed can be written as $\beta_{\rm T} = \beta \sin\theta/(1-\beta\cos\theta)$ (see e.g. Beckmann & Shrader 2012 for a derivation), with a maximum possible value of $\beta\Gamma$. The detection of superluminal motion in the radio emission from the jets of blazars and beamed AGN is one of the key components of RL AGN unification (Lister et al. 2013).

A second important characteristic of blazars arising from relativity is that the jetted emission is boosted along the direction of motion. As such, an observer will detect a broadband flux that is amplified to $F = \delta^4 F'$, where the primed quantity represents emission in the jet's co-moving frame and the Doppler factor δ is defined as $\delta = [\Gamma(1-\beta\cos\theta)]^{-1}$. Values for δ are usually on the order of $\sim$10-20, meaning that the boosted emission over a particular band-

[1]For the rest of this thesis, the terms "blazar" and "beamed AGN" will be used almost interchangeably, although it is important to note that not all beamed AGN necessarily show the same spectral characteristics as blazars.

pass is usually $\sim$10,000 times higher than in the frame of the jet. In addition to this, variability timescales are shortened in the observer's frame, with a characteristic timescale τ' in the jet frame being compressed to $(1+z)\tau'/\delta$, leading to relatively rapid variability in the frame of the observer. As a result, the emitted radiation from blazars, which is dominated by extreme non-thermal processes that take place in the jet, has historically been known to be very luminous, with high-amplitude, rapid variations in their flux, spectra, and polarization observed across most timescales and energy bands (see e.g. Stein et al., 1976; Blandford & Rees, 1978; Angel & Stockman, 1980; Marscher & Gear, 1985; Morini et al., 1986; Feigelson et al., 1986; Wagner & Witzel, 1995; Ulrich et al., 1997; Andruchow et al., 2005; Lichti et al., 2008; Soldi et al., 2014).

In general, blazars can be separated into two subclasses: BL Lacertae (BL Lac) objects and flat-spectrum radio quasars (FSRQs). This classification is usually based on the rest-frame equivalent width (EW) of the optical emission lines, with FSRQs showing broad lines with EW>5Å and BL Lacs showing weak or no emission lines in their spectra (Stickel et al., 1991). FSRQs and BL Lacs can also be identified through their broadband spectral energy distributions (SEDs). Blazar SEDs generally consist of a "double-hump" continuum that spans the entire electromagnetic spectrum and represents the nonthermal emission produced in the jet, with the hump at lower frequencies caused by synchrotron emission from the radio to the ultraviolet (UV)/X-rays and the hump at higher frequencies, i.e. X-rays to γ-rays, arising due to inverse Compton processes (see Figure 1.2 for examples). In BL Lacs, the two humps are usually nearly equally luminous, and the inverse Compton hump is likely due to the synchrotron self-Compton (SSC) mechanism, where the synchrotron photon field produced by the jet is Compton upscattered by the same highly energetic particles in the jet. For FSRQs, the inverse Compton hump is often significantly more luminous than the synchrotron hump, and is instead believed to be the product of inverse Compton scattering of photons external to the jet (the so-called "external Compton" (EC) process).

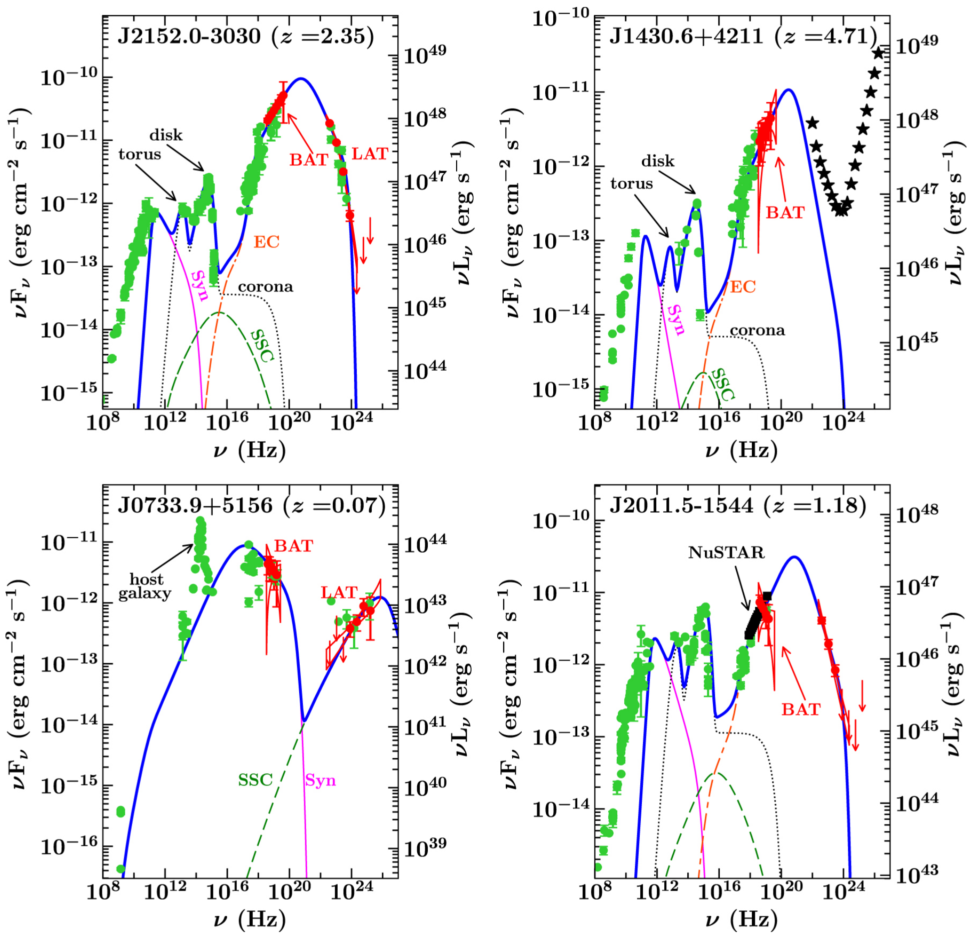

Figure 1.2: Examples of SEDs of blazars that appear in the *Swift*-BAT catalog, from Paliya et al. 2019b . Different components to the SED are shown: thermal emission from the torus, accretion disk, and the X-ray corona are represented with a black dotted line, while non-thermal emission from synchrotron, SSC, and EC processes is shown with the pink solid, green long dashed and orange dashed–dashed–dotted lines, respectively. The blue solid line represents the sum of the different types of radiation, i.e. the full SED of the blazar.

In addition, many FSRQs also show a third "bump" between the customary low-energy and high-energy humps in their SEDs, which is representative of thermal emission in the optical/UV that is not as dominant as the nonthermal emission and is associated with the accretion disk. This has led to a more physical distinction between BL Lacs and FSRQs, where the more luminous FSRQs likely exhibit radiatively efficient accretion; this forms a UV-bright disk that photo-ionizes the BLR, which in turn provides an external photon field that is upscattered by the jet (Ghisellini et al., 2009b, 2011)[2]. Based on the frequency of the peak of the synchrotron hump, $\nu_{\rm syn}^{\rm peak}$, FSRQs and BL Lacs can further be divided into "high-synchrotron-peaked" (HSP, $\nu_{\rm syn}^{\rm peak} \gtrsim 10^{15}$Hz); "intermediate-synchrotron-peaked" (ISP, $10^{14} \lesssim \nu_{\rm syn}^{\rm peak} \lesssim 10^{15}$Hz); and "low-synchrotron-peaked" (LSP, $\nu_{\rm syn}^{\rm peak} \lesssim 10^{14}$Hz; see e.g. Abdo et al. 2010b), with FSRQs usually classified as LSPs. With this classification in mind, Fossati et al. (1998) and Ghisellini et al. (2017) also observed that the bolometric luminosity gradually decreases with increasing $\nu_{\rm syn}^{\rm peak}$, i.e., as one goes from FSRQ/LSP to HSP. This anti-correlation was termed the "blazar sequence" and, if linked to a real physical property, could shed light on the physical processes that produce blazar SEDs.

When it comes to the production of the X-rays in particular, the emission mechanisms involved in BL Lacs and FSRQs can lead to differences in the nature of the variability for each type of blazar. For instance, the X-rays in BL Lacs are usually produced by either synchrotron emission or the SSC process (see e.g. Ghisellini et al. 2009b). In this case, the blazar's variability is likely driven by the timescale for the acceleration of particles in the jet as it compares to the timescale of energetic losses by those same particles through either synchrotron or inverse Compton processes. By contrast, as implied earlier, the X-rays in FSRQs are produced by the EC process, where the dominant radiation field corresponds to the photon density of an external component. The variability in these blazars could involve variations in an external photon field that scatters off a quasi-stable particle distribution. In addition, a number of blazars are termed

[2]This external Compton mechanism can also occur with external photon fields other than the one from the BLR, such as seed photons from the disk itself and infrared emission from the torus (see e.g. Ghisellini & Tavecchio 2009 for relevant modeling).

"off-axis" or "hybrid" blazars/AGN, in the sense that their jets are aligned at a higher angle than is customary ($\sim 10°$) to the observer's line of sight. In these blazars, the jetted X-ray emission resulting from the previously mentioned processes may be accompanied by another significant component that represents emission from the disk/corona originating in the vicinity of the black hole (see Section 1.1), which may include features indicative of a reprocessing of the coronal X-ray emission by the accretion disk; for this component, the variability would likely be driven by multiplicative processes associated with accretion rate fluctuations occurring in the disk. The implications that the aforementioned processes have on the characterization of the X-ray variability of blazar subclasses remain a major point of discussion, as differences between spectral components and between blazar types may provide insight into the physical mechanisms involved in driving the jetted emission.

In order to have a better understanding of the behavior of these different emission components and their contribution to blazar variability, it is useful to describe some of the basic emission mechanisms involved in these objects. The following subsection provides a brief overview of the main radiative processes in blazars and some associated quantities in some more detail, as well as the implications that these processes may have on the behavior of their emission.

1.2.1 Radiative Processes in Blazars

The basic idea behind the dominant emission from blazars is that a non-thermal population of highly energetic particles radiate photons over the entire electromagnetic spectrum. For simplicity, most blazar emission models usually assume leptonic radiative processes to describe the emission, where the radiation is associated with electrons and/or positrons in the jet radiating from a single, or “one-zone”, spherical emission region that covers the entire cross-section of the jet; this is the scenario that will be considered in this thesis. In this section, quantities are calculated in the jet’s co-moving frame.

Assuming a framework where these particles are efficiently accelerated in the jet, the simplest way to describe the electron injection function is as a power law distribution, namely

$$Q(\gamma') = Q_0 \gamma'^{-q} \ [\mathrm{s}^{-1}\mathrm{cm}^{-3}], \tag{1.1}$$

where Q_0 is a normalization constant, γ' is the Lorentz factor of the electrons in the co-moving frame (representing their energy), and q is the spectral index. Alternatively, the injection function may be described with a broken power law (see e.g. Ghisellini & Tavecchio 2009; Paliya et al. 2019b). The energy distribution $N(\gamma')$ of the particles, which will have the same form as $Q(\gamma')$, can be derived from the injection function by solving the continuity equation, with

$$N(\gamma') = \frac{\int_{\gamma'}^{\gamma'_{max}} [Q(\gamma') + P(\gamma')] d\gamma'}{\dot{\gamma'}} \ [\mathrm{cm}^{-3}], \tag{1.2}$$

where $\dot{\gamma'}$ represents the energy dissipation rate (i.e. the “cooling” rate) of an electron with energy γmc^2 and $P(\gamma')$ is a term representing electron-positron pairs, which is neglected for the purposes of this thesis. Due to the presence of a magnetic field B, this distribution of electrons then emits synchrotron radiation with average power $P_{\mathrm{syn}} = \frac{4}{3}\sigma_{\mathrm{T}} c U'_B \beta^2 \gamma'^2$ per electron, where if $\gamma'^2 \gg 1$, which is the case for highly relativistic electrons, the factor $\beta^2 = 1 - \gamma^{-2} \approx 1$ can be ignored.

As previously mentioned, these same electrons may also inverse Compton scatter the synchrotron photons through the SSC process, or they may upscatter radiation fields whose origins are external to the jet, such as thermal emission from the dusty torus, BLR, or accretion disk (including emission from the X-ray corona just above the disk). Averaging over the solid angle, the power dissipated per electron during inverse Compton scattering is $P_{\rm IC} = \frac{4}{3}\sigma_{\rm T} c U'_{\rm r} \beta^2 \gamma'^2$, where in this case $U'_{\rm r}$ is the energy density of the seed photon fields before scattering (e.g. $U'_{\rm syn}$ in the case of SSC, or for EC, $U'_{\rm d}$ for direct disk radiation, $U'_{\rm X}$ for emission from the X-ray corona, $U'_{\rm BLR}$ for emission from the BLR, or $U'_{\rm IR}$ for emission from the torus, or any combination of these; see e.g. Ghisellini & Tavecchio 2009 for a calculation of these densities). Using these quantities, as well as the characteristic dissipation timescale $\tau = \frac{E'}{dE'/dt}$, we can calculate the "cooling time" of the electrons for both synchrotron and inverse Compton processes, which yields

$$\tau_{\rm syn}(\gamma') = \frac{3 m_{\rm e} c}{4 \sigma_{\rm T} U'_B \gamma'} \tag{1.3}$$

and

$$\tau_{\rm IC}(\gamma') = \frac{3 m_{\rm e} c}{4 \sigma_{\rm T} U'_{\rm r} \gamma'}. \tag{1.4}$$

These timescales, when transformed into the frame of the observer, are extremely important when considering the variability timescales of the observed emission, and are often used as a basis for comparing with the observed timescales of the variability in order to determine whether the variability from a blazar may be due to radiative losses or other processes. As an example, we can consider the synchrotron regime, which for a particular source may produce emission from the radio band to the X-rays. From equations 1.3 and 1.4, the cooling timescales go as the inverse of γ', implying that electrons at higher energies would cool more rapidly. Emission in the X-rays would therefore involve cooling timescales that are considerably shorter than those for electrons producing the radio emission, suggesting that one would likely observe a significantly higher degree of variability in the X-rays, assuming it is dominated by radiative losses. In the case where the timescales of the detected variability do not match the cooling times, it is possible that the variability is governed by processes other than energetic losses, such as those associated with particle acceleration/injection or jet dynamics (e.g. shocks). The cooling timescales can therefore serve as a basic guide to provide insight into the physics producing the variable emission in blazars.

1.3 The *Swift*-BAT as a tool for studying the hard X-ray variability of blazars

This thesis focuses on probing the X-ray variability behavior of blazars and blazar-like AGN that appear in the archival database of the *Swift* Burst Alert Telescope. The BAT is a large field of view ($\sim 60^\circ \times 100^\circ$), coded-aperture imaging instrument that finds point sources by implementing a fast Fourier transform convolution of the coded aperture mask pattern with an array of detector rates, which effectively uses the shadow of the mask cast by a source onto the detector array to create a sky image. While its pointing system is optimized to detect transient gamma-ray bursts (GRBs) in the hard X-rays, it also continuously observes the sky, performing an all-sky hard X-ray survey with a median 5σ sensitivity corresponding to 7.24×10^{-12} erg s^{-1} cm^{-2} in the 14-195 keV band for the latest published survey (Oh et al. 2018), with the sensitivity of the latter in general scaling as the square root of the exposure time.

The reduction of the BAT data is similar across all updated surveys/catalogs (see e.g. Tueller et al. 2010; Baumgartner et al. 2013): data are extracted in eight energy bands (14–20 keV, 20–24 keV, 24–35 keV, 35–50 keV, 50–75 keV, 75–100 keV, 100–150 keV, and 150–195 keV) from a single snapshot image, and then the data from each snapshot are combined into all-sky mosaic images. Next, the eight-band mosaic images are combined to form a total-band map, and a blind search for sources in the 14-195 keV band images is performed with a 4.8σ detection threshold. In order to identify counterparts, the procedure searches archival X-ray data from instruments such as *Swift*-XRT, *Chandra*, and *XMM-Newton*; sources are also checked for optical counterparts in the NED[3] and SIMBAD[4] databases (see Baumgartner et al. 2013, Oh et al. 2018, and references therein for details). Monthly-binned light curves (in either each of the eight bands or the full BAT band) are generated by creating monthly, all-sky mosaic images, and then extracting the mosaic fluxes for each month for all sources detected in the full survey.

The most recent versions of the BAT's hard X-ray survey, namely the 105-month and 157-month catalogs (Oh et al. 2018; Lien et al. in prep), are unique in that they provide continuous, well-sampled observations over a $\gtrsim$ 9-year timescale for a hard X-ray selected sample of sources, and thus sample the time variability of these objects in a previously unexamined time domain. Due to its wide field of view, this survey yields data for over 1600 sources that have been detected since $\sim$December 2004, $\sim$1000 of which are AGN, and 158 of which are classified as "beamed AGN". The BAT catalog therefore currently boasts the largest sample of AGN observed in the hard X-rays on long timescales, with a wide range in redshift and luminosity exhibited across the AGN listed in the catalog.

In this thesis, the *Swift*-BAT monthly catalog data for the blazars detected in the survey are used extensively, and two of the core chapters (Chapters 3 and 4) use the data as a basis for studying the long-term behavior of these objects that the telescope probes. In addition, for some blazars, the archival BAT data is compared with newer data that was acquired from other

[3]https://ned.ipac.caltech.edu/
[4]https://simbad.u-strasbg.fr/simbad/sim-fbasic

well-known X-ray telescopes, such as *XMM-Newton*, *NuSTAR*, and *NICER*.

1.4 Thesis Outline

This thesis investigates the properties of the X-ray emission of blazars and beamed AGN detected by the *Swift*-BAT, with an eventual focus on the long-timescale variability of these objects.

In Chapter 2, I present a case study with data from *XMM-Newton*, *NuSTAR*, and the *Swift*-BAT of the gamma-ray emitting narrow-line Seyfert 1 1H 0323+342, a blazar-like AGN with X-ray emission whose origins had not been clearly established in previous studies. For the first time, we definitively detect features in this source that suggest that the X-ray emission predominantly comes from the corona in the vicinity of the black hole, while also finding evidence for non-thermal jetted emission in the hard X-rays. This study helps establish this AGN as a member of a group of unique sources that may be used to study emission from the disk, corona, and jet, as well as any connections between the mechanisms that produce the emission from these regions.

In Chapter 3, I investigate the rest of the blazars in the *Swift*-BAT catalog and publish the first dedicated time-domain study of the hard X-ray variability behavior of blazars on long timescales based on $\sim$13 years of continuous hard X-ray data in the 14-195 keV band, where I find that a significant portion of the blazars in the sample do not show statistically significant hard X-ray variability on monthly timescales, deeply at odds with previous studies that show that blazars are highly variable in the X-rays and other energy bands on a wide range of timescales. I also show that the FSRQs and BL Lacs for which we do detect variability exhibit similar flux variability, and that the long-term spectral variability for some of the brightest blazars can be characterized as a simple power law that changes spectral slope over time.

In Chapter 4, I present a study that serves as a follow-up to the supposed lack of variability that is found for a significant fraction of the blazars from the sample analyzed in Chapter 3. I investigate the spectral and temporal behavior of 4 faint, "quiescent" blazars as seen by the BAT by using observations from a recent, 5-month long *NICER* campaign, as well as archival BAT data. I show that variations are detected in the *NICER* band on minute, $\sim$weekly, and monthly timescales, but that the variability is overall low and decreases with longer timescales, implying generally low-amplitude variability across the 4 sources and showing very low variability on monthly timescales, once again showing behavior that is fairly unexpected of blazars. In addition, I find that the broadband X-ray spectra (0.3-195 keV) of the sources can be described with different types of power law models, with one source interestingly requiring significant absorption in the soft X-rays, possibly due to interactions with the warm-hot intergalactic medium.

In Chapter 5, I discuss future directions in which my research could be taken. This includes a recent multi-cycle campaign with new *NICER* data that follows up on the one mentioned in Chapter 4, which slightly increases the sample size of that study and will attempt to characterize the variability of these blazars on even longer timescales with the *NICER* data. In addition, I describe a future project that involves a joint Fourier-based, frequency domain analysis of *NuSTAR* and BAT data for a mixture of blazars and non-blazar AGN. This study would provide the first well-sampled time variability characteristics in the hard X-rays for a small sample of AGN over timescales ranging from minutes to $\sim$15 years. Finally, I briefly touch on expanding some of these studies to other wavelengths, as well as prospects for continuing this research with future X-ray observatories.

1.5 A summary of facilities and software

1. `XSPEC` (Arnaud 1996)–Used for X-ray spectral analyses (chapters 2, 3, and 4)
2. Astropy (Astropy Collaboration et al. 2013)–primarily used for handling FITS files and extracting/reading astronomical data throughout the research; NumPy (Harris et al. 2020)–handling arrays of data/mathematical operations; SciPy (Virtanen et al. 2020)–statistical tests/analyses; Matplotlib (Hunter 2007)–basic plotting
3. Veusz (Sanders 2003; `https://veusz.github.io/`)–for publication-ready plots
4. The data used in Chapter 2 can be found in the *XMM-Newton* Science Archive at `http://nxsa.esac.esa.int/nxsa-web/#home`
5. Data used in Chapter 3 can be found in the online *Swift*-BAT 157-month catalog at `https://swift.gsfc.nasa.gov/results/bs157mon/`
6. Data used in Chapter 4 can be found online in the *Swift*-BAT 105-month catalog (`https://swift.gsfc.nasa.gov/results/bs105mon/`); the *NICER* data from our campaign can now be found in the HEASARC archives at `https://heasarc.gsfc.nasa.gov/cgi-bin/W3Browse/w3browse.pl`

Chapter 2: The origin of X-ray emission in the gamma-ray emitting narrow-line Seyfert 1 1H 0323+342

In this chapter, we present the results of X-ray spectral and timing analyses of the closest gamma-ray emitting narrow-line Seyfert 1 (γ-NLS1) galaxy, 1H 0323+342. We use observations from a recent, simultaneous *XMM-Newton*/*NuSTAR* campaign. As in radio-quiet NLS1s, the spectrum reveals a soft excess at low energies ($\lesssim 2$ keV) and reflection features such as a broad iron K emission line. We also find evidence of a hard excess at energies above ~ 35 keV that is likely a consequence of jet emission. Our analysis shows that relativistic reflection is statistically required, and using a combination of models that includes the reflection model `relxill` for the broadband spectrum, we find an inclination of $i = 63^{+7}_{-5}$ degrees, which is in tension with much lower values inferred by superluminal motion in radio observations. We also find a flat ($q = 2.2 \pm 0.3$) emissivity profile, implying that there is more reflected flux than usual being emitted from the outer regions of the disk, which in turn suggests a deviation from the thin disk model assumption. We discuss possible reasons for this, such as reflection off of a thick accretion disk geometry.

2.1 Introduction

Narrow-line Seyfert 1 (NLS1) galaxies are a type of active galactic nucleus (AGN) characterized by their unique optical spectral features, such as broad Balmer emission lines with low widths ($\mathrm{FWHM}_{\mathrm{H}\beta} < 2000$ km s^{-1}), weak [OIII] emission ([OIII]/H_β flux < 3), and strong FeII emission (Osterbrock & Pogge, 1985). Studies have suggested that NLS1s host supermassive black holes on the lower-mass end ($\sim 10^6 - 10^8 \mathrm{M}_\odot$, (Grupe & Mathur, 2004; Deo et al., 2006)) that accrete near or above the Eddington limit (e.g., Peterson et al., 2000). As a result, it is believed that NLS1s form a set of younger AGN that have yet to transform into more luminous quasars.

In addition to their optical properties, NLS1s are bright in the X-ray band and exhibit complex X-ray spectral features, such as an excess in soft X-ray emission and reflection features in the hard X-rays. As with other accretion systems around black holes (e.g. black hole X-ray binaries), the primary form of the X-ray emission is a continuum well-modeled by a power law that results from the inverse Compton scattering of seed disk photons by a hot plasma of electrons, or a corona, that lies above the disk in the vicinity of the black hole. Some of this continuum emission illuminates the accretion disk, and the upscattered photons end up either Compton scattering off of electrons in the disk, or are reprocessed through fluorescence (see Reynolds & Nowak 2003 for a review). These reflection mechanisms have also been featured in the spectra of NLS1s in the form of an iron emission line between 6-7 keV and a Compton reflection "hump" that peaks between around 20 and 30 keV, implying that the reflection is occurring off of an ionized disk (for reflection features in NLS1s, see e.g. Marinucci et al. 2014; Kara et al. 2017). The Fe emission line in these spectra is usually broadened and skewed towards lower energies due to line-of-sight

Doppler boosting and the gravitational potential of the black hole, respectively (Fabian et al., 1989; Reynolds & Nowak, 2003). Which effect is most dominant depends on the inclination of the disk relative to our line of sight; therefore, from reflection processes alone, we can arrive at an estimate for the disk inclination of a NLS1.

The origin of the soft excess is still disputed. It can be modeled as blackbody thermal emission, but this is not physical because the resulting blackbody temperature is simply too high to be emission from the disk. A way around this is to consider a "warm" Comptonization region that is optically thicker than the corona, which yields a temperature of around 0.1-0.2 keV that is constant across a wide range of black hole masses and accretion rates (e.g., Gierliński & Done, 2004). Other ideas that have been put forth place atomic processes like reflection or absorption as the culprits. One example of the former is that coronal illumination of the disk could result in the fluorescence of lines at lower energies that end up being blurred due to gravitational effects (Crummy et al., 2006; Fabian et al., 2009; Walton et al., 2013). The soft excess could also be described by a disk with a high electron density. With a higher density, bremsstrahlung would have a higher contribution to the spectrum, in the form of an increased temperature at the surface of the illuminated disk that results from free-free absorption (García et al., 2016; Jiang et al., 2018; Mallick et al., 2018; Jiang et al., 2019). This, in turn, may cause blurred reflection at low energies to look more like a blackbody spectrum. If a higher density disk is not taken into account, this could result in a perceived excess at lower energies, especially in AGN with smaller supermassive black holes ($M \ll 10^9 \mathrm{M}_\odot$).

The spectral features of NLS1s have also been described by a series of alternative, absorption-based partial covering models. In this family of models, the X-ray variability is not intrinsic to the source, but is rather caused by a varying partial covering fraction of clouds that possibly result from disk instabilities or radiation-driven outflows. Gallo et al. 2004 and Tanaka et al. 2004 described spectral changes in the NLS1 1H 0707-495 with neutral single and double layer absorbers, respectively, with the latter assuming that the covering fraction changed with the clouds' orbital motion. In addition, Miyakawa et al. 2012 and Mizumoto et al. 2014 were able to explain the broad line feature in MCG-6-30-15 and 1H 0707-495 with ionized partial covering models, with Mizumoto et al. 2014 suggesting that the clouds are produced by funnel-shaped disk winds. However, several studies have shown that most accreting objects have a linear RMS-flux relation, which suggests that the underlying X-ray variability processes are multiplicative in nature and are therefore intrinsic to the source (e.g., Alston, 2019; Uttley et al., 2005). This is at odds with the inherent features of partial covering models, which would show shot noise, additive variability. Due to these characteristics and the mysterious nature of some of these observations, NLS1s, along with other Seyferts, are not only ideal candidates for studying X-ray emission processes and their origins, but also offer interesting possibilities in the realm of X-ray astronomy pertaining to an AGN's central region.

Roughly 10% of AGN exhibit collimated, relativistic jets that emit in the radio band via synchrotron radiation (e.g., Begelman et al., 1984). Another unsolved problem in the physics of AGN processes is exactly where and how these jets are launched, and as a result, the connection between the disk, corona, and the jet's driving mechanism is currently poorly understood. In any case, "radio-loud" (RL) AGN with the X-ray spectral features discussed earlier would provide the most promising environment in which to study the interaction between these three and other components. Most NLS1s, however, are "radio-quiet" (RQ), meaning that their jets are not nearly as powerful as those from blazars or other RL AGN. Therefore, looking for the long-sought disk-corona-jet connection in these AGN proves to be quite difficult.

In recent years, a new class of NLS1s has been discovered by the *Fermi Gamma-Ray Telescope*. These are gamma-ray emitting, RL NLS1s (γ-NLS1), which have features seen in both NLS1s (discussed previously) and blazars, such as flat radio spectra, double-hump spectral energy distribution (SED) (e.g., Abdo et al., 2009), and occasionally superluminal motion (e.g., D'Ammando et al., 2013). The presence of gamma-ray emission in these galaxies is evidence for a jet, given that in those blazars classified as flat spectrum radio quasars (FSRQs), photons from outside a jet can be inverse Compton scattered to hard X-rays or γ-rays by the relativistic particles in the jet; this is referred to as external Compton (EC) (e.g., Błażejowski et al., 2000; Ghisellini et al., 2009b). Studies of the X-ray spectra of these γ-NLS1s have already shown not only a soft excess, but also a "hard excess" above a few keV that requires a much harder power law component compared to the ones usually found in AGN (Bhattacharyya et al., 2014), possibly representing the jet emission. Therefore, these γ-NLS1s provide us with an unusual laboratory for studying properties from both the jet and the thermal emission from the corona simultaneously, and can give us insight into the dominant mechanism that produces the X-ray emission, while at the same time shedding light on how extragalactic jets are formed.

The closest of these exotic AGN is 1H 0323+342 (α: 03 24 41.16, δ: +34 10 45.8), with a redshift of $z = 0.06$ (Zhou et al., 2007). Radio images of this source exhibit superluminal motion (1-7 times the speed of light), which in turn implies the presence of a relativistic jet at an angle $i = 4 - 13$ deg from the line of sight (Fuhrmann et al., 2016). 1H 0323+342 also has a double-hump SED characteristic of γ-NLS1s that peaks in the radio band and gamma-rays, implying synchrotron emission and synchrotron self-Compton and/or EC mechanisms that would result from a jet, and is believed to be in the low-mass end of the FSRQ black hole mass distribution (see Kynoch et al. 2018).

Exactly where the X-ray emission from 1H 0323+342 comes from is still unknown. Currently, two main explanations have been put forth: it could be the result of interactions between the disk and the corona, as in RQ NLS1s (power-law continuum, reflection features, etc.; see Paliya et al. (2014), Paliya et al. (2019a)), or it could simply be a continuation of the double-hump SED that fills the gap between the radio and gamma-ray emission from the jet, implying that X-ray emission would be included as a direct consequence of interactions with the jet (for a detailed multi-wavelength spectral analysis for this source, see Kynoch et al. 2018).

1H 0323+342 has been observed by *Swift* and *Suzaku*, and the spectra show properties seen in RQ NLS1s, such as a soft excess and a potential broad Fe Kα emission line (e.g., Walton et al., 2013; Paliya et al., 2019a). Archival data has shown that there is a potentially blue-shifted iron line that would require a disk inclination of nearly 90° due to line-of-sight Doppler boosting (Walton et al., 2013; Yao et al., 2015), which contradicts data from radio observations since the superluminal motion in the latter indicates that the jet is emitted at an angle close to our line of sight, and therefore also suggests that the disk is face-on. However, the broad iron line has never been clearly detected due to low signal-to-noise.

In this chapter, we present an X-ray spectral and timing analysis with the first such data set from *XMM-Newton* and *NuSTAR* for this source. We aim to find the origin of the X-ray emission in 1H 0323+342, while at the same time obtaining an estimate of the disk inclination purely from the X-ray spectra. We describe the observations and data reduction in Section 4.2, present our spectral and timing analyses and their results in Section 2.3, and discuss these results in Section 2.4.

2.2 Observations and Data Reduction

To study this source, we use a set of six simultaneous observations made by both *XMM-Newton* and *NuSTAR* (twelve total, PI: Kara; see Table 4.1), as well as an archival observation that was made in 2015 (ID 0764670101; PI: D'Ammando).

2.2.1 *XMM-Newton*

The *XMM-Newton* data were reduced with the *XMM-Newton* Science Analysis System (SAS v.16.1.0) and the current calibration files available. We focus on the data from the EPIC-pn camera here, which was taken in Large Window mode. All observations were checked for flaring particle background, and we set PATTERN ≤ 4 to choose single and double events and FLAG $== 0$ to get the best quality data. The data was also checked for pile-up with the SAS epatplot task, but there was no pile-up present in any of the observations. We extracted the source spectra from circular regions with radii of 40″ that were centered on the J2000 coordinates of 1H0323+342. The background spectra were obtained from circular background regions that were offset from the source and were made as large as possible, with radii of 70″.

Background-subtracted light curves were also extracted with the EPICLCCORR tool and were binned with 10 second bins (see Fig. 2.1). Although the flux varies by about a factor of 4, there was no significant change in the spectrum between observations, and the hardness ratio between the hard and soft bands remains relatively constant across each observation. We therefore decided to combine them to form one spectrum. This co-added spectrum was rebinned with the `grppha` tool to ensure that we would have a minimum of 25 counts per bin.

Table 2.1: *XMM-Newton* and *NuSTAR* observations used in our analysis. Shown are the detector name, observation ID, observation start dates, the duration of the observations, and the effective exposure times (for *XMM*, after excluding epochs of flaring particle background). All *XMM* observations were made in Large Window mode.

Detector	Obs. ID	Start Date	Duration (s)	Effective Exposure (s)
EPIC-pn	0764670101	2015/08/23	80900	62000
	0823780201	2018/08/14	53066	47600
	0823780301	2018/08/18	48212	43800
	0823780401	2018/08/20	47975	45461
	0823780501	2018/08/24	48515	46002
	0823780601	2018/09/05	50818	44700
	0823780701	2018/09/09	49468	46951
FPMA/	60061360002	2014/03/15	108880	101633
FPMB	60402003002	2018/08/14	38937	36390
	60402003004	2018/08/18	31711	29732
	60402003006	2018/08/20	28137	26401
	60402003008	2018/08/24	27276	25565
	60402003010	2018/09/05	32516	30422
	60402003012	2018/09/09	29921	27795

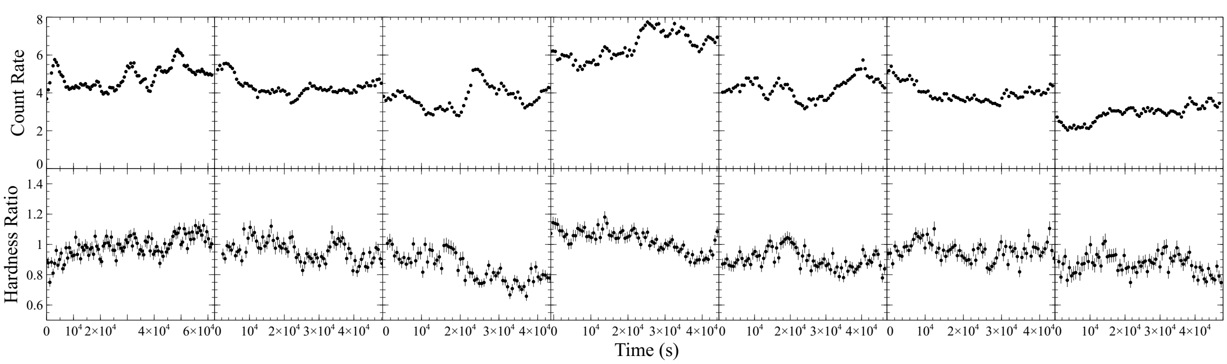

Figure 2.1: *Top panel*: EPIC-pn broadband lightcurves from 0.3-10 keV in 600 s bins. Light curves were generated with circular extraction regions of 40 arcsec radii. The first observation is archival and is longer than the rest by about 30 ks. *Bottom panel*: Hardness ratio (1-4 keV to 0.3-1 keV) of the EPIC-pn observations. For the spectral analysis, the observations were co-added as the hardness ratio remains fairly constant throughout the campaign.

2.2.2 *NuSTAR*

We extracted the *NuSTAR* data using HEASOFT v.6.22.1 and the standard `nupipeline` task, again from 40″ circular regions for both source and background spectra, for each focal plane module (FPMA/FPMB). The spectra were also co-added with the archival observation and binned with `grppha` to have at least 25 counts per bin. The source spectrum is above the background spectrum up to ~ 50 keV, so we show the relevant plots up to this energy.

2.2.3 *Swift*-BAT

To probe higher energies, we make use of the time-averaged data available (BAT name: SWIFT J0324.8+3410) in the Swift-BAT Hard X-ray Survey (Oh et al. 2018). We include the ready-to-use time-averaged eight-channel spectrum that is provided in our analysis.

2.3 Results

2.3.1 RMS-Flux Relation

In the past, it has been shown that most accreting sources have a linear relationship between absolute RMS and flux. Previous works (e.g., Alston, 2019; Uttley et al., 2005; Uttley & McHardy, 2001) have shown that this relation implies a variability process that is intrinsic to the source and that is likely a multiplicative process, building up from propagating mass accretion rate fluctuations occurring in the disk. Since the best model to describe this is one where accretion disk fluctuations are the source of the variability, finding such a relation in 1H 0323+342 would suggest that disk-corona and reflection models, where the X-rays are assumed to be intrin-

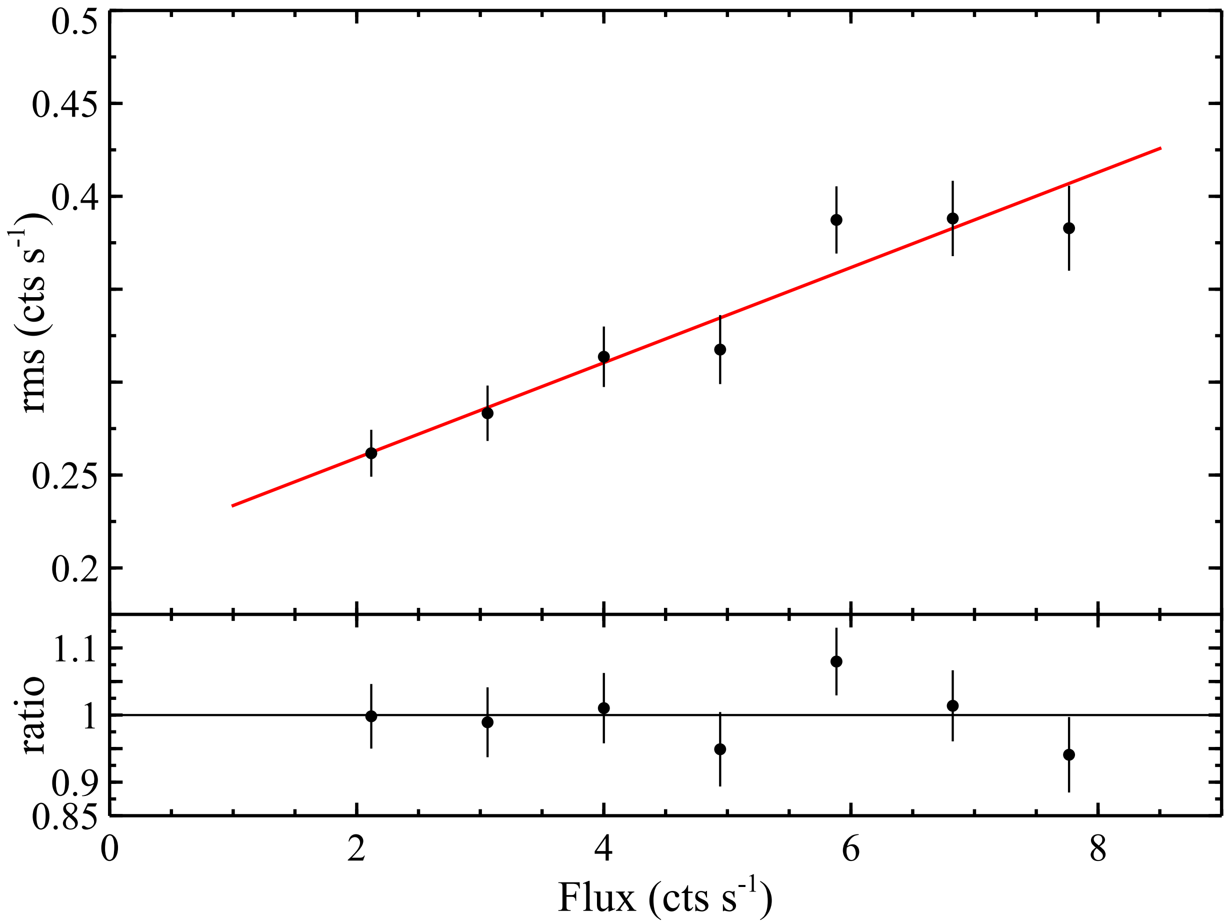

Figure 2.2: Relationship between absolute rms and flux. On average, the absolute rms increases linearly with flux, suggesting that variations are intrinsic to the source.

sic variations originating from the innermost regions of the disk, would be best to describe the data.

We begin a calculation of the rms-flux relationship in the time domain by binning our *XMM* lightcurves in 1000 s bins. At the same time, we compute the excess variance as a function of time with the same binning, effectively producing a 'variance light curve'. We take the square root of the excess variance to obtain the rms amplitude, and sort these values by count rate. We then bin the rms amplitudes by flux such that we have ~ 50 points in each bin. Errors on the rms amplitude are calculated as in Vaughan et al. (2003). We show in Fig. 2.2 that we indeed obtain a linear rms-flux relation, with a linear fit of $\chi^2 = 4.61$ for 5 degrees of freedom. This therefore supports the use of reflection models for this data and implies that the X-ray variations are intrinsic.

2.3.2 Spectral Features

We fit the *XMM-Newton* and *NuSTAR* spectra simultaneously using XSPEC v12.9.1p (Arnaud, 1996). We included an overall multiplicative constant in each of our models ($C_{\rm A}$ for FPMA and $C_{\rm B}$ for FPMB) to take into account differences in absolute flux calibration between each detector. We used the `tbabs` model (Wilms et al., 2000) and cross-sections from Verner et al. (1996) to model the galactic absorption, setting $N_{\rm H,Gal} = 1.26 \times 10^{21} {\rm cm}^{-2}$ (Kalberla et al., 2005). In all of our fits, we also check for potentially different spectral shapes between *XMM* and *NuSTAR*, but we find that the spectral index Γ only differs by $\sim 1\%$ and does not affect our results, so we fit with the same photon index. All spectra are plotted in the source rest frame energies.

2.3.2.1 Reflection Features above 2 keV

We begin by searching for the broad iron line, which has only been marginally detected in previous observations (e.g., Paliya et al., 2019a, 2014; Yao et al., 2015; Walton et al., 2013). To show the highest resolution version of the line and to show we are making a significant detection, we fit the 3-10 keV spectra with a power law (see Figure 2.3) and compare this to a power law plus Gaussian. The addition of the Gaussian improves the fit by $\Delta\chi^2 = 130$ for 3 additional parameters, and therefore a line is preferred at >99.99% confidence. We find a line at 6.6 ± 0.1 keV in the rest frame of the source that is broad with respect to the spectral resolution of the instruments, with $\sigma = 0.62^{+0.13}_{-0.12}$ keV. This is consistent with Fe Kα emission. We also calculate an equivalent width of around 175 ± 40 eV for *XMM*, which is stronger than in archival, lower signal-to-noise observations (e.g., Kynoch et al., 2018) and again supports our claim of a broad line.

Figure 2.3 also shows a relatively pronounced peak between 6 and 7 keV, at the 6.4 keV of neutral iron fluorescence. We therefore include a narrower line fixed at 6.4 keV, in addition to the aforementioned Gaussian, and fix its width to 100 eV. This improves the fit by $\Delta\chi^2 = 10$ for one additional parameter, at a significance of $> 99.8\%$. This suggests that, in addition to the broad iron line, there may also be a narrow component from a distant reflector that contributes to the spectrum.

A power law fit to the 2-79 keV spectra of *XMM-Newton* and *NuSTAR* shows not only a broad iron line peaking at 6-7 keV, but also a Compton reflection hump above 10 keV, indicating reflection off of an ionized disk (see Figure 2.4). This power law yields a reduced chi-squared $\chi^2/\text{d.o.f} = \chi^2_\nu = 2552/2385 = 1.07$. Given the nature of the spectra, it is clear that reflection and possibly relativistic broadening need to be taken into account, so we fit the 2-79 keV data with different flavors of the reflection model `relxill` (Dauser et al., 2016). Following up on the narrow component at 6.4 keV discussed earlier, we start with a neutral, non-relativistic reflection model `xillver`, with the ionization parameter $\log \xi$ fixed at 0. This gives a fit with $\chi^2_\nu = 1.01$, improving from the power law fit by $\Delta\chi^2 = 137$ for 4 additional free parameters, with a significance of $>$ 99.99% evaluated using the F-test. The residuals between 6-7 keV, along with the fact that we detect a fairly broad line, suggest we still need to account for relativistic smearing.

We use the relativistic model `relxill` and set the inner accretion disk radius R_{in} to the innermost stable circular orbit. We start by fixing the emissivity index to the Newtonian value

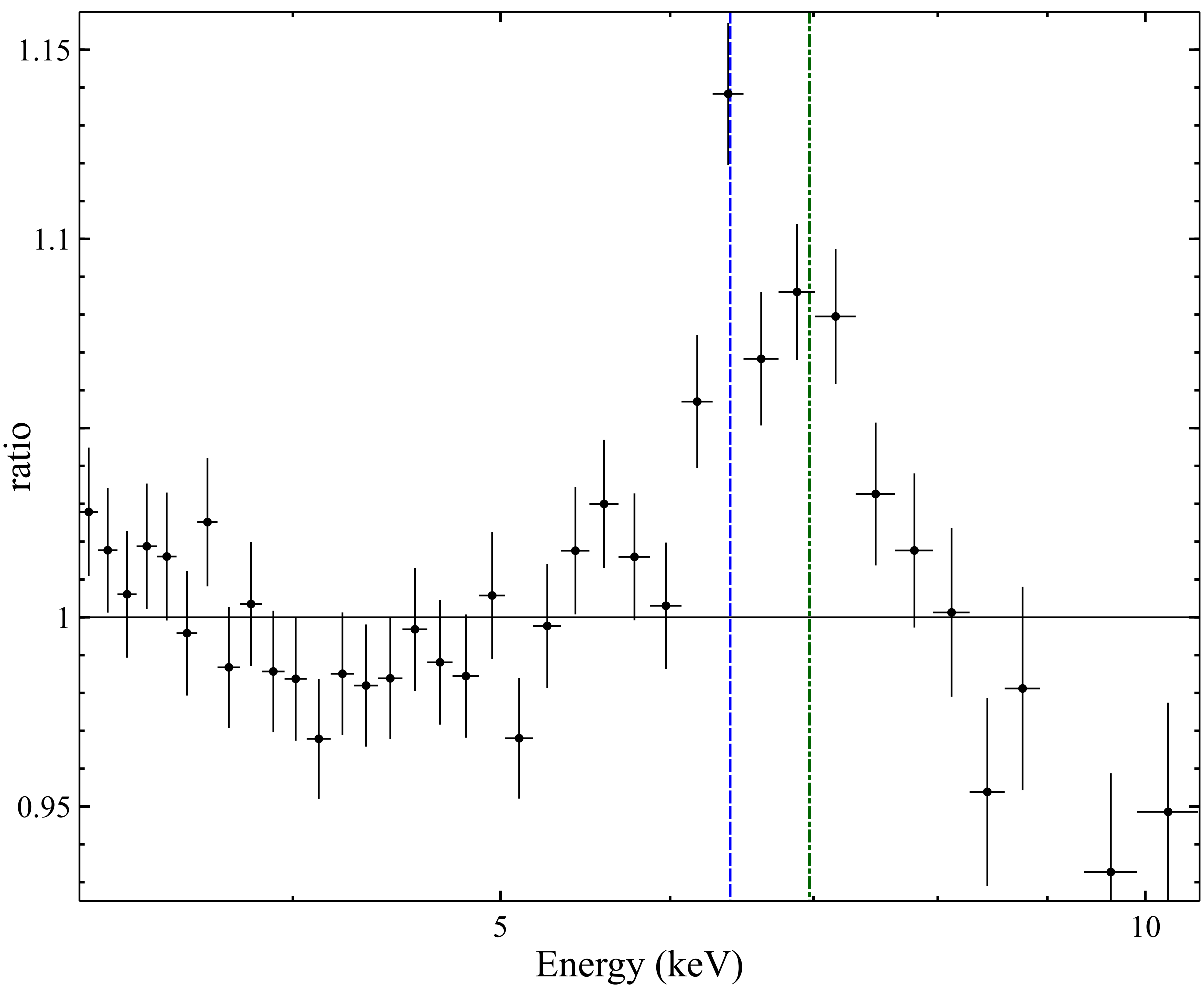

Figure 2.3: The ratio of EPIC-pn to a simple power law; energies are in the rest frame of the source. The blue line shows the position of neutral iron at 6.4 keV, the green line that of hydrogen-like Fe XXVI at 6.97 keV. We find an equivalent width of 175 ± 40 eV for the broad iron line.

$q = 3$ and find a good fit, with $\chi^2_\nu = 2385/2380 = 1.002$. We also attempt using a broken power law emissivity, but this yields a break radius $R_{\rm break}$ that is below the innermost stable circular orbit, which is not physical. We therefore keep an unbroken emissivity for the rest of the chapter. We also cannot constrain the spin a. Since this is a jetted source, it may involve a high-spin object, so we use this physical motivation to fix the spin to the maximum value of 0.998.

We combine the models in the second and third panels of Figure 2.4 to check for the possibility of an additional neutral, distant reflector. All relevant parameters in `xillver` are tied to the parameters of `relxill`, except for the normalization. This improves the fit by $\Delta\chi^2 = 31$ for one additional free parameter, at a significance of $> 99.99\%$. This fit finds an inclination $i = 59^{+4}_{-5}$ deg, which is in tension with the low inclination obtained from radio observations. Within 90% confidence, this fit yields very similar parameters as the ones with just `relxill`, and we adopt this version for later analyses of the broadband spectrum. We report the best-fit parameters in Table 2.2.

Our fits also seem to show consistent negative residuals at ~ 9 keV (see Figures 2.3 and 2.4). It is important to note that this is most likely not physical. When we plot the background spectrum, we see that this is probably a background feature, namely the EPIC-pn Cu-Kα complex at around those energies. Regardless of our source region size or background region placement (keeping the latter within the inner 4 CCDs), the feature remains. The residuals are therefore likely the result of over-subtraction of the EPIC-pn background features. We verify this by plotting the spectrum without the background subtracted, and find that the feature is not present (see Appendix A.1). We also do not see the negative residuals in any of the individual EPIC-MOS spectra.

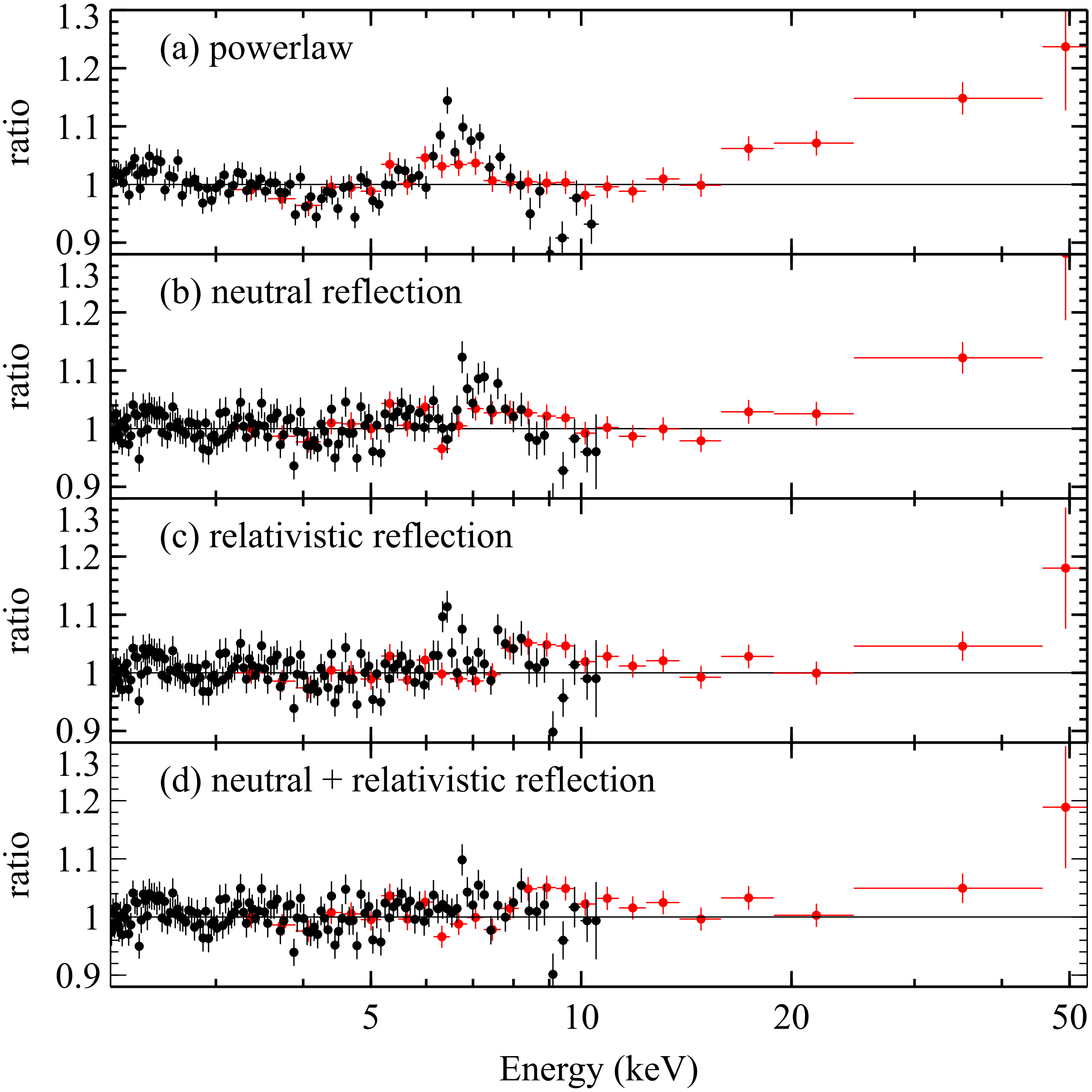

Figure 2.4: The ratio of EPIC-pn and *NuSTAR* spectra to different models. (a) The ratio to a power law. (b) Ratio to neutral reflection model. (c) Ratio to relativistic reflection model. (d) Ratio to relativistic reflection model with an additional neutral, distant reflector.

Parameter	`xillver + relxill`	`diskbb + xillver + relxill + po`
$N_{\rm H,Gal}$ (10^{22}cm^{-2})*	0.126	0.126
$N_{\rm H,intrinsic}$ (10^{22}cm^{-2})	...	< 0.01
$K_{\tt diskbb}$	...	200^{+65}_{-66}
$K_{\rm dist.\ reflection}$ (10^{-5})	$1.1^{+0.5}_{-0.4}$	0.5 ± 0.4
$K_{\rm rel.\ reflection}$ (10^{-5})	$3.3^{+0.5}_{-0.4}$	$1.8^{+0.6}_{-0.5}$
z*	0.06	0.06
$T_{\rm in}$ (keV)	...	0.18 ± 0.01
Γ	1.91 ± 0.01	$2.2^{+0.3}_{-0.1}$
$\Gamma_{\rm hard}$	...	$1.5^{+0.1}_{-0.2}$
$E_{\rm cut}/kT$ (keV)	> 453	300
$A_{\rm Fe}$	3 ± 1	4^{+5}_{-2}
log ξ (erg cm s^{-1})	< 2.9	< 1
$\mathcal{R}_{\rm refl}$	0.6 ± 0.1	$1.3^{+0.4}_{-0.7}$
i (deg)	59^{+4}_{-5}	63^{+7}_{-5}
$R_{\rm in}$ (ISCO)*	1	1
$R_{\rm out}$ $(R_{\rm g})$*	400	400
$R_{\rm break}$ $(R_{\rm g})$*	15	15
q	3	2.2 ± 0.3
a*	0.998	0.998
$C_{\rm A}$	1.17 ± 0.01	1.17 ± 0.01
$C_{\rm B}$	1.20 ± 0.01	1.20 ± 0.01
χ^2/d.o.f.	2354/2379	2693/2679
χ^2_ν	0.99	1.01

Table 2.2: 90% confidence level parameters for the 2-79 keV and 0.5-79 keV ranges, reported with respect to EPIC-pn. K's are normalizations, $C_{\rm A}$ and $C_{\rm B}$ are the calibration constants for FPMA and FPMB, respectively, and q is the emissivity index. $\Gamma_{\rm hard}$ is the photon index of the hard power law, $T_{\rm in}$ the temperature at the inner disk radius, and $E_{\rm cut}$ the cutoff energy in the rest frame of the source. $\mathcal{R}_{\rm refl}$ and ξ are the reflection fraction and ionization parameter of the relativistic reflection component, respectively. $N_{\rm H,Gal}$, $R_{\rm in}$, z, $R_{\rm break}$, a and $R_{\rm out}$ were frozen to the corresponding values (parameters with asterisk). In addition, the ionization parameter in the `xillver` distant reflector model was frozen to 0.

2.3.2.2 Broadband Spectrum

Fitting a power law to the data in the 2-79 keV range and extrapolating the fit to lower energies also reveals a soft excess below 2 keV. We begin our analysis in the broadband by including a phenomenological disk blackbody component to help fit the spectrum at soft energies. To account for the possibility of intrinsic absorption, we use `ztbabs`. We also keep the neutral, distant reflector from the previous section.

We first attempt a Newtonian emissivity profile for the `tbabs*ztbabs*(diskbb + xillver + relxill)` model. This gives a fit with $\chi^2_\nu = 1.04$. Freeing the emissivity index improves the fit by $\Delta\chi^2 = 37$ for one additional free parameter at a significance $> 99.99\%$, with $\chi^2/\mathrm{d.o.f.} = 2760/2680 = 1.03$. Increasing residuals at energies $\gtrsim 35$ keV remain in the *NuSTAR* data (see Figures 2.4 and 2.5), and including the archival BAT data in the spectrum further suggests the presence of a hard excess component (Figure 2.5), so we include an extra power law to account for a possible contribution of Compton upscattering further out in the jet, similar to Paliya et al. 2019a. An additional hard power law improves the fit by $\Delta\chi^2 = 46$ for two additional free parameters with a significance $> 99.99\%$. We find that the fit does not significantly depend on the cutoff energy, so we fix it to 300 keV. This best fit (see Figure 2.6 and second column of Table 2.2) yields a photon index of $\Gamma = 2.2^{+0.3}_{-0.1}$ for the coronal emission models and $\Gamma_{\rm hard} = 1.5^{+0.1}_{-0.2}$ for the hard power law, which is consistent with values found in γ-NLS1s (see e.g. Paliya et al. 2019a and the Γ histograms for their double power-law fit, as well as photon index values in Ojha et al. 2020). It also gives a high inclination of $i = 63^{+7}_{-5}$ deg, as before. Moreover, we obtain a relatively flat emissivity index $q = 2.2 \pm 0.3$, suggesting not only that strong general relativistic effects are not required to accurately describe the illumination

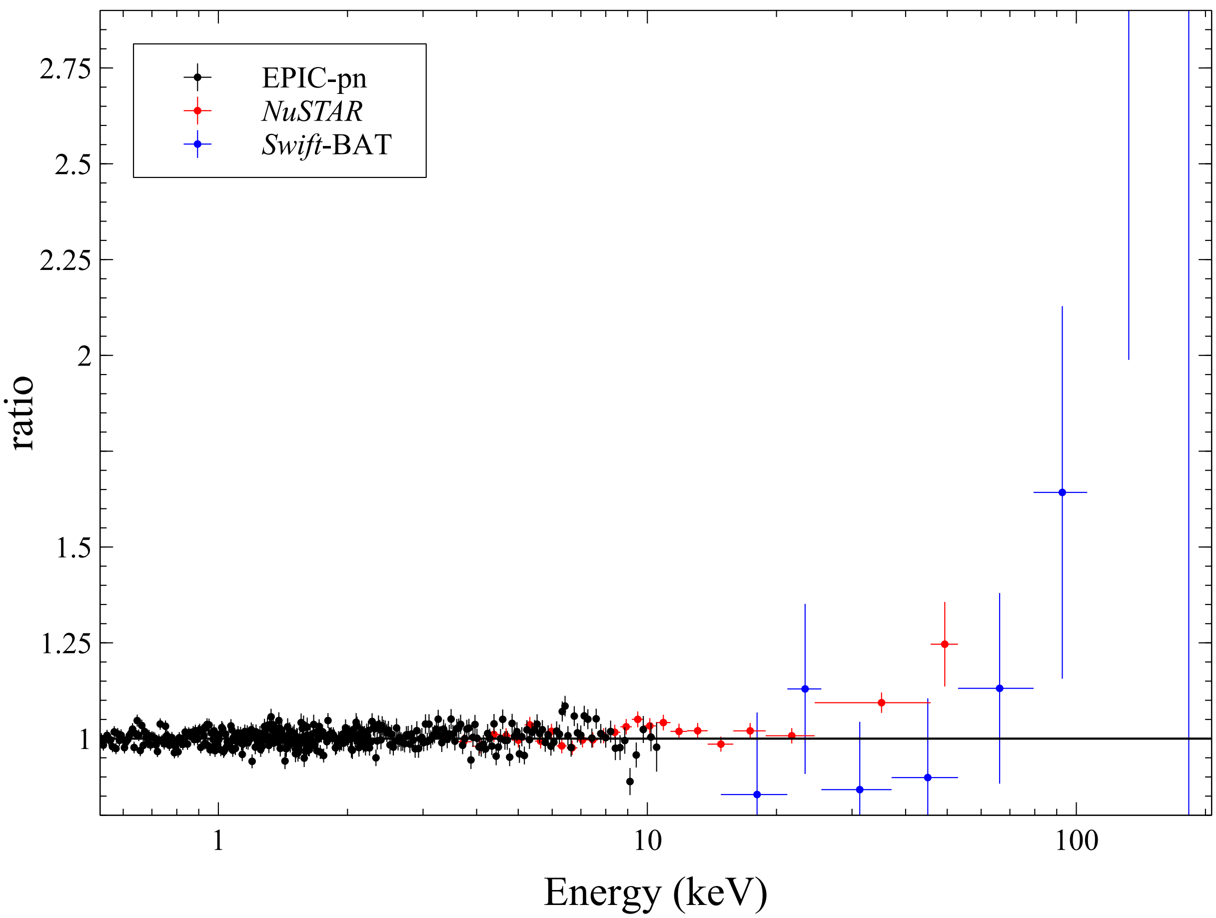

Figure 2.5: Residuals with the *Swift*-BAT time-averaged data included. The additional archival data further suggest a hard excess component.

pattern of the disk, but also that more reflected flux is emitted from the outer regions of the disk. The fact that the observed flux seems to drop slowly at large radii could be an indication that the razor-thin disk assumption is invalid.

We also attempt to model the data with a more physically motivated approach. Following the possibility that the soft excess could arise from reflection off of a high-density disk (e.g., García et al., 2016; Jiang et al., 2018; Tomsick et al., 2018), we try to fit the soft excess with the extended reflection model `relxillD`. Given that this source is at a low galactic latitude, it is likely that there is a fair amount of uncertainty in the column density, so we allow `tbabs` to be a free parameter, and remove `ztbabs`. We also include an additional hard power law to compare

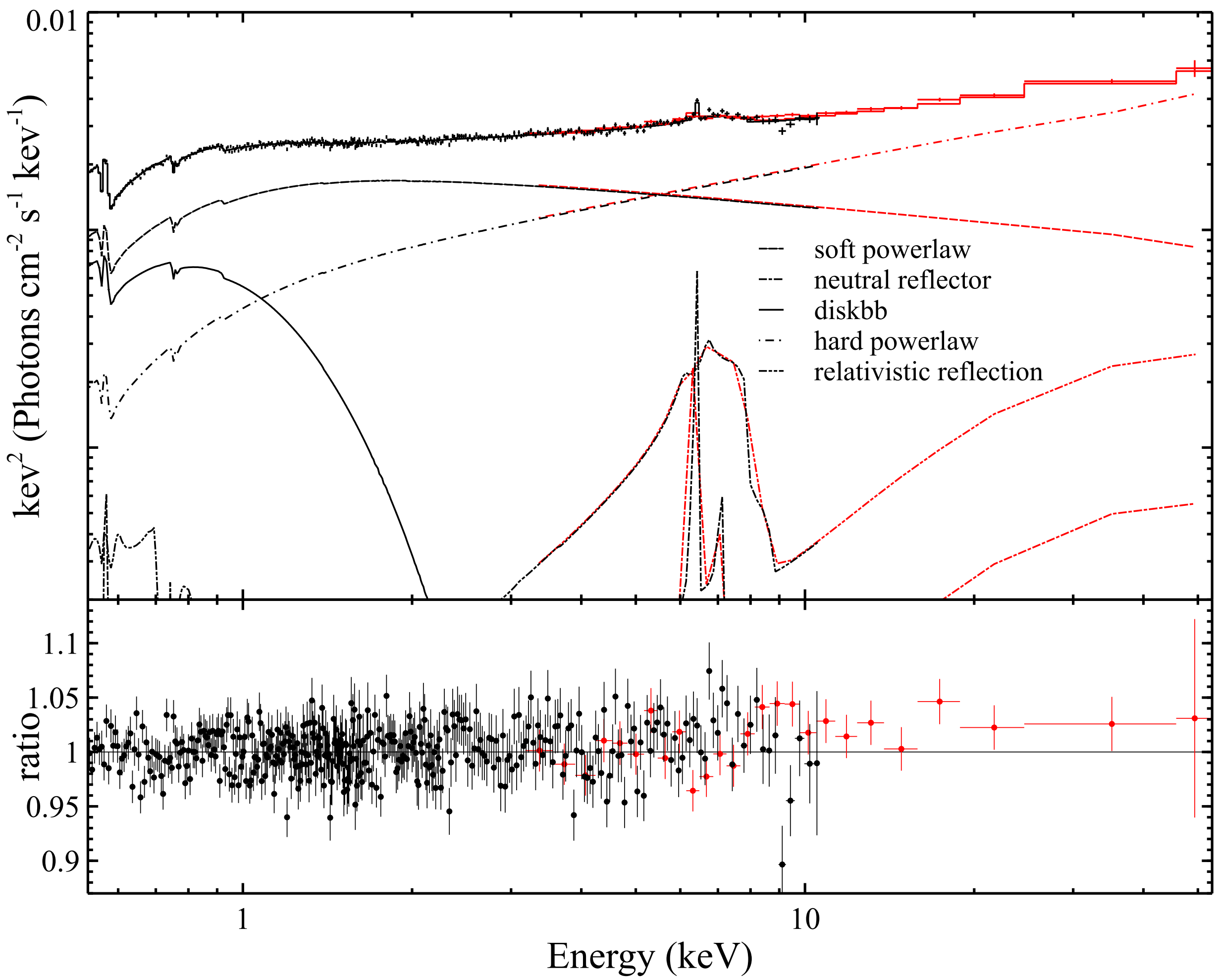

Figure 2.6: Unfolded spectrum and best-fit model. Model components are also shown. EPIC-pn data from *XMM-Newton* are shown in black; *NuSTAR* data are shown in red.

directly with our `diskbb` fit. This `tbabs*(xillver + relxillD + po)` model yields an acceptable fit with χ^2/d.o.f. $= 2726/2680$ and an electron density log $n_e = 17.2^{+0.5}_{-0.1}$, but it requires an iron abundance of > 9 and a high emissivity index $q = 7^{+1}_{-2}$, which suggests a much higher degree of relativistic smearing than is expected given the equivalent width of our iron line. As in our previous model, it also requires a very high inclination, with $i = 72^{+3}_{-5}$.

For completeness, we also fit the broadband spectrum with an alternative, ionized partial covering model instead of relativistic reflection, replacing `relxill` with `zxipcf*powerlaw` in our best fit, in order to see if we actually require a broad iron line. We also apply `zxipcf` to the disk blackbody component and remove the hard power law component for simplicity. This model, which instead fits the broad line region with a combination of an absorbed power law and a narrow reflection component, gives an acceptable fit with χ^2/d.o.f $= 2726/2681 = 1.02$. It requires a covering fraction of $0.56^{+0.07}_{-0.08}$, as well as an outflow velocity of nearly $\sim 0.1c$, which is probably needed in order to account for the blueshift of the iron K line. However, the physical processes represented by this model would manifest themselves in the variability as shot noise, or additive, variability processes, but we instead see a linear RMS-flux relationship representing multiplicative variability processes.

2.3.2.3 Disk Inclination

In our best-fit model, we find an unphysically high disk inclination. We confirm this result by generating the statistic surface for this parameter, which gives comparable values (see Figure 2.7). This is much higher than predicted by superluminal motion in radio observations (Fuhrmann et al., 2016), which implies a relativistic jet at an inclination $i = 4 - 13$ deg from the line of sight.

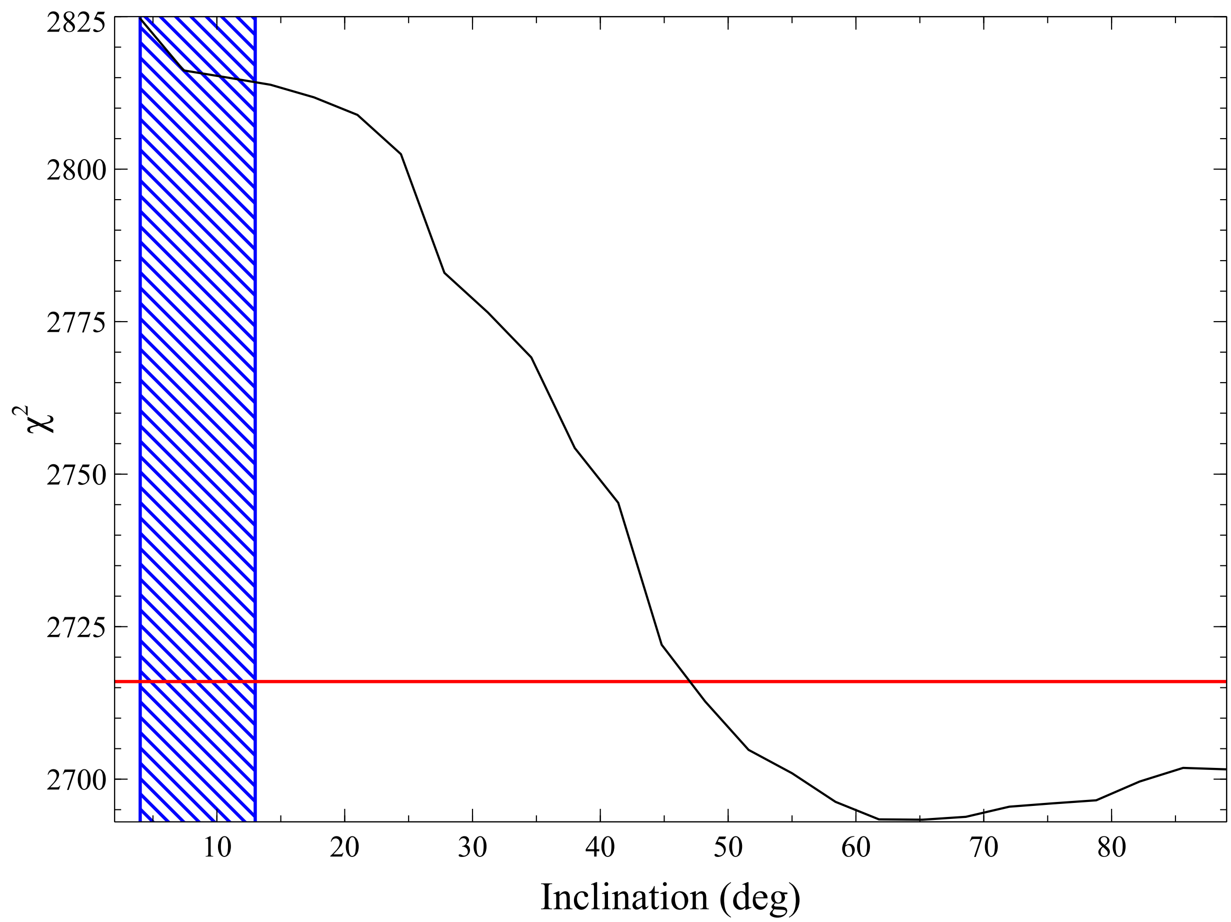

Figure 2.7: χ^2 statistic vs. disk inclination for our best fit. The red horizontal line is the 90% confidence level. The blue hashed region depicts the range set by radio observations (4-13 deg).

We therefore attempt to further constrain the inclination angle by placing hard limits at these values. However, we are unable to constrain the inclination this way, as the parameter is pegged at the hard upper limit, so we proceed to fix the inclination to a value of 10 deg. This scenario provides a fit with $\chi^2_\nu = 1.04$, and we again find that our best fit with an unrestricted inclination is an improvement at a significance of $> 99.99\%$ ($\Delta\chi^2 = 70$ for 1 additional free parameter). Therefore, our data suggests that, although we do observe a broad iron line, the broadening may be caused almost exclusively by line-of-sight Doppler effects that result from a high inclination. However, this is at odds with superluminal motion inferred from radio observations. Alternatively, the geometry is not a simple geometrically thin disk, as assumed by the blurred reflection model.

2.3.3 Timing Analysis

In addition to the spectral analysis described in the previous section, we also performed a timing analysis to compare to timing analyses from RQ NLS1s. X-ray reverberation lags have been used to probe the inner accretion disk region as a means to gain insight into the origin of the X-ray emission in NLS1s (e.g., Fabian et al., 2009; Uttley et al., 2014). These so called "soft lags" are caused by a reflection-induced soft excess that lags behind coronal power-law photons due to the short, extra time the latter take to travel from the corona to the inner disk. The detection of a soft lag therefore provides evidence that the soft excess is due to relativistic reflection; on the other hand, a non-detection of a soft lag could suggest that the soft excess is possibly a different component that is not simply reflection.

In the next subsections, we look into whether we can detect soft lags in 1H 0323+342, and analyze the relationship between variations in the soft band and those in the hard band by using Fourier techniques outlined in works such as Nowak et al. (1999) and Uttley et al. (2014).

2.3.3.1 Lag-frequency spectrum

We begin the second part of our timing analysis by using the available 7 light curves to compute time lags between the power law dominated hard band (1-4 keV) and the soft excess (0.3-1 keV) as a function of temporal frequency, or inverse timescale. If the light curve in, say, the soft band, s, has N time bins of width Δt, then its discrete Fourier transform at each Fourier frequency $f_n = n/(N\Delta t)$ is

$$S = \sum_{k=0}^{N-1} s_k e^{2\pi i n k/N} \tag{2.1}$$

We focus on frequencies higher than 6×10^{-5}Hz to avoid red noise leakage at lower frequencies. We require at least 10 frequencies per bin.

We can rewrite the Fourier transform in a complex polar form as $S = |S|e^{i\phi_s}$. Repeating the process for the hard band light curve h, we can write the complex conjugate of its Fourier transform as $H^* = |H|e^{-i\phi_h}$. The product of S and H^* gives us the Fourier cross-spectrum between the two bands:

$$C = |H||S|e^{i(\phi_s - \phi_h)} \tag{2.2}$$

This gives the phase difference between the soft and hard bands, and the average lag between the two bands in each frequency bin is then obtained by taking the phase of the averaged cross-spectrum, or $\phi = \arg[\langle C \rangle]$. This can then be manipulated to give the time lag at each frequency bin:

$$\tau = \frac{\phi}{2\pi f} \tag{2.3}$$

Figure 2.8 shows the resulting lag-frequency spectrum between lightcurves in the 0.3-1 keV and 1-4 keV bands that had 10 s bins. To decide our upper limit in frequency, we calculate the frequency range where we expect to see reverberation, given the black hole mass of this AGN, by using the correlation between soft lag frequencies and black hole mass from De Marco et al. (2013). Landt et al. (2017) obtain a mean mass of $1.9^{+0.4}_{-0.3} \times 10^7 \mathrm{M}_\odot$ through estimates based on the ionizing 5100 Å continuum luminosity and the width of the hydrogen broad emission lines. We use this mass in the correlation in De Marco et al. (2013), and find that this corresponds to a frequency range $\nu_{\mathrm{lag}} = (2.3 \pm 0.5) \times 10^{-4}$ Hz where we can expect to find a soft lag. As a precaution, we extend the frequency range to $1 \times 10^{-3}\mathrm{Hz}$, to account for uncertainties in the mass estimate and the frequency-mass correlation.

While our spectrum shows a low-frequency hard lag that is consistent with propagating fluctuations in the disk, our spectrum shows no soft lags at shorter timescales, which could be related to a lack of coherence between the soft and hard bands, something we investigate in the next subsection. This non-detection may also in fact support our spectral results by suggesting that reflection off of the accretion disk is not the dominant process causing the soft excess.

2.3.3.2 Coherence-frequency spectrum

In an attempt to further explain the non-detection of soft lags, we proceed to calculate the coherence between the soft and hard light curves. The coherence provides us with a way of measuring how correlated two light curves or signals are. Essentially, it tells us to what extent

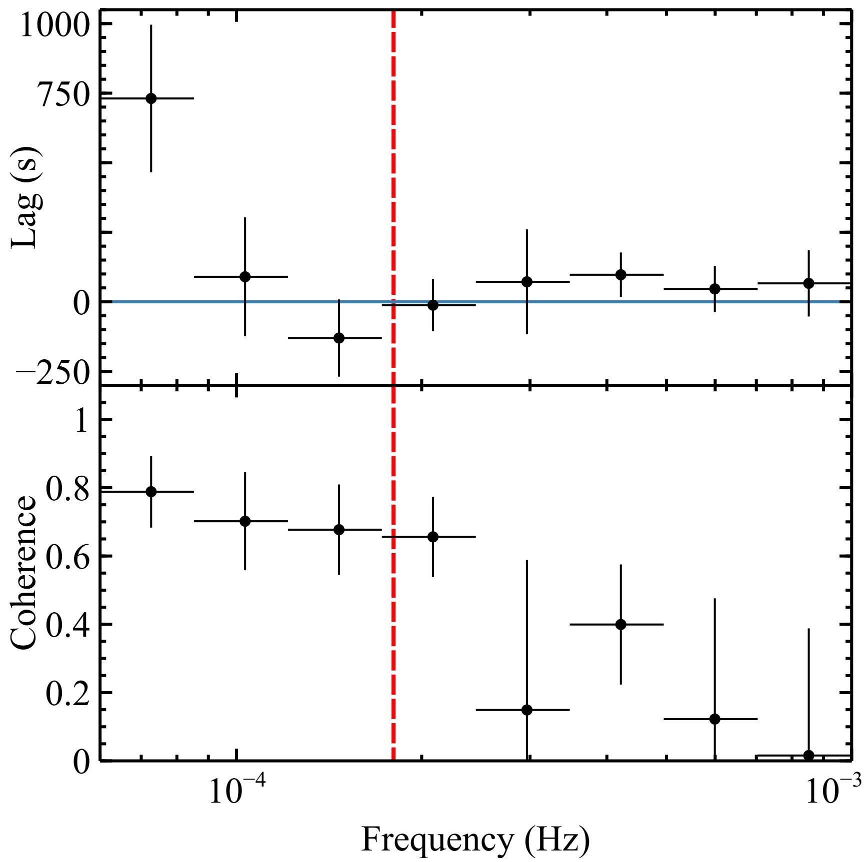

Figure 2.8: Time lag and coherence between variations in the soft (0.1-3 keV) and hard (1-4 keV) bands as a function of timescale (temporal frequency). The dashed red line is the frequency above which we would have expected reverberation. Our results yield a soft lag of zero, possibly suggesting the soft excess is not necessarily due to reflection, and a relatively low coherence, suggesting that the soft excess may not be directly correlated with the hard band.

one light curve can be predicted from the other. The coherence at each frequency is defined as

$$\gamma^2 = \frac{|\langle C \rangle|^2 - n^2}{\langle P_s \rangle \langle P_h \rangle} \tag{2.4}$$

where the n^2 term is due to Poisson noise contributing to the square of the cross-spectrum, and the terms in the denominator are noise-subtracted power spectra. For unity coherence, the two light curves would be perfectly coherent, meaning one would be able to predict a light curve from the other through a linear transformation.

Figure 2.8 shows the coherence-frequency spectrum that results from our data. On long timescales, the coherence is $\gtrsim 0.6$, representing the fact that on these timescales, the dominant form of emission in both the soft and hard light curves is expected to be from the power-law continuum, so they should be fairly well correlated. In the frequency range where we expect to see reverberation, given this black hole mass, we can see that for the most part the coherence is below 0.6 and consistent with 0. The non-unity coherence at these frequencies shows that there is a non-linearly correlated component in the soft band. A coherence less than unity may have to do with an additional soft excess continuum component that is variable in a way that is not correlated with the power-law and reflection components.

2.4 Discussion

2.4.1 Where does the X-ray emission of 1H 0323+342 come from?

Previous studies of 1H 0323+342 have had mixed approaches when it comes to the modeling of the source's X-ray spectra. By using a simple comparison in count rates between the soft

(0.3-2 keV) and hard (2-10 keV) bands of *Swift*-XRT observations, Paliya et al. (2014) showed that 1H 0323+342 might exhibit a strong soft excess whose variability was not perfectly correlated with the variability of the hard band, which may suggest that at least two spectral components are required to fit the X-ray spectra of this source. They successfully fit the spectrum using an ionized reflection model, and found that the fit improved when they took relativistic blurring into account. However, they fix the inclination to 10 deg. This resulted in a steep spectrum ($\Gamma = 2.02 \pm 0.06$) and a high spin ($a = 0.96 \pm 0.14$). Ghosh et al. (2018) also assumed that the soft excess was due to reflection and arrived at similar results. However, other studies such as Paliya et al. (2019a) and Kynoch et al. (2018) have managed to obtain good fits by modeling the soft excess with a power law, which adds a layer of ambiguity regarding the best description of the excess at low energies.

In each of these cases (as well as in Walton et al. 2013, Yao et al. 2015), there was some evidence of a potential broad Fe Kα line, but there were a few aspects that were unclear, such as a stark difference in the measured black hole spin between Walton et al. (2013) and Yao et al. (2015) (although the latter froze their inclination to a much lower value), and the fact that the emission was relatively weak to begin with. In addition, Paliya et al. (2019a) and Kynoch et al. (2018) found that a combination of narrow emission lines was adequate enough to fit the residuals at ~ 6 keV. Therefore, as for the soft excess, the nature of these residuals was up for debate.

We find through our spectral analysis that reflection may play a role in both the excess emission in the soft band and the residuals at higher energies ($\sim$2-35 keV); that being said, regardless of the model we use, we require some additional soft excess component that is not reflection. A combination of a reflection model (`relxill`) and a phenomenological blackbody model, along with a distant reflector, results in a good fit to most of the broadband spectrum, and we detect an iron line at 6.6 ± 0.1 keV thanks to the increased signal-to-noise ratio that results from combining 6 simultaneous *XMM-Newton* and *NuSTAR* observations with archival data. However, a discussion of the origin of the blackbody-like component is warranted, and whether it is related to the jet or is due to Comptonization is still unclear.

A high density reflection model can also describe the data fairly well, but certain well-known issues arise, such as the fact that the featureless soft excess requires stronger broadening than the fit to the iron line alone. An alternative ionized partial covering model also works; however, the variability imprinted by a partial covering model would not predict the linear RMS-flux relation we obtain, which suggests that the variability of this source is multiplicative in nature. This further suggests that the X-ray emission originates in the central region of the AGN.

While we detect a hard low-frequency lag that suggests propagating disk fluctuations, we do not detect a soft lag. RQ AGN with similar variance, exposure, and flux do show soft lags, which might suggest that this is not a signal-to-noise issue. This might have to do with the presence of an additional soft excess component that is not simply blurred reflection and that displays variability that is uncorrelated with the continuum-dominated hard band.

The final piece of the spectral puzzle involves the possible hard excess observed at energies above ~ 35 keV. We find that, in each of our models, the residuals seem to increase at higher energies. None of our reflection models were able to take care of this, which implies that this excess may be due to non-thermal processes related to the jet. The otherwise coronal-dominated X-ray spectrum suggests the emission might be contaminated by a combination of synchrotron self-Compton mechanisms and Comptonization of external disk photons, although the fact that the source is probably an FSRQ (see e.g. Kynoch et al. 2018) means that the latter mechanism is likely dominant. This hard excess was also observed in Ghosh et al. (2018). Paliya et al. (2014)

and Paliya et al. (2019a) also detect a hard excess and manage to fit it with a broken power law and a second power law, respectively, and they attribute this to a combination of thermal coronal emission and jet emission with a power-law shape, the latter of which would result from the AGN undergoing γ-ray flaring. In other words, the same process that produces the γ-ray emission (likely external Compton) may be the dominant form of hard X-ray emission above 35 keV. The fact that an additional hard power law component helps fit the hard excess we observe at a significance of $> 99.99\%$ seems to suggest a similar behavior.

2.4.2 Model Inconsistencies and Alternative Assumptions

Fuhrmann et al. (2016) constrain the viewing angle of 1H 0323+342 to values between 4 and 13 degrees using observations in the radio band. In X-ray spectra, the inclination can be independently determined by the shape of the Fe Kα line in the reflection spectrum: if the line is mostly broad and blue-shifted, line of sight Doppler boosting (i.e. larger line-of-sight velocities) has the dominant influence on the line profile, and therefore this would correspond to a highly inclined disk; on the other hand, if the profile is mostly skewed towards lower energies, it would mean that gravitational and time dilation redshifts are dominant, corresponding to a disk that is almost face-on.

Our results in both the 2-79 keV and the broadband ranges with `relxill` provide an inclination that is higher than the upper limit obtained from radio observations (see Table 2.2). Our detection of the iron line also shows that the line is blue-shifted. Walton et al. (2013) had modeled *Suzaku* observations with relativistic reflection and found that if they let the inclination vary, they end up with a highly blue-shifted line that peaks at ~ 8 keV, and obtain an unphysical value of $i = 82 \pm 3$ deg. Therefore, high inclinations have been suggested in the past; however, as previously mentioned, the iron line had only been marginally detected. In this work, we finally have a constraint on the iron line profile, and we still measure a high inclination. Given the latter, it seems that the broadening of the line can be explained almost exclusively through line-of-sight Doppler effects, but this is a lot more Doppler boosting than is physically allowed by the inclination measured in the radio observations. This, along with the unusually flat emissivity profile from our best fit, seems to suggest that we may have to reconsider our model assumptions.

One way to account for a perceived high inclination is to consider the possibility that the emission is being viewed through the acceleration zone of the jet. In this scenario, a highly energetic corona would end up inverse Compton scattering the reflection spectrum. Studies have shown that considering these processes provides a more complete picture of the emission from both black hole transients and AGN, with the logic being that if thermal seed photons from the disk are upscattered by the corona, reprocessed reflection photons that emerge in the inner regions of the disk should also be influenced by the same process (e.g., Wilkins & Gallo, 2015; Steiner et al., 2017). This process could cause the iron line in 1H 0323+342 to be blueshifted, even if the disk is face-on and the jet is closely aligned to the line of sight.

Another way to explain our measurements may involve abandoning the thin disk geometry (Shakura & Sunyaev, 1973) altogether and considering a model where the accretion disk is geometrically thick, a scenario which has also been suggested to explain similar inclination mismatches in X-ray binaries (e.g., Connors et al., 2019). In the past few years, simulations have been used to understand the underlying physical processes behind sources that have very high accretion rates (e.g., McKinney et al., 2015; Sądowski & Narayan, 2015). All of these simulations lead to an accretion disk that is both optically and geometrically thick. This highly accreting, geometrically thick scenario could lead to optically thick outflows that restrict the emitted radiation to a funnel-like space. A jet from near the black hole could then be able to clear out some of the inner flow and could potentially give us a line of sight towards the central X-ray emitting region (McKinney et al., 2015).

If 1H 0323+342 were to have a relatively high accretion rate, its accretion disk would not be infinitesimally thin. Since radio observations point to a low-inclination geometry, the blue-shifted iron line we observe could be caused by radiation-driven outflows in the funnel, and since the presence of the jet would be exposing the central region, gravitational redshifts could also be used to explain the broadening of the line. Kara et al. (2016) develop a simple model for iron line reverberation in a funnel geometry where special relativistic effects and gravitational redshift are taken into account, and where only an outflow velocity profile for the funnel walls is considered. Through Monte Carlo simulations, they show that an iron line can indeed be blueshifted and broadened due to reflection off an optically thick outflow.

A very recent study by Thomsen et al. (2019) makes use of this funnel geometry to make a detailed comparison between the iron line profiles of thin disks and those of a geometrically thick supper-Eddington disk. In particular, they show that, in each type of disk, photons emitted from different radii have different contributions to the line profile. They show that for thin disks, most of the flux comes from radii less than $25R_{\mathrm{g}}$, since the emissivity profile drops relatively quickly at larger radii. However, for a funnel geometry, more photons are emitted between $25 - 50R_{\mathrm{g}}$ because the reflected flux does not decrease as quickly at large radii, due to the fact that in this geometry, the emission from the corona would be able to illuminate more of the disk at larger radii than it would for a thin disk. In addition, they show that the iron line profiles of the thick disk are significantly more blue-shifted than those of the thin disk, for reasons mentioned earlier.

We can test if 1H 0323+342 would be an adequate candidate for a thick-disk model by performing a quick calculation to estimate its Eddington rate using our data. We use the 2-10 keV luminosity from our best fit model to estimate the latter. After performing this calculation, we arrive at a value of $\log(L_{2-10\ \mathrm{keV}})$=43.8. Adjusting the appropriate value in ergs s^{-1} by a bolometric correction of ∼20 (Vasudevan & Fabian, 2007) to get the bolometric luminosity $L = \eta \dot{M} c^2$, we then divide by the Eddington luminosity. As in our timing analysis, we use the mass $M_{\mathrm{BH}} = 1.9^{+0.4}_{-0.3} \times 10^7 \mathrm{M}_{\odot}$ obtained by Landt et al. (2017). Our result is then $L \sim 0.5^{+0.2}_{-0.1} L_{\mathrm{Edd}}$. The values we calculate here are comparable to the luminosity and Eddington ratio values obtained in Kynoch et al. (2018) and several other previous works (e.g., Paliya et al., 2019a, 2014; Pan et al., 2018; Landt et al., 2017). Although this ratio does not imply super-Eddington accretion, it does represent a relatively high accretion rate.

It is important to note that the bolometric correction we use is really an average obtained for Eddington ratios $\lesssim$0.1. Vasudevan & Fabian (2007) show that the correction seems to increase with Eddington ratio, and discuss that it may vary considerably between different objects, in particular when it comes to sources like NLS1s and RL AGN. In fact, according to Vasudevan & Fabian (2007), for high-Eddington AGN, the bolometric correction is closer to 60. Given the high accretion rate of NLS1s, this could mean that 1H 0323+342 may have an Eddington ratio as high as ~ 1.5. Our results seem to suggest that these are the physical phenomena that are relevant for the case of 1H 0323+342.

2.5 Conclusions

We have presented X-ray spectral and timing analyses of the γ-NLS1 1H 0323+342 with a combination of the first simultaneous *XMM-Newton* and *NuSTAR* campaign and archival data. Our main results are as follows:

1. We definitively measure a broad iron line and a Compton hump in 1H 0323+342. The broad line extends from $\sim 5.5 - 8$ keV, meaning that there are significantly blueshifted and redshifted components of the line.

2. We attempt describing the data with a variety of absorption and reflection based models. We find that the X-ray emission in the 0.5-79 keV range (soft excess and iron line) is well described by a combination of a phenomenological blackbody component and relativistic reflection model, suggesting that the dominant form of the X-ray emission comes from the corona in the vicinity of the black hole.

3. We find potential evidence of a hard excess at high energies, suggesting that non-thermal jet emission contributes yet another component to the hard X-ray spectrum.

4. Our measurement of the inclination using a razor-thin disk model is definitively in tension with radio observations at a significance of $>$99.99%; this measurement can be explained by the detection of a blue-shifted line in the spectrum. However, the discrepancy might be reconciled by considering a model that takes into account a geometrically thick accretion flow.

Chapter 3: Long-term hard X-ray variability properties of *Swift*-BAT blazars

In this chapter, we present results from the first dedicated study in the time domain of the hard X-ray variability behavior of blazars on long timescales based on $\sim$13 years of continuous hard X-ray data in the 14-195 keV band. We use monthly-binned data from the recent 157-month *Swift* Burst Alert Telescope catalog to characterize the hard X-ray variability of 127 blazars and search for potential differences between the variability of BL Lacertae objects (BL Lacs) and flat-spectrum radio quasars (FSRQs). A significant portion of the blazars in the sample ($\sim$37%) do not show statistically significant hard X-ray variability on monthly timescales, which is deeply at odds with previous studies that show that blazars are highly variable in the X-rays and other energy bands on a wide range of timescales. We also find that, on average, the FSRQs and BL Lacs for which we do detect variability exhibit similar flux variability ($\langle F_{\rm var}\rangle = 76 \pm 5\%$ vs $\langle F_{\rm var}\rangle = 75 \pm 4\%$); this suggests that the variability in these FSRQs is not necessarily primarily driven by variations in the source function of scattered external radiation arriving from extended regions, and that it is instead possibly driven by processes such as shocks in the jet that lead to variations in particle injection. In addition, only five blazars in our sample (3C 273, 3C 454.3, Mrk 421, Mrk 501, and 1ES 0033+595) show significant spectral variability in the long-term light curves. For 3C 273, Mrk 421, and Mrk 501, we find that a power law that changes slope on monthly timescales is sufficient to characterize the variable hard X-ray spectrum, suggesting that, at least for some of the brightest blazars, the long-term spectra in the hard X-rays may be described in a relatively simple fashion.

3.1 Introduction

Active galactic nuclei (AGN) are known to exhibit intrinsic stochastic variability on a wide range of timescales, and the study of such variability provides insight into the physical processes and structures associated with the emitting source. Blazars are radio-loud (RL) AGN characterized by having a jet pointed close to the line of sight of the observer. The particles in the jet move with bulk relativistic speed $v = \beta c$ towards the observer, and as a result emission originating in the jet is relativistically boosted in the direction of motion. More specifically, an observer at rest will detect a broadband flux that scales as $F = \delta^4 F'$ compared to the emission in the co-moving frame of the jet, where $\delta = [\Gamma(1 - \beta\cos\theta)]^{-1}$ is defined as the Doppler factor, and Γ and θ are the bulk Lorentz factor and viewing angle, respectively (Urry & Padovani 1995). These conditions therefore lead to emission in the observer's frame that is much more powerful than if the jetted particles were at rest; consequently, over the past several decades, the mostly non-thermal emission from blazars has been characterized by high luminosities, as well as by high-amplitude, rapid variations in flux, spectra, and polarization across most timescales and wavelengths (see e.g. Stein et al., 1976; Blandford & Rees, 1978; Angel & Stockman, 1980; Marscher & Gear, 1985; Morini et al., 1986; Feigelson et al., 1986; Wagner & Witzel, 1995; Ulrich et al., 1997; Andruchow et al., 2005; Lichti et al., 2008; Soldi et al., 2014).

In general, blazars can be classified into two categories: BL Lacertae (BL Lac) objects and flat-spectrum radio quasars (FSRQs). Historically, the distinction between these two types has been based on the rest-frame equivalent width (EW) of optical emission lines: FSRQs exhibit broad emission lines in their optical spectra (EW>5Å), while BL Lacs have featureless optical spectra or spectra with weak emission lines (Stickel et al., 1991). The two subclasses can also be distinguished via their spectral energy distributions (SEDs). The SEDs of all blazars generally consist of a double-hump structure, with the hump at lower frequencies caused by synchrotron emission from the radio to the ultraviolet (UV)/X-rays and the hump at higher frequencies (X-rays to γ-rays) arising due to inverse Compton processes. In BL Lacs, the two humps are usually nearly equally luminous, and the Compton hump is likely due to the synchrotron self-Compton (SSC) mechanism, where the synchrotron photon field produced by the jet is Compton upscattered by the same highly energetic particles in the jet. For FSRQs, the inverse Compton hump is often significantly more luminous than the synchrotron hump, and is instead believed to be the product of inverse Compton scattering of photons external to the jet (the so-called "external Compton" (EC) process). This has led to a more physical divide between BL Lacs and FSRQs, where the more luminous FSRQs likely exhibit radiatively efficient accretion; this forms a UV-bright disk that photo-ionizes the broad-line region (BLR), which in turn provides the external photon field that is upscattered by the jet (Ghisellini et al., 2009b, 2011). FSRQs and BL Lacs can further be divided based on the frequency of the peak of the synchrotron hump, $\nu_{\rm syn}^{\rm peak}$, leading to the terms "high-synchrotron-peaked" (HSP, $\nu_{\rm syn}^{\rm peak} \gtrsim 10^{15}$Hz); "intermediate-synchrotron-peaked" (ISP, $10^{14} \lesssim \nu_{\rm syn}^{\rm peak} \lesssim 10^{15}$Hz); and "low-synchrotron-peaked" (LSP, $\nu_{\rm syn}^{\rm peak} \lesssim 10^{14}$Hz; Abdo et al. 2010b), with FSRQs usually classified as LSPs and the "blazar sequence" dictating that the bolometric luminosity gradually decreases as one goes from FSRQ/LSP to HSP (Fossati et al., 1998; Ghisellini et al., 2017).

When it comes to the production of the X-rays in particular, the emission mechanisms involved in BL Lacs and FSRQs can naturally lead to differences in the nature of the variability for each type of blazar. For instance, the X-rays in BL Lacs are usually produced by either synchrotron emission or the SSC process (see e.g. Ghisellini et al. 2009b). In this case, the blazar's variability is likely driven by the timescale for the acceleration of particles in the jet as it compares to the timescale of energetic losses by those same particles through either synchrotron or inverse Compton processes. By contrast, as implied earlier, the X-rays in FSRQs are produced by the EC process, where the dominant radiation field corresponds to the photon density of an external component. The variability in these blazars could involve variations in an external photon field that scatters off a quasi-stable particle distribution. The implications that the aforementioned processes have on the characterization of the X-ray variability of blazar subclasses remain a major point of discussion, as differences in variability between different spectral components and between blazar types may provide insight into the physical mechanisms involved in driving the jetted emission.

The X-ray portion of blazar SEDs can generally be well-modeled by a simple power law representing the non-thermal processes occurring in the jet (e.g. Urry et al. 1996; Sambruna et al. 2000; Paliya et al. 2019b), although curvature in the form of a log-parabola or a broken power law has also been detected in a significant number of objects (e.g. Comastri et al., 1997; Kubo et al., 1998; Massaro et al., 2004, 2006; Paggi et al., 2009; Furniss et al., 2013; Arcodia et al., 2018; Dalton et al., 2021). According to many blazar emission models, these curved continua may result from relativistic particle distributions that have a similar shape (see e.g. Sikora et al. 1994, 1997, 2009; Tavecchio et al. 2007; Tavecchio & Ghisellini 2008; Ghisellini & Tavecchio 2009, 2015; Arcodia et al. 2018). In addition, some sources have shown a "harder-when-brighter" trend (i.e. the spectrum flattens as the source brightens, e.g. Zhang et al. 2006; Soldi et al. 2014; Hayashida et al. 2015; Pandey et al. 2017; Bhatta et al. 2018), possibly due to an increased contribution of a hard tail produced by the jet when the source is in a brighter state. The behavior of blazar X-ray spectra is therefore expected to be fairly variable.

Blazar variability analyses in the X-rays have been instrumental in helping constrain the jet physics involved in these sources, both in multi-wavelength and X-ray-focused studies (see e.g. Worrall & Wilkes 1990; Urry & Padovani 1995; Urry et al. 1996; Takahashi et al. 1996; Ulrich et al. 1997; Sambruna et al. 2000; Pian 2002; Zhang et al. 2005, 2006, and references therein). While most of these analyses focused on X-ray observations taken within the "classical" 0.3-10 keV range, recently, the hard X-rays ($\gtrsim 10$ keV) in blazars and beamed AGN have been studied more extensively than in the past (e.g. Madsen et al. 2015; Hayashida et al. 2015; Rani et al. 2017; Bhatta et al. 2018; Rani et al. 2022). The origin of the hard X-ray emission discussed in these studies may provide insight into the physics occurring in the innermost regions located near the base of the jet, with some sources serving as potential laboratories to probe the elusive disk-jet connection (Sbarrato et al. 2016; Chatterjee et al. 2018). However, most of the work on blazars in the X-ray band has historically been heavily biased towards bright sources and/or sources in bright/active states; in the hard X-rays in particular, studies have also been limited to relatively shorter timescales (due to the observing strategies of the available hard X-ray telescopes and their limited field of view), thus leaving an incomplete picture of the X-ray variability behavior of blazars.

The Burst Alert Telescope aboard the *Swift* observatory (*Swift*-BAT) has a very wide field of view ($\sim 60^\circ \times 100^\circ$), and its main objective is to detect transient gamma-ray bursts (GRBs) with a coded-aperture mask telescope. However, as it searches for GRBs and other transients in the hard X-rays, it also continuously observes the sky, performing an all-sky hard X-ray survey in the 14-195 keV band (Tueller et al. 2008, 2010). The recent release of the 105-month catalog (Oh et al. 2018), as well as the pending publication of the 157-month survey[1] (Lien et al. in prep), are unique in that they provide continuous, well-sampled observations over a $\gtrsim 9$-year timescale for a hard X-ray selected sample of sources, and thus sample the time variability of these objects in a previously unexamined time domain. Due to the wide field of view and moderate sensitivity, this survey yields data for over 1600 sources that have been detected since ∼December 2004, ∼1000 of which are AGN, and 158 of which are classified as "beamed AGN". The BAT catalog therefore currently boasts the largest sample of AGN observed in the hard X-rays on long timescales, with a wide range in redshift and luminosity exhibited across the AGN listed in the catalog.

In this chapter, we aim to remove some of the bias towards bright blazars seen in past X-ray studies by studying 127 blazars from the 157-month BAT catalog (regardless of their brightness) and performing the first dedicated study of the hard X-ray variability of blazars on long timescales based on ∼13 years of *Swift*-BAT data. The structure of the chapter is as follows: we describe our sample selection and the BAT data and their filtering in Section 4.2, present our variability analysis and its results in Section 4.3, and discuss our results in Section 3.4.

3.2 *Swift*-BAT sample selection and data filtering

In the more recent *Swift*-BAT catalogs, the "QSO" type is replaced with either "Seyfert" or "beamed AGN" depending on the properties of the optical emission lines in the literature, and the Roma blazar catalog BZCAT (Massaro et al. 2009) is also used as a reference to classify beamed AGN (see e.g. Oh et al. 2018). This classification yields 158 sources that are defined as "beamed AGN" in the BAT 157-month catalog. However, not all of these sources show the spectral shape

[1]https://swift.gsfc.nasa.gov/results/bs157mon/

that is expected of a blazar in their SEDs. As in Paliya et al. (2019b), we exclude sources for which this is the case and therefore end up with a sample of 127 blazars for our analysis.

As for previous catalogs (see e.g. Tueller et al. 2010; Baumgartner et al. 2013), the 157-month catalog data reduction is carried out by extracting data in eight energy bands (14–20 keV, 20–24 keV, 24–35 keV, 35–50 keV, 50–75 keV, 75–100 keV, 100–150 keV, and 150–195 keV) from a single snapshot image; the data from each snapshot are then combined into all-sky mosaic images, which in turn are combined to form a total-band map, and a blind search for sources in the 14-195 keV band images is performed with a 4.8σ detection threshold. Monthly- binned light curves are generated by creating monthly, all-sky total-band mosaic images, and then extracting the mosaic fluxes for each month for all sources detected in the full survey. The catalog includes monthly light curves for the total 14-195 keV BAT band, as well as light curves divided by the eight BAT bands; these are the data we use to conduct our long-timescale variability analyses.

As in Soldi et al. (2014), we filter the light curves by excluding any data points with exposure times shorter than one day. In order to filter out points with very large error bars, we also inspect the histogram of the flux uncertainties of all light curves in logarithmic space to determine where the high-value tail of the distribution begins. However, we find that for the most part, each of these two flags accounts for the same data points, so we use the flag on the exposure time as our main filter for the BAT monthly data (see Figure 3.1 for examples of the filtered light curves).

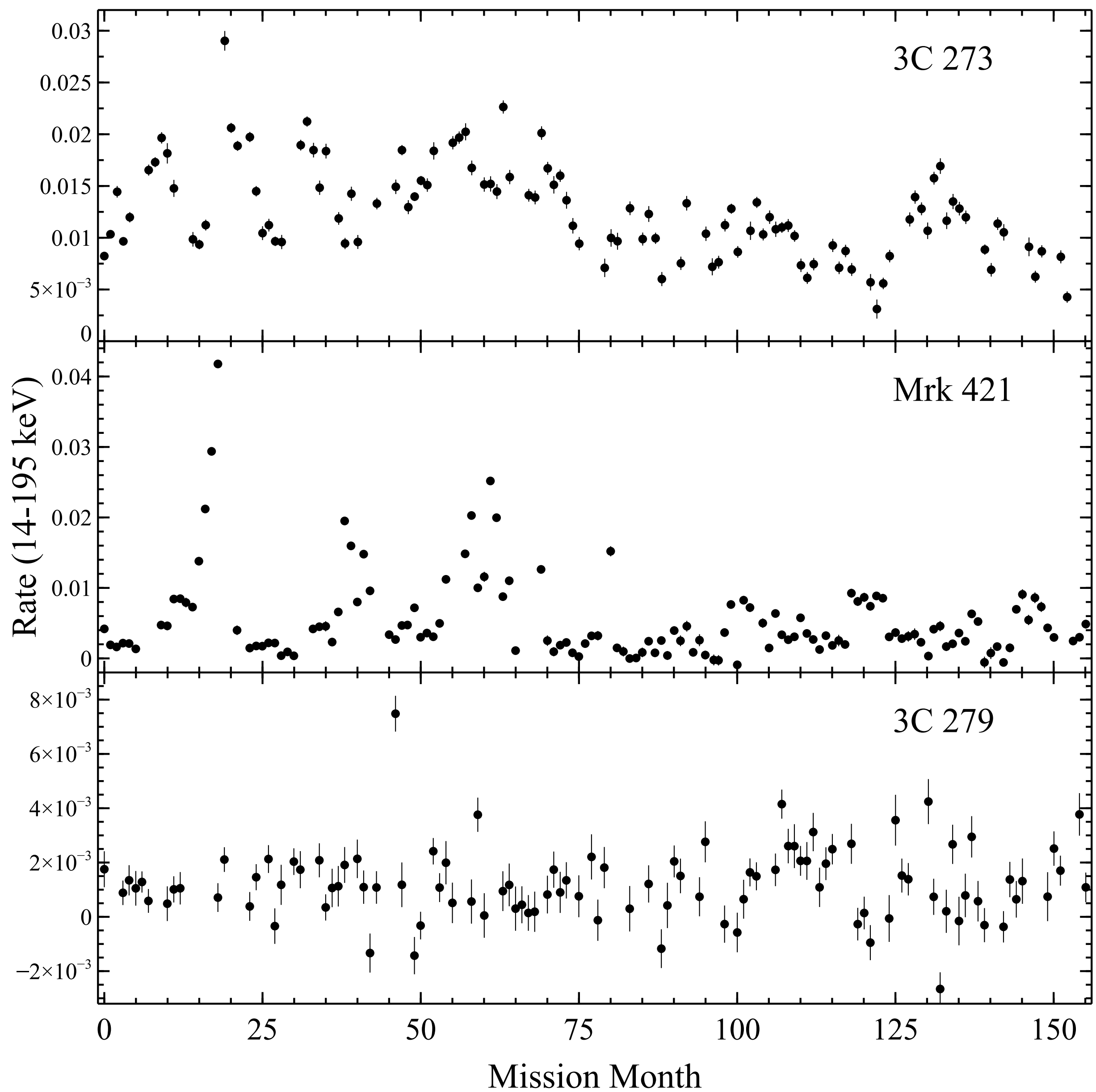

Figure 3.1: Examples of filtered monthly-binned light curves for 3 well-known blazars from the 157-month catalog in the 14-195 keV band. We exclude points for which the exposure is <1 day. Mission month 0 corresponds to the first month of the *Swift*-BAT survey observations, namely December 2004 (see e.g. Oh et al. 2018).

3.3 Results

3.3.1 Flux variability analysis in the 14-195 keV band

We initially estimate the variability in our sources by fitting the 14-195 kev total band monthly light curves with a constant function, and then applying a χ^2 test. The criterion that we set to represent a significant detection of the variability is $p_{\chi^2} < 5\%$, where p_{χ^2} is the null-hypothesis probability of obtaining that value of χ^2 if the source were in fact constant. We also quantify the flux variability of our sources by following the methods described in e.g. Vaughan et al. (2003), where the contribution of an additional variance from measurement uncertainties is corrected for. The "excess variance" has been widely used in studies of the variability of accreting objects to estimate the intrinsic source variance (e.g. Nandra et al., 1997; Edelson et al., 2002), and is frequently normalized to directly compare the variance between different sources. The fractional root mean square (rms) variability amplitude $F_{\rm var}$ is defined as

$$F_{\rm var} = \sqrt{\frac{S^2 - \overline{\sigma^2_{\rm err}}}{\overline{x}^2}}, \tag{3.1}$$

where S is the sample variance, $\overline{\sigma^2_{\rm err}}$ is the mean square error, and $\overline{x}$ is the mean of the light curve. The quantity $F_{\rm var}$ is the square root of the normalized excess variance, and has the added benefit of being a linear statistic, thus allowing for the representation of the rms variability amplitude in percentage terms; this is the quantity we will use here, written as a percentage.

Upon applying the above methodology, we find that 6 sources exhibit a fractional variability that ends up being much higher than expected ($\gtrsim$240%) upon inspection of their light curves. We believe that, for these sources, the high value of $F_{\rm var}$ is due to the fact that $\gtrsim$40% of the data points correspond to negative count rates, implying a mean flux that is very close to 0; when we inspect their light curves, we do not see significant variability in the amplitudes, especially when taking into account their uncertainties. We therefore exclude these 6 sources from the rest of the analysis due to their relatively low signal-to-noise (S/N) data (for a list of the remaining 121 sources, see Table 3.1).

We also find that a significant fraction (∼37%) of our sample of blazars does not show statistically significant variability on monthly timescales. For the vast majority of the objects in this sub-sample, we cannot measure $F_{\rm var}$ because we calculate a slightly negative normalized excess variance (i.e., the uncertainties are slightly larger than the sample variance), suggesting that any variation in the amplitudes is fairly low. This is surprising, since it has been established from past studies that the emission from blazars is extremely variable at almost every timescale and wavelength. It is important to note, however, that the BAT has a relatively low sensitivity per unit time (Tueller et al. 2008), and that it is not clear from the BAT data alone if the lack of variability we observe is actually a result of relatively constant emission. In a joint analysis with *NICER* data (Mundo & Mushotzky 2023), we show that, for at least 4 of the sources in this sub-sample, there is in fact detectable variability on monthly timescales and shorter, but that it is significantly lower-amplitude than what is expected of blazars (see Sec. 3.4 for further discussion).

We divide the remaining blazars for which we can detect statistically significant variability (76 total) into BL Lacs and FSRQs based on the classification in the BZCAT catalog (Massaro et al. 2015), as well as on the SEDs in Paliya et al. (2019b). We calculate $F_{\rm var}$ for each population (we use this sample for the rest of the analysis). The $F_{\rm var}$ distributions for each blazar type are shown in Figure 3.2, produced by using a kernel density estimate (KDE) of their probability

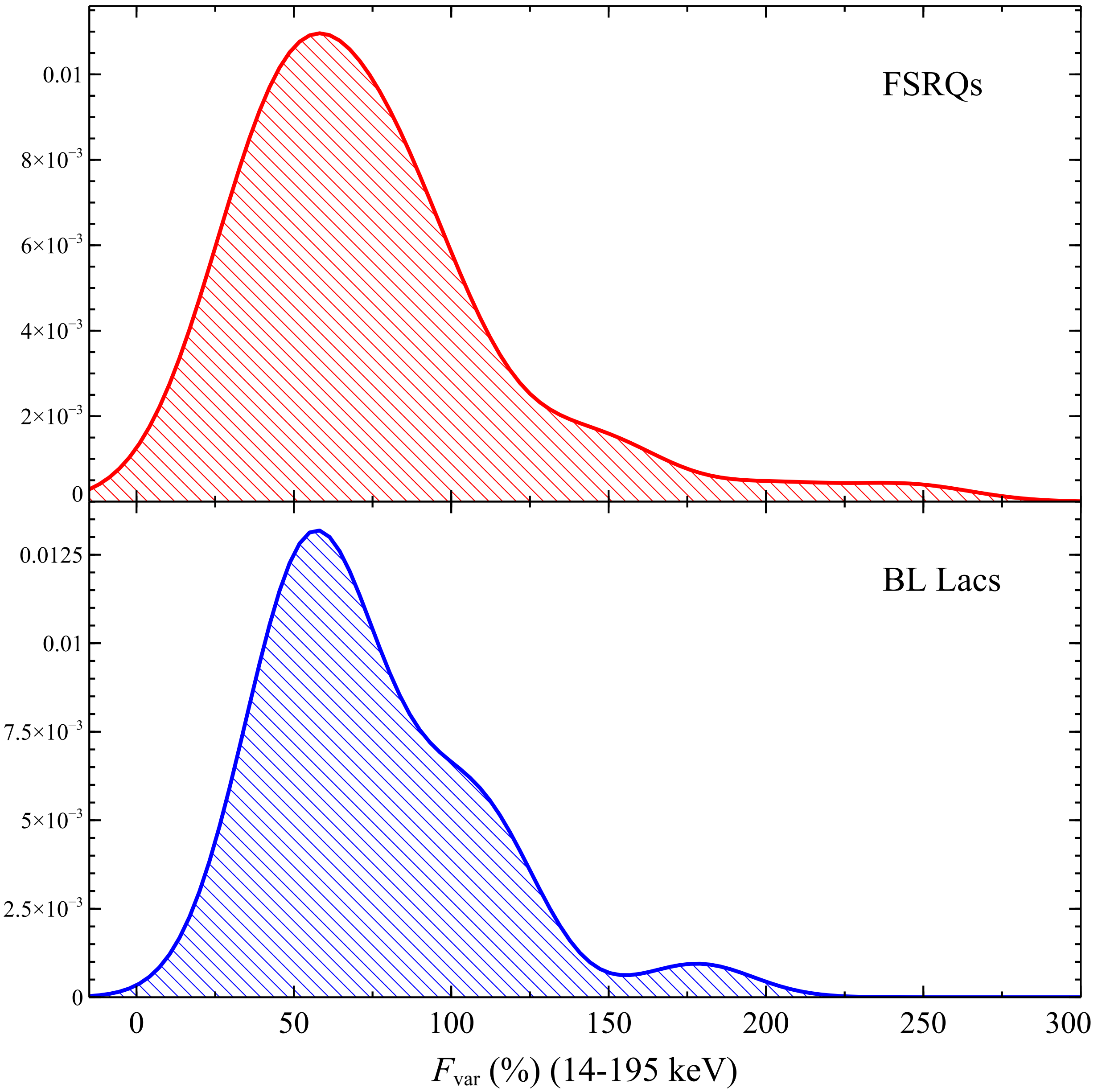

Figure 3.2: KDE distributions for $F_{\rm var}$. A KS-test shows that the two distributions are likely not significantly different, i.e. they may be drawn from the same parent population.

density functions[2]. We find that, within error bars, the variability between the two blazar types is practically the same, with mean $F_{\rm var}$ values of 76±5% and 75±4% for FSRQs and BL Lacs, respectively. Given that the distributions are fairly skewed, we also report the median values to compare the distributions, and find that these are identical (both 65%). A Kolmogorov-Smirnov (KS) test confirms that the two distributions are likely not significantly different at the 95% confidence level (KS statistic = 0.18, p value = 0.60). Since, for most FSRQs, the X-ray emission is produced via the EC mechanism, one might expect an overall lower variability compared to BL Lacs; the reason for this is that the variability would be caused by variations in the scattered external radiation field, which arrives from extended regions such as the BLR and dusty torus, and would thus involve longer timescales and less rapid variations. Our results suggest that it is possible that the variability in FSRQs may instead be driven by variations in the particle energy distribution and particle injection processes.

3.3.2 Correlation analysis

In order to test for possible trends between the hard X-ray variability and some of the main properties of the 76 variable blazars in our sample, we correlate the fractional variability with the luminosity in the BAT band, black hole mass, Doppler factor, and the photon index Γ from the time-averaged spectra in the 14-195 keV band, for the BL Lac and FSRQ populations separately. We use the FSRQ black hole mass estimates and the Doppler factors for both populations from Paliya et al. (2019b), as well as the BL Lac masses estimated via the properties of the host galaxy

[2] In this chapter, we visualize our distributions with KDEs. Each data point in the sample is assigned a specific kernel, and the corresponding densities are then summed together. Here we choose a Gaussian kernel with bandwidth corresponding to "Scott's Rule" (Scott 1992), i.e. width $= N^{-1/5}$ (N is the number of data points). The benefit of using KDEs over regular histograms is that in the latter, the appearance can change based on the binning properties; a KDE only depends on the kernel width.

Table 3.1: Sample of 121 blazars used in this study, along with associated properties. 76 of these blazars are used in the correlation analysis between $F_{\rm var}$ and the last 4 parameters in this table. (1) is the blazar name; (2) is the blazar type; (3) is the source redshift; (4) is the luminosity in the BAT band; (5) is the black hole mass estimate, gathered from the literature if available; (6) is the Doppler factor (from Paliya et al. 2019b); (7) is the spectral index for the time-averaged spectra in the BAT band; (8) is the fractional variability. Empty entries are meant to indicate that the parameters were not readily found in the literature. Sources for which we do not detect statistically significant variability have a dash in column (8). The full list of sources can be found in the electronic version and in the 157-month BAT catalog.

Name	Blazar Type	z	$L_{14-195\ \rm keV}$	$\log(M_{\rm bh})$	δ	$\Gamma_{14-195\ \rm keV}$	$F_{\rm var}$ (%)
(1)	(2)	(3)	(4)	(5)	(6)	(7)	
Mrk 1501	FSRQ	0.0893	44.78	8.70	9.5	$1.82^{+0.22}_{-0.21}$	59±9
1ES 0033+595	BL Lac	0.0860	44.68	7.25	13.6	$2.81^{+0.22}_{-0.19}$	111±2
PKS 0101-649	FSRQ	0.1630	45.02	8.70	18.2	$1.58^{+0.54}_{-0.51}$	—
SHBL J012308.7+342049	BL Lac	0.2720	45.41		15.7	$2.94^{+0.61}_{-0.48}$	—
B2 0138+39B	BL Lac	0.0800	44.37			$2.08^{+0.44}_{-0.38}$	55±25
...	...	...	...	...	...	...	...

(e.g. stellar velocity dispersion, fundamental plane relation) in studies such as Woo & Urry (2002) and Woo et al. (2005); we list the black hole masses of the blazars in column (5) of Table 3.1. The masses of ∼9 BL Lacs in this sample are not readily available in the literature. We apply a Spearman rank correlation test to quantify any potential trends.

We plot $F_{\rm var}$ against each of these parameters in the 4 panels in Figure 3.3. While we do not detect any significant correlation between the variability and these parameters for either blazar type (i.e., the probability that a correlation occurs by chance is always > 0.05), the results still provide some potential insights. For instance, the lack of correlation between the variability and both the luminosity and black hole mass is in contrast to the anti-correlations that have been found in past studies within the 2-10 keV band for line-emitting AGN (Seyferts and quasars; see e.g. Barr & Mushotzky 1986; Green et al. 1993; Papadakis & McHardy 1995; Papadakis 2004; Zhou et al. 2010; Kelly et al. 2011, 2013; Ponti et al. 2012). However, it is important to note that these anti-correlations were usually observed in analyses that involved timescales shorter than those

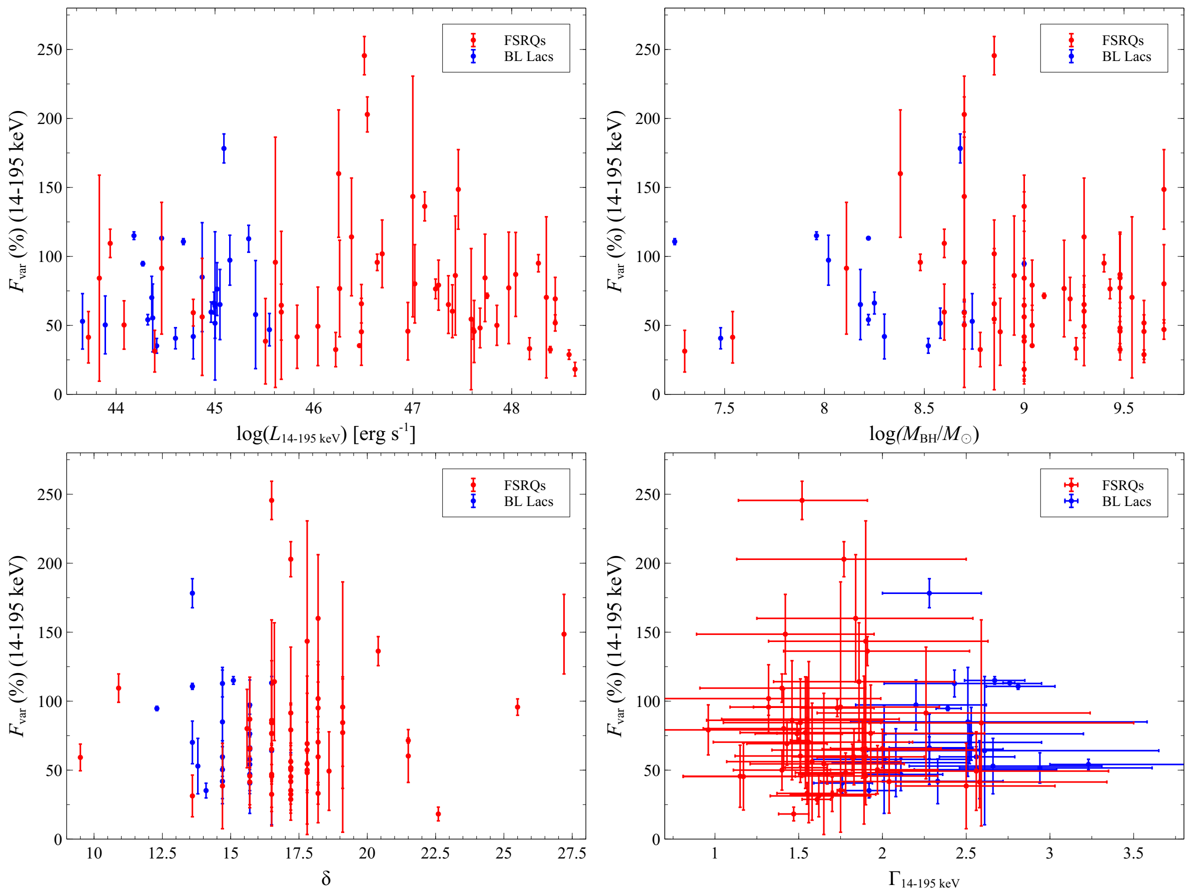

Figure 3.3: $F_{\rm var}$ as a function of the BAT luminosity, black hole mass, Doppler factor, and photon index in the BAT band. We do not find statistically significant correlations between the hard X-ray variability and parameters that represent the properties of the blazars in our sample. (*Note: The fairly high variability ($F_{\rm var}$ $\gtrsim$175%) seen in 3 sources in these plots is not due to low S/N, as was essentially the case for the 6 objects we previously excluded from this analysis.*)

probed by the BAT, and therefore would likely not be detected in this study (see e.g. Markowitz & Edelson 2004; Saxton et al. 2011; Zhang 2011; Soldi et al. 2014 for similar results on longer timescales). In addition, and probably more importantly, the aforementioned studies focused on Seyferts, which of course have very different underlying astrophysical processes associated with their X-ray emission (e.g. disk/coronal emission), and so the trends observed with these sources were usually directly related to the accretion process. It is therefore unclear what should have been expected to begin with when it came to our sample of blazars and their jetted emission (see Section 3.4 for further discussion).

Small changes in jetted emission will be Doppler boosted towards the observer to larger-amplitude variations; one might therefore expect to detect a positive correlation between the Doppler factor δ and the fractional variability. While we do not find such a correlation in our analysis, we do calculate a mean Doppler factor for the FSRQs in our sample that is larger than that for the BL Lacs ($\delta \sim 18$ vs $\delta \sim 15$, respectively). A KS-test shows that the Doppler factor distributions for the two blazar types are significantly different from each other (KS statistic = 0.70, p value $\ll$ 0.05). This suggests that effects related to relativistic beaming may be a significant driving factor for the X-ray variability in these FSRQs, enhancing it to a level detectable by the BAT.

The time-averaged spectra in the 157-month catalog have not yet been calculated, so for the comparison with the photon index Γ, we assume that the time-averaged spectra have not changed drastically over long timescales and therefore use the values for Γ available in the previously published 105-month catalog[3]. The lack of correlation we observe here on monthly timescales is interesting since, naively, one might expect steeper indices to be indicative of radiative losses

[3]https://swift.gsfc.nasa.gov/results/bs105mon/

that may lead to significant flux variability. Our results suggest that, on these longer timescales, energetic losses may not be the origin of the variability.

3.3.3 Spectral variability analysis

In order to detect potential variations in the spectra of our sources, we make use of the monthly light curves that are divided into the eight individual BAT bands. In addition to the filtering mentioned in Sec. 2, we also exclude months where the total-band count rate is negative to maximize the S/N for this particular analysis.

3.3.3.1 Hardness ratio calculations

We quantify the spectral variability by calculating different hardness ratio (HR) time series. To set up the HR calculations, for each month, we bin the eight BAT channels into three bins with similar average S/N over time. The reason for re-binning each monthly spectrum is two-fold: firstly, we would like to maximize the S/N before calculating the HRs. Secondly, having three bins would allow us to investigate the spectral variability in more detail, as it would allow for the calculation of at least three different simple hardness ratios. This results in the following channels: a "low" (L) channel from 14-24 keV, a "medium" (M) channel from 24-50 keV, and a "high" (H) channel from 50-150 keV. We exclude the 150-195 keV channel due to its very low S/N. The relevant hardness ratios for this analysis are therefore $\frac{H}{L}$, $\frac{H}{M}$, and $\frac{M}{L}$.

As in the flux variability analysis, we fit each of the HR time series with a constant, and a χ^2-test is applied, with the null hypothesis stating that the time series can be fit with a constant. Again, we define objects that show spectral variability are those for which $p_{\chi^2} < 5\%$. Upon

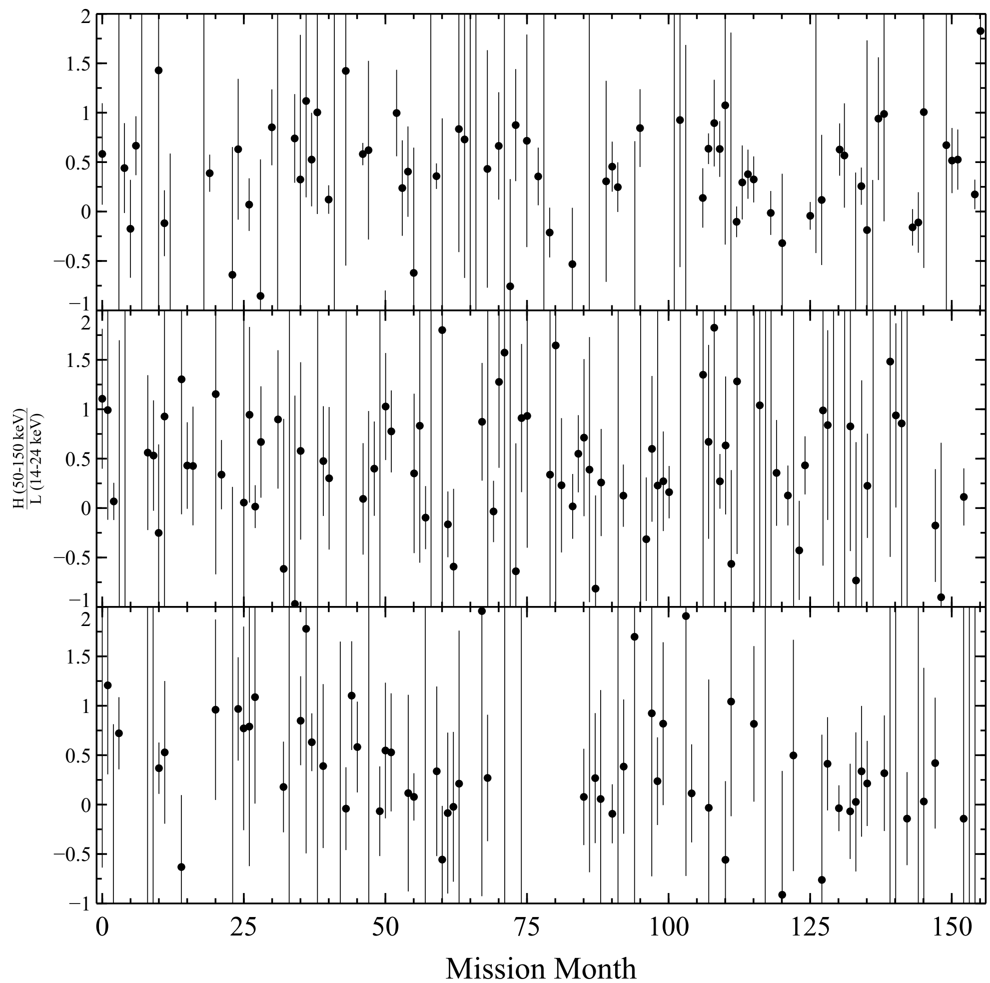

Figure 3.4: Most of the blazars in our sample do not show spectral variability on monthly timescales according to a χ^2-test. Here, we show 3 blazars (top to bottom: 3C 279, 4C +04.42, B2 0743+25) for which this is the case, by showing the time series for the $\frac{H}{L}$ hardness ratio as an example. For the vast majority of the blazars, we do not detect statistically significant spectral variability due to the relatively low S/N of their eight-band light curve data; at times, there are also insufficient variations between the amplitudes of the points.

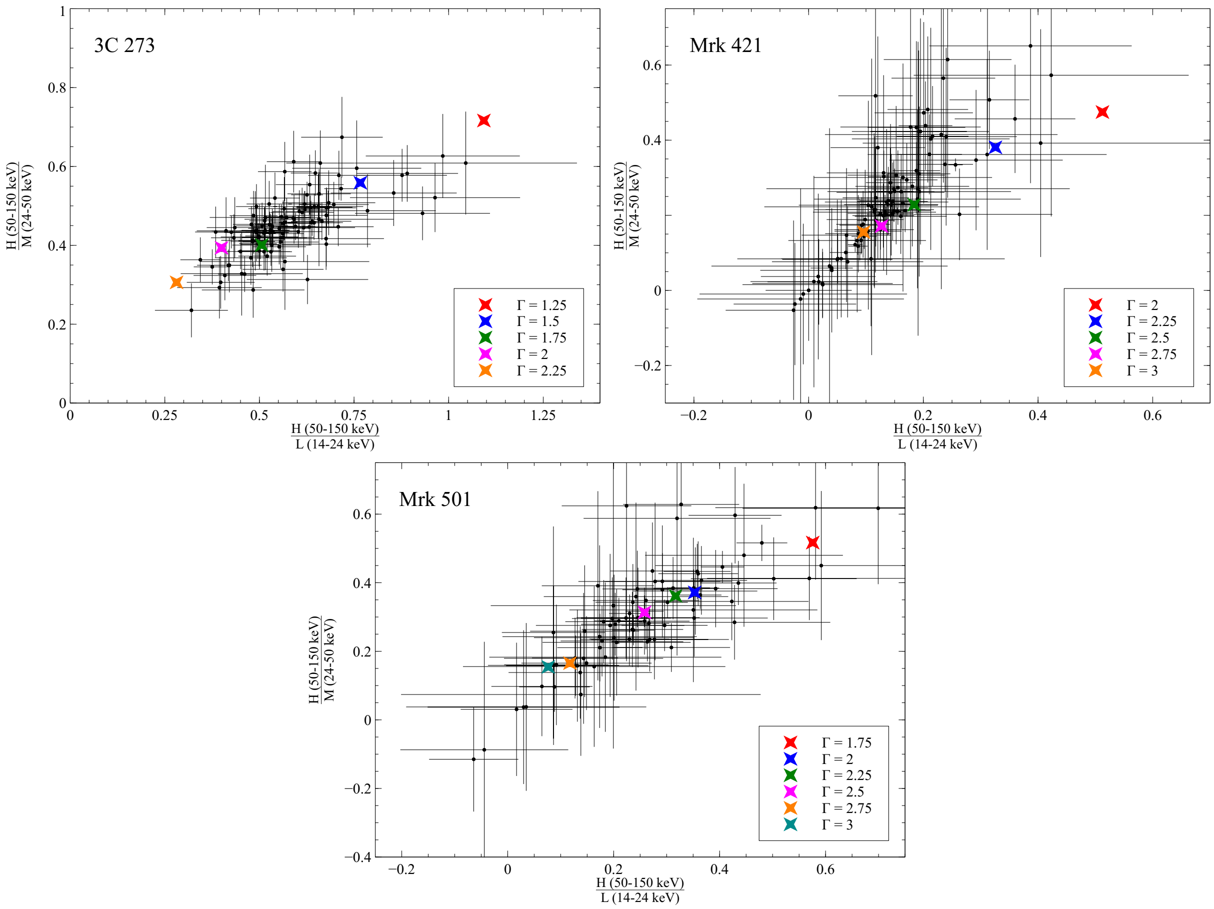

Figure 3.5: HR planes for 3C 273, Mrk 421, and Mrk 501. The points calculated from the power law simulations (colored crosses) track the trend in the hardness ratios, suggesting that the spectra for these sources can be described with a simple power law that is variable on monthly timescales.

applying this test, we find that only 5 sources (3 BL Lacs, 2 FSRQs) show spectral variability. This is once again in tension with the literature, which states that blazars on average can exhibit significant variability in their spectra; it is therefore surprising that we do not detect spectral variability for the vast majority of our sources in these long-term data. However, it is also possible that the BAT is simply not sensitive enough to detect such changes most of the time (see Figure 3.4 for examples).

For the 5 sources that do show spectral variability (3C 273, 3C 454.3, Mrk 421, Mrk 501, and 1ES 0033+595), we extend the analysis further by attempting to characterize the nature of the changing spectrum on timescales of a month with a specific model. We decide to do this by plotting two of the calculated HRs against each other to form a "HR plane" (see Figure 3.5 for examples); this essentially allows for an analysis of the monthly spectral data using only hardness ratio values, independent of time. Using the "fakeit" command on XSPEC v12.12.0g (Arnaud 1996), we then simulate monthly BAT spectra based on a simple power law, the simplest possible model for the X-ray emission of AGN. More specifically, we use the "pegpwrlw" model in XSPEC and the time-averaged 14-195 keV flux (in erg cm^{-2} s^{-1}) of our sources to construct the simulated spectra. The simulations are performed with different power law slopes for each source, with Γ ranging from $\sim$1 to 3, which is the typical range of photon indices of AGN in the BAT catalog. With these fake spectra, we can then calculate the HRs as we have done for the monthly data, and we plot the simulated HR values on the HR plane, shown as colored crosses in Figure 3.5.

For 3 blazars, we notice a visual positive correlation between the $\frac{H}{L}$ and $\frac{H}{M}$ ratios from the data. We confirm this with a Pearson correlation analysis, with correlation coefficients of 0.70 for 3C 273 and 0.88 for both Mrk 421 and Mrk 501, all at a significance of >99.99%. As shown in Figure 3.5, the simulated points agree with the correlation in the data, suggesting a variable spectrum described by a power law with a photon index that changes on a month-to-month basis.

We find that when using the HR plane method, we cannot conclusively describe the spectra of either 3C 454.3 or 1ES 0033+595 in the same way. We should note, however, that these sources are also different in that they show statistically significant variability for only two of the hardness ratios that we calculate, namely $\frac{M}{L}$ and $\frac{H}{L}$. The fact that these are the two ratios that vary suggests that these spectra may require at least a changing broken power law with a pivot at $\sim$25-30 keV in order to adequately describe their variability. However, the BAT data do not have a high enough S/N to be able to be described by such a complex model, as compared to a simple power law.

3.3.3.2 Extracting values of Γ from the hardness ratios

For the 3 sources whose spectra can be described by a power law, we push the spectral analysis even further. Since we have calculated the HRs for the data, as well as those for the simulated points based on a power law, we have the necessary tools to extract values for the photon index Γ for each monthly data point from the monthly HR values. In order to do this, we plot either HR against the slopes used in the simulations, and find a relation for each source for the power law slope as a function of the HR. We show distributions for the values of the photon index for these 3 sources in Figure 3.6, as well as the photon index time series in Figure 3.7. It is clear from these plots and their mean values that the extracted values for Γ agree with where in the HR plane the HRs cluster relative to the simulations. We also note the difference in the distributions between 3C 273 (an FSRQ) and Mrk 421, Mrk 501 (BL Lacs, both HSPs); this is consistent with the fact that FSRQs/LSPs generally have flatter spectra, due to the X-rays falling on the rising part of the high-energy hump in the SED (see e.g. Ghisellini et al. 2017; Paliya et al. 2019b, and Figure 3.3).

We also investigate how the spectra change with brightness, and we show the photon index as a function of the normalized 14-195 keV flux for these sources in Figure 3.8. We do not find a statistically significant trend for either 3C 273 or Mrk 421, but for Mrk 501, we detect a "harder-when-brighter" behavior at a significance of $>99.98\%$, possibly associated with increased particle injection that hardens the particle energy distribution, resulting in a flatter emitted spectrum.

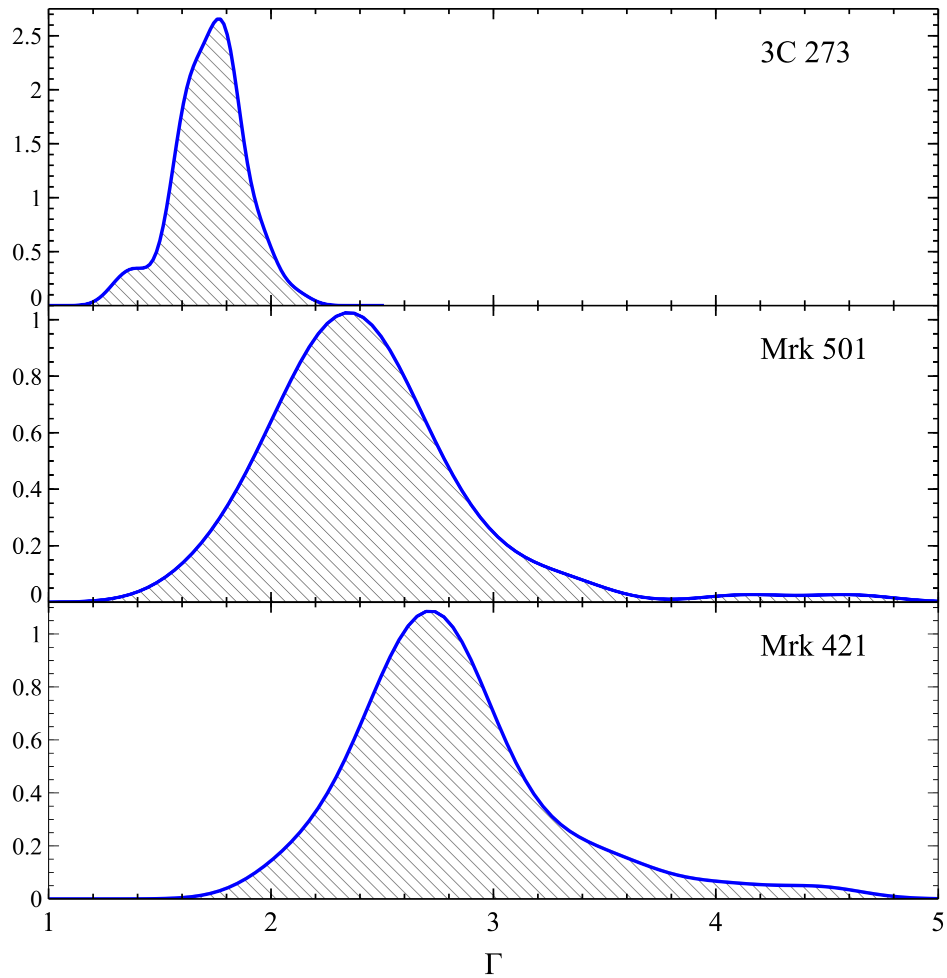

Figure 3.6: KDE distributions for Γ; the peaks of the distributions agree with the portions in the HR planes that are the most heavily populated with the data points As expected, 3C 273, an FSRQ, has overall a flatter spectrum, given that the X-rays are likely produced via the EC process, which has a hard spectral shape in the X-rays. By contrast, the X-rays in the two BL Lacs shown (both HSPs) are produced via synchrotron emission and lie on the tail of the synchrotron hump in the SED (see e.g. Paliya et al. 2019b).

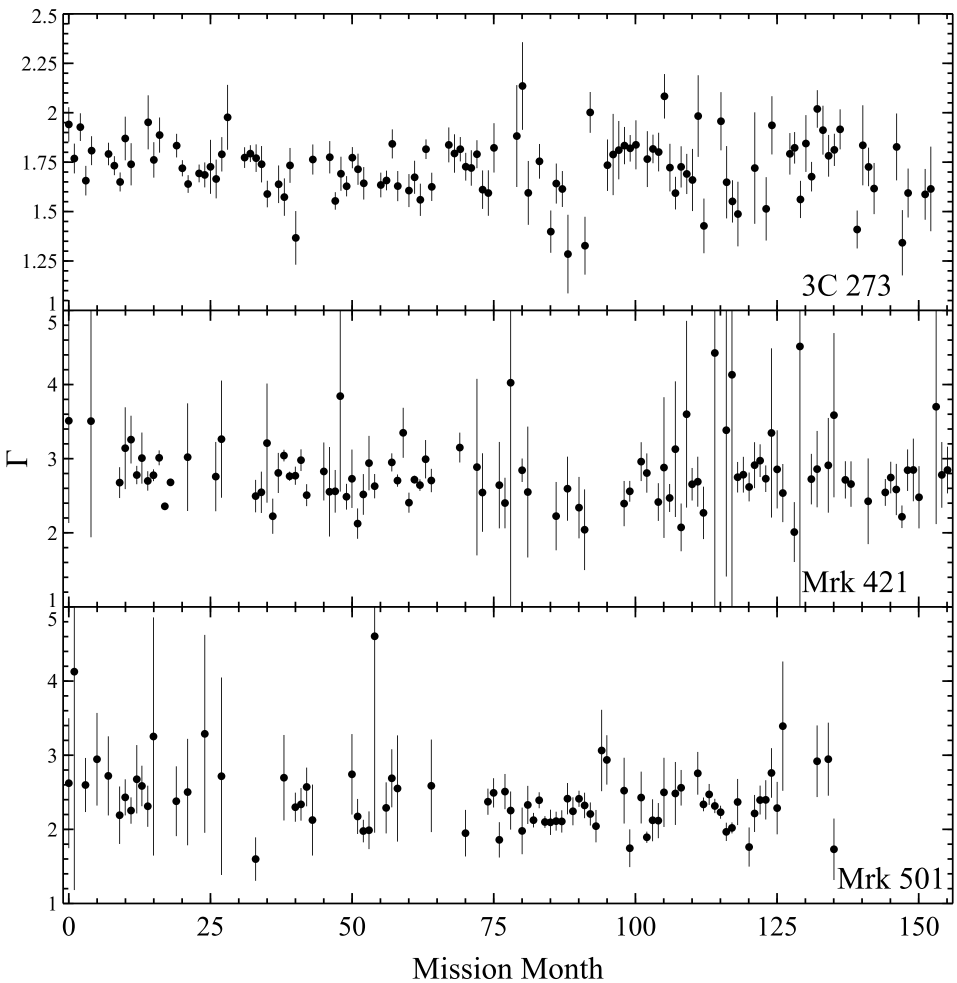

Figure 3.7: Photon index time series for 3C 273, Mrk 421, and Mrk 501. The values agree with the data in the HR plane plots, as well as the distributions; the data points missing at the end of the Mrk 501 light curve are due to the filtering of very low S/N points that have a total-band negative count rate.

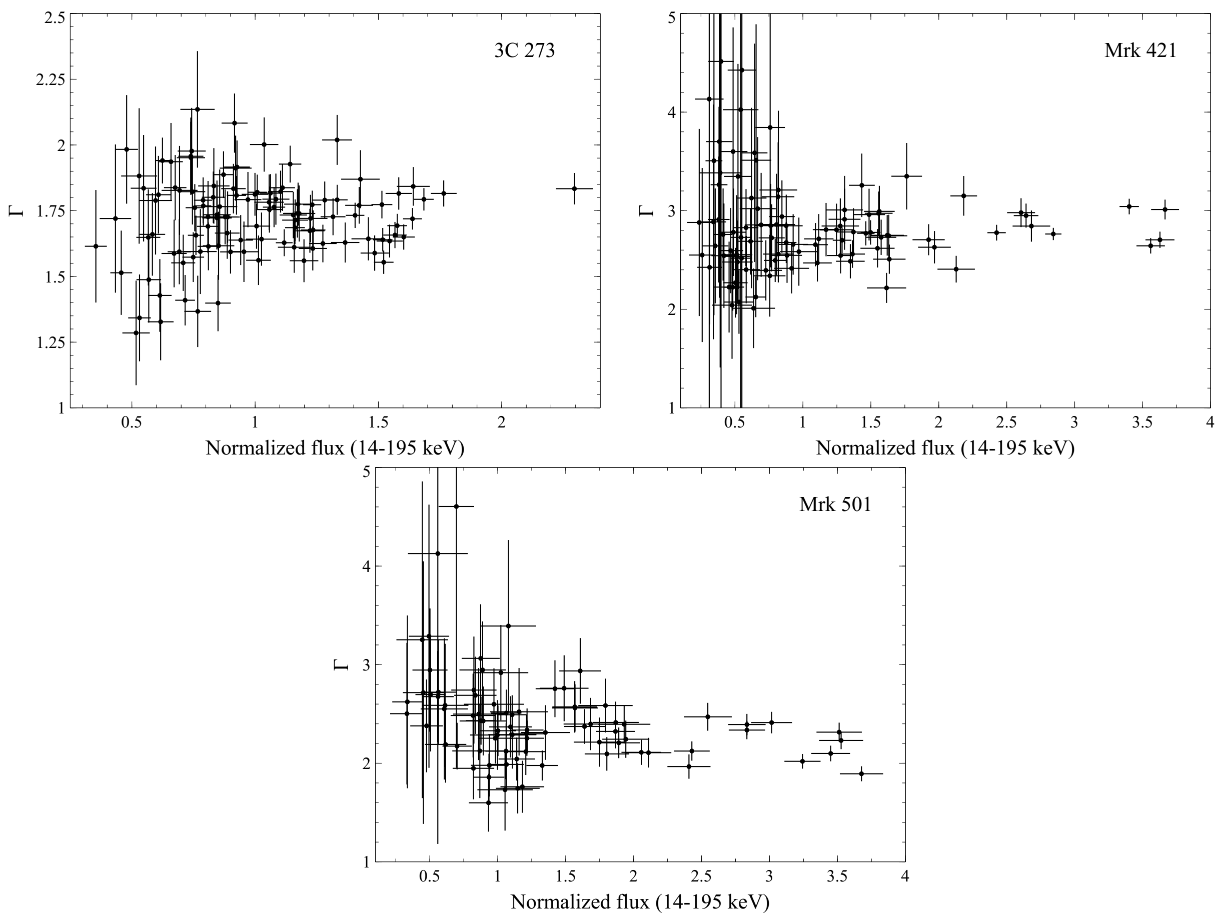

Figure 3.8: Γ as a function of the normalized flux for 3C 273, Mrk 421, and Mrk 501. We do not detect any correlation for 3C 273 or Mrk 421. The Mrk 501 data reveals a "harder-when-brighter" trend, at a significance of $>99.98\%$.

3.4 Discussion

3.4.1 Towards a more complete view of the X-ray variability of blazars

Blazars have historically been described as extremely variable objects, showing significant variations in their flux and spectra across many timescales and wavelengths. However, it is well known that most X-ray studies of blazars have been biased towards the brightest sources, and/or towards blazars in active states such as flares. In this study, at least for a hard X-ray selected sample of sources, we attempt to reduce some that bias by analyzing the long-term data of the vast majority of the blazars in the *Swift*-BAT 157-month catalog, which provides a more complete sample of blazars with varying degrees of brightness.

By expanding the flux range covered in such an analysis, we find that it is possible that not all blazars are necessarily as highly variable as originally thought. However, the timescales on which variability is measured can be radically different in the literature, and simply stating that blazars are usually "highly variable" must be qualified by the timescales covered. For this particular study, it is also important to stress that there are two major caveats to consider along with our seemingly surprising results. The first is that it is unclear from just the BAT data if this supposed lack of variability is due to real near-constant emission, or if it is solely due to sensitivity issues of the BAT data, given that the BAT does not have the highest sensitivity per unit time as compared to other X-ray telescopes. The second is that, on very long timescales, it is possible for blazars to exhibit fairly long periods of relative quiescence that are interrupted by flaring events. Indeed, studies such as the ones conducted by e.g. Williamson et al. (2014), Paliya et al. (2015), and Hayashida et al. (2015) suggest periods of relatively constant emission on close to yearly timescales in both the X-rays and other wavelengths, with some sources spending a significant amount of time in a quiescent state, implying mostly low-amplitude emission with occasional flaring events.

In Mundo & Mushotzky (2023), we investigate these potential scenarios for a sub-sample of 4 faint, "quiescent" blazars that were taken from the population for which we did not detect variability that is mentioned in Section 3.1; the study involves the joint use of BAT data and data acquired from the *NICER* observatory. *NICER*'s $>$100 times sensitivity per unit time as compared to the BAT allowed us to probe shorter timescales that may not be detected by the BAT, while also allowing for an estimate of the variability on timescales similar to those of the BAT catalog. In general, the high sensitivity of the *NICER* observatory therefore offered a way to possibly confirm the apparent lack of X-ray variability seen in the BAT data. In that study, we find that variability is in fact detected in the *NICER* band, but that the variations are much lower amplitude than is expected of a blazar and appear to decrease with longer timescales. In addition, joint fits between the co-added *NICER* spectra and the time-averaged BAT spectra suggest that any potential variability between the two bands would be occurring on timescales significantly longer than one year (see Mundo & Mushotzky 2023 for further details). Therefore, for at least 4 of the "non-variable" blazars in this current study, it is possible that the X-ray emission is represented by periods of quiescence that are much longer than the ones typically observed in blazars.

For the 76 blazars for which we can detect statistically significant flux variability, we find that on average the FSRQs and BL Lacs in the sample have very similar $F_{\rm var}$. It is probably the case that our sample sizes are not large enough to confirm this as a general behavior, as we perform this analysis for only 53 FSRQs and 24 BL Lacs (the BAT blazar population in general is dominated by FSRQs). However, Rajput et al. (2020) find similar results for the long-term γ-ray variability of a larger population of FSRQs and BL Lacs. They use data from the third *Fermi*-LAT catalog to show that, for a significantly larger sample size, the variability of FSRQs is in fact significantly higher than that of BL Lacs. FSRQs produce the X-rays via EC effects, meaning that, assuming a leptonic model, external radiation arriving from extended regions like the BLR and dusty torus is inverse Compton scattered by the highly energetic electrons in the jet. In this scenario, due to light travel time effects, one might expect that the variability caused by variations in the external photon fields would be smeared out, leading to an observed overall lower-amplitude variability. Given the results here and in Rajput et al. (2020), it is therefore possible that the variability for some of these objects is instead driven by a variability in the injection function and in turn by changes in the particle energy distribution.

One physical scenario in which the above situation might arise involves a variability that is mostly caused by internal shocks moving along the jet. In this "shock-in-jet" model (Marscher & Gear 1985; Spada et al. 2001), the injected energy is transmitted at irregular intervals to accelerate the shells of plasma in the jet. Energetic shocks in the jet then emerge via collisions between these shells, and some of the energy of the shocks is eventually converted into the radiative energy output of the relativistic particles, resulting in both a variable particle energy distribution and variable emission. Our results suggest that this may be a significant contributor to the variability not just in BL Lacs (where it is expected that the variability involves a balance between the acceleration and synchrotron/SSC cooling timescales of the relativistic electrons in the jet), but also in FSRQs.

3.4.2 Relationships between F_{var} and important blazar parameters

Several groundbreaking studies have shown that the fractional variability of AGN is anti-correlated with the sources' luminosity and black hole mass (Barr & Mushotzky 1986; Green et al. 1993; Papadakis & McHardy 1995; Lu & Yu 2001; Uttley et al. 2002; Papadakis 2004; Zhou et al. 2010; Kelly et al. 2011, 2013; Ponti et al. 2012). These results have usually been interpreted in the context of accretion timescales and are thus also linked to additional correlations between e.g. the break frequency in the power spectral density (PSD) of these sources and the black hole mass and accretion rate (Markowitz et al. 2003; McHardy et al. 2006; Körding et al. 2007; Kelly et al. 2011); the break frequency ν_{b} in particular has come to be recognized as a vital quantity to describe accretion processes and specific timescales of accretion. However, these studies analyzed the variability usually only in the 2-10 keV band, finding that ν_{b} occurred on relatively short timescales.

Shimizu & Mushotzky (2013) performed one of the first PSD analyses with BAT data using the 58-month catalog for 30 AGN. Due to the long timescales probed, they could not detect breaks in the power spectra, with the ensuing implication being that there was a lack of correlation between the variability and the luminosity and black hole mass. Soldi et al. (2014) similarly ascribe the same lack of correlation in their analysis to the fact that, for the vast majority of the sources in the catalog, the BAT can only constrain the variability on monthly timescales, which is much longer than the typical PSD break times that usually dictate some of these correlations in AGN.

In this study, we do not find significant correlations between the fractional variability of blazars on monthly timescales and their luminosity and black hole mass. Since we probe the same long timescales as in the two aforementioned studies, it is possible that our results arise for similar reasons. However, one major difference is that we focus on blazars, whereas the previous studies are exclusive to Seyferts. Even though, for some blazars, a correlation between variability and black hole mass could have led to a superficial probing of the disk-jet connection, in general, the blazars in our sample have very different underlying astrophysical processes associated with their X-ray emission (jetted emission) compared to Seyferts (emission from the disk and corona). Therefore, it is unclear whether this comparison with past studies is 100% valid to begin with.

While we also do not find a correlation between F_{var} and the Doppler factor δ, we do observe that the FSRQs have a higher mean δ than BL Lacs. This might be expected of the more luminous FSRQs, whose luminosities are at times several orders of magnitude higher than those of BL Lacs, but whose black hole masses are on average only a few times higher than those of BL Lacs (see Figure 3.3), implying that FSRQs need higher Doppler factors to reach such luminosities and that relativistic beaming may be contributing significantly to the X-ray variability in these sources.

The lack of correlation between F_{var} and the photon index Γ is somewhat unexpected, since the steeper indices associated with a significantly falling spectrum are likely indicative of radiative losses. Since for higher-energy particles, the cooling timescales are shorter ($t_{\mathrm{cool}} \propto \gamma^{-1}$), this would translate to higher and more rapid variability. In a study with *NuSTAR* data, Bhatta et al. (2018) do find a positive correlation between the hard X-ray variability and photon index (for both FSRQs and BL Lacs separately) for several observations of a sample of 13 blazars. They find that for BL Lacs, the trend is not as distinct as is found for FSRQs; they attribute this to rapid synchrotron cooling in BL Lacs at higher energies possibly contributing to photons at the high-energy end of each individual spectrum, resulting in a harder power law distribution and thus reducing the relationship seen of a higher variability with steeper index. This study, however, is performed on the shorter timescales probed by *NuSTAR*, and they note that their sample size is limited. The fact that we do not see any correlation in our study therefore suggests that cooling processes are not necessarily at the heart of the variability on longer timescales.

3.4.3 Interpreting the spectral variability

We detect statistically significant variability in 5 of our sources. For 3 of these, we find that the spectrum can be described with a simple power law that changes spectral slope on monthly timescales. This is generally in line with studies that show that the X-ray spectra (and in particular, the hard X-ray spectra) of blazars can be described with a power law. However, there are hints in our analysis pointing to potentially more complex spectra. For example, for 3C 454.3 and 1ES 0033+595, only two hardness ratios, $\frac{M}{L}$ and $\frac{H}{L}$, show statistically significant variability. This suggests that for these sources, the hard X-ray spectra may require a broken power law model to adequately describe their variability, with spectral variations possibly arising from the BAT spectra pivoting about a break energy at $\sim$25-30 keV. Such a break in the spectra could be present due to the BAT data lying between the synchrotron and Compton humps, as usually the hard X-ray data on either hump have significantly different spectral slopes (lower Γ for inverse Compton hump, higher Γ for synchrotron hump); alternatively, curvature could be detected if the data lie on the very peak of either hump. We inspect the latest SEDs provided for these sources in Paliya et al. (2019b), but find that all of the BAT data for 1ES 0033+595 are on the tail of the synchrotron hump, while all of the BAT data for 3C 454.3 are on the rising part of the Compton hump. However, given the significant variability we detect, it is possible that the SEDs shown in Paliya et al. (2019b), and therefore the location of the X-rays in the SEDs, experience significant changes over long timescales. In an analysis of the long-term variability of 1ES 0033+595, Kapanadze & Gurchumelia (2022) do in fact find significant curvature in most of the source's *Swift*-XRT spectra in the 0.3-10 keV band, stating that their best-fit model is a log-parabolic power law. Therefore, it is possible that our results are consistent with their analysis in that 1ES 0033+595 may require a more complex model than a simple power law.

The discussion of spectra more complex than a power law naturally brings up one of the most famous and well-studied sources in our sample. 3C 273 happens to be a blazar-like AGN (usually classified as an FSRQ within the context of blazars) with a fairly high viewing angle of $\sim 10^{\circ}$ (Stawarz 2004). While our analysis suggests that its emission can be described by a simple hard power law, several studies have indicated that its X-ray spectrum can be modeled by the combination of a Seyfert-like component (e.g. coronal emission and X-ray reflection features) and a beamed, blazar-like component to describe emission from the jet (Kataoka et al. 2002; Soldi et al. 2008; Esposito et al. 2015; Madsen et al. 2015). In particular, the analysis in Madsen et al. (2015) with *NuSTAR* and *INTEGRAL* data suggests that the hard X-ray spectral variability is caused by a change in amplitude in each component as their respective power law slopes remain fairly invariant. In an attempt to find some agreement through the BAT data, we briefly investigate this by performing simulations for such a scenario, but find that the quality of the BAT data is not high enough to detect the spectral features associated with the 2-component model, and that the hardness ratio values spanned by the data in the HR plane are best represented by the simulated HR points that result from the simple power law simulations. We therefore come to the conclusion that the higher sensitivity of *NuSTAR* is probably more appropriate to explore a more complex scenario like a 2-component model.

Finally, we find that Mrk 501 shows signs of "harder-when-brighter" behavior on monthly timescales, suggesting that the hard X-ray spectrum flattens as the source reaches brighter states. Bhatta et al. (2018) also find such a correlation for Mrk 501 with their *NuSTAR* analysis on shorter timescales. A reason for this could be that the brightening of the source corresponds to increased particle injection. As a HSP BL Lac, the BAT data for Mrk 501 lie at the tail of the synchrotron hump; this could cause the particle distribution to harden, resulting in a harder power law slope for the emitted spectrum. Alternatively, a strengthening of the magnetic fields in the jets could also lead to increased synchrotron emission, possibly producing harder photons in the process.

3.5 Conclusions

We have presented long-timescale, time-domain variability analyses of 127 blazars from the *Swift*-BAT 157-month catalog by use of $\sim$13 years of continuous archival hard X-ray data in the 14-195 keV band. Our main results are as follows:

1. We do not detect statistically significant flux variability for a significant fraction ($\sim$37%) of the blazars in our sample, which is in tension with the expected highly variable emission of blazars on most timescales and wavelengths.

2. On average, for the objects that do show variability, we find that FSRQs appear to have a very similar degree of flux variability compared to BL Lacs ($\langle F_{\rm var}\rangle = 76 \pm 5\%$ vs $\langle F_{\rm var}\rangle = 75 \pm 4\%$), possibly due to the variability in FSRQs being driven by variations in the particle injection as opposed to variations in external radiation fields.

3. We do not find correlations between $F_{\rm var}$ and the luminosity and black hole mass, possibly due to the fact that the BAT probes timescales much longer than the timescales where these

correlations have previously been observed; however, the physical mechanisms producing the X-rays in these blazars are also significantly different to those in the Seyferts analyzed in these previous studies. We also do not find a trend between $F_{\rm var}$ and the photon index Γ, suggesting that radiative losses may not be the main source of variability for these objects on long timescales.

4. We detect spectral variability in 5 blazars, and for 3 of them the behavior can be summarized as a simple power law in the hard X-rays that changes spectral slope Γ on monthly timescales. For at least two sources, it is possible that a more complex model is required to describe the variable spectra.

5. For Mrk 501, a HSP BL Lac, we detect a "harder-when-brighter" behavior at a significance of $>99.98\%$, possibly associated with increased particle injection or an enhancement of the magnetic fields in the jet.

Chapter 4: Investigating the variability of *Swift*-BAT blazars with *NICER*

In this chapter, we present results of X-ray spectral and time-domain variability analyses of 4 faint, "quiescent" blazars from the *Swift*-BAT 105-month catalog. We use observations from a recent, 5-month long *NICER* campaign, as well as archival BAT data. Variations in the 0.3-2 keV flux are detected on minute, $\sim$weekly, and monthly timescales, but we find that the fractional variability $F_{\rm var}$ on these timescales is $<$25% and decreases on longer timescales, implying generally low-amplitude variability across all sources and showing very low variability on monthly timescales ($F_{\rm var} \lesssim 13\%$), which is at odds with previous studies that show that blazars are highly variable in the X-rays on a wide range of timescales. Moreover, we find that the flux variability on very short timescales appears to be characterized by long periods of relative quiescence accompanied by occasional short bursts, against the relatively time-stationary nature of the variability of most other AGN light curves. Our analysis also shows that the broadband X-ray spectra (0.3-195 keV) of our sources can be described with different power law models. As is the case with most blazars, we find that 2 sources (2MASS J09343014-1721215 and PKS 0312-770) are well-modeled with a simple power law, while the remaining two (1RXS J225146.9-320614 and PKS 2126-15) exhibit curvature in the form of a log-parabolic power law. We also find that, in addition to the continuum, PKS 2126-15 requires significant absorption at the soft X-rays ($\lesssim$1 keV) to fully describe the observed curvature, possibly due to absorption from the intergalactic medium.

4.1 Introduction

Blazars are a class of radio-loud (RL) active galactic nuclei (AGN) whose defining characteristic is a jet aligned close to the observer's line of sight (Urry & Padovani 1995). Due to the bulk relativistic motion of the particles in the jet, any emission from the latter will be relativistically beamed in the direction of motion, and an observer at rest will detect emission that is much more powerful than if the particles were at rest. As a result, the emitted radiation from blazars, which is dominated by extreme non-thermal processes that take place in the jet, has historically been known to be very luminous, with high-amplitude, rapid variations in flux, spectra, and polarization observed across most timescales and energy bands (see e.g. Stein et al., 1976; Blandford & Rees, 1978; Angel & Stockman, 1980; Marscher & Gear, 1985; Morini et al., 1986; Feigelson et al., 1986; Wagner & Witzel, 1995; Ulrich et al., 1997; Andruchow et al., 2005; Lichti et al., 2008; Soldi et al., 2014).

While most blazars share a number of characteristics, such as flat radio spectra, rapid variations in flux and in radio/optical polarization, and superluminal motion at radio wavelengths (Mutel et al., 1990; Vermeulen & Cohen, 1994; Jorstad et al., 2005), they can nonetheless be separated into two subclasses: BL Lacertae (BL Lac) objects and flat-spectrum radio quasars (FSRQs). This classification is usually based on the rest-frame equivalent width (EW) of the optical emission lines, with FSRQs showing broad lines with EW>5Å and BL Lacs showing weak or no emission lines in their spectra (Stickel et al., 1991).

FSRQs and BL Lacs can further be told apart by their broadband spectral energy distributions (SEDs). The SEDs of BL Lacs are characterized by two broad emission humps that are usually close to equally luminous. The peak at low frequencies is likely caused by synchrotron emission processes that usually emit from the infrared to the X-rays, while the peak at high frequencies (X-rays to γ-rays) likely arises from the synchrotron self-Compton (SSC) mechanism, an inverse Compton process by the same highly energetic particles in the jet. FSRQs show the same two aforementioned emission humps, but in these blazars, the Compton hump is more luminous than the synchrotron hump; this is likely due to the radiatively efficient accretion in the more luminous FSRQs, which leads to a UV-bright disk that produces ionizing photons to form a broad-line region (BLR). The BLR, in turn, provides an additional source of photons external to the jet that undergo inverse Compton scattering (Ghisellini et al., 2009b, 2011), producing the high-energy hump in the SEDs of FSRQs.

In particular, the X-ray spectra of blazars can generally be well-described by a simple power law or a curved continuum that represent the non-thermal processes occurring in the jet (see e.g. Comastri et al., 1997). Many spectra show curvature in the form of either a log-parabolic power law or a broken power law (e.g. Massaro et al., 2004, 2006; Paggi et al., 2009; Furniss et al., 2013; Arcodia et al., 2018; Dalton et al., 2021), with many blazar emission models predicting that spectra exhibiting either shape can result from a relativistic particle distribution that has a similar curvature (see e.g. Sikora et al. 1994, 1997, 2009; Tavecchio et al. 2007; Tavecchio & Ghisellini 2008; Ghisellini & Tavecchio 2009, 2015; Arcodia et al. 2018, and references therein). Alternatively, curvature might be observed simply due to the location of the X-rays on the SED, as is the case with "extreme" blazars that have the peak of their synchrotron hump located at very high frequencies ($\nu_{syn}^{peak} \gtrsim 10^{17}$ Hz; see e.g. Paliya et al. 2019b for examples), likely due to the efficient acceleration mechanisms in their jets (e.g. Costamante et al., 2001; Foffano et al., 2019;

Paliya et al., 2019c).

An intrinsic curved continuum does not always yield a complete picture of the X-ray emission from a blazar. Certain studies have shown that sometimes, significant photoelectric absorption, in addition to said continuum, is required in the soft X-rays to fully describe the curved X-ray spectrum (e.g. Cappi et al., 1997; Tavecchio et al., 2000; Fabian et al., 2001a,b; Worsley et al., 2004a,b, 2006; Page et al., 2005; Grupe et al., 2004, 2006; Sambruna et al., 2007; Eitan & Behar, 2013; Arcodia et al., 2018; Dalton et al., 2021). At first glance, this contradicts the very nature of blazars, since in general these objects are considered to have negligible X-ray absorption along the line of sight, due to their kiloparsec-scale jet likely sweeping away any potential contribution to absorption from the host galaxy. In order to reconcile this, several studies (e.g. Fabian et al., 2001a; Behar et al., 2011; Campana et al., 2012, 2015; Starling et al., 2013; Eitan & Behar, 2013; Arcodia et al., 2018; Dalton et al., 2021) have suggested that the absorption might be due to the highly ionized "warm-hot" intergalactic medium (WHIM), with more recent studies emphasizing that such a component from the intergalactic medium should be considered in the spectral analysis of blazars when appropriate (see e.g. Arcodia et al., 2018; Dalton et al., 2021).

In a time-domain variability analysis of 127 blazars in the *Swift*-Burst Alert Telescope (BAT) 157-month catalog (Mundo & Mushotzky in preparation, see Chapter 3), we find that a non-negligible fraction ($\sim$37%) of the sample does not show statistically significant variability on monthly timescales in the 14-195 keV band, in tension with previous works that have established that blazars are extremely variable objects at almost every timescale and wavelength. However, it is unclear from just the BAT data if this apparent lack of variability is a result of truly relatively constant emission (i.e. only moderate amplitude variability) or emission that is mostly constant with occasional flaring events, as seen in Fermi data for some sources (e.g. Paliya et al., 2015;

Hayashida et al., 2015), or if it is solely related to the sensitivity or systematic issues of the BAT data. The BAT catalog data are unique in providing continuous observations over a 9-year timescale for a hard X-ray selected sample and thus sample the time variability of these objects in a previously unexamined time domain. Therefore, confirmation of these results could change our understanding of the properties of blazars and beamed AGN.

Because of the BAT's relatively low sensitivity per unit time (Tueller et al., 2008), it can only constrain the variability on monthly timescales for the vast majority of objects detected in the 105-month catalog. In order to determine if the supposedly "non-varying" sources exhibit variability on shorter timescales not detected by the BAT, we started a $\sim$5-month long campaign in 2021 with the Neutron Star Interior Composition Explorer (*NICER*) for each of 4 such apparently non-variable sources. Thanks to the *NICER* telescope's $>$100 times sensitivity per unit time compared to the BAT, the campaign allows for an estimate of the variability on a wide range of timescales, probing shorter timescales while also representing the timescales of the BAT catalog.

The 4 sources analyzed here with new *NICER* data (2MASS J09343014-1721215; PKS 0312-770; 1RXS J225146.9-320614; PKS 2126-15) correspond to the brightest blazars from the *Swift*-BAT 105-month catalog for which there was very little variability ($F_{\rm var} \lesssim 10\%$) on monthly timescales. In general, these objects lie at the low flux end of the BAT blazar population and are among the most quiescent sources in the catalog. In addition, according to a recent spectroscopic study of the blazars in the 105-month catalog (Paliya et al., 2019b), the *NICER* band (0.3-10 keV) falls on the same hump as the BAT band (14-195 keV) for each of the 4 sources, meaning that the broadband X-rays are likely produced by the same underlying process for each source, and thus the new *NICER* observations would shed light on the physical processes driving the BAT band.

In this chapter, our main objectives are to determine whether these 4 sources are variable, as well as to characterize the nature of their variability and their spectra in the *NICER* band. We describe the observations and data reduction in Section 2, present our variability and spectral analyses and their results in Section 3, and discuss these results in Section 4.

4.2 Observations and Data Reduction

4.2.1 *NICER*

Each of the 4 sources in this investigation were observed over a period of 5 months in order to mimic the long timescales of the BAT 105-month catalog, with $\sim$8 observations per month that had varying individual exposure ($\sim$40 observations total per source, PI: Mundo; see Table 4.1 and caption). Each source was observed for a total exposure of at least $\sim$20 ks taken over this 5-month period (all the data are available on the electronic version and the HEASARC archive[1]). The *NICER* data were reduced using HEASOFT v.6.29.1 and the current calibration files available (v. xti20210707). The `nicerl2` pipeline was used with the default settings using all 56 detectors and applying the necessary filters and calibration to produce cleaned events files.

We used the tool `xselect` to extract 1-second binned light curves, which we later re-binned to three different timescales for our time-domain variability analysis (see Figure 4.2 for an example of the campaign with light curves on minute and $\sim$weekly timescales for one of our sources). The background estimation and calculation of the total spectra were performed using the tool `nibackgen3C50`[2] (Remillard et al., 2022). The spectra were binned to a minimum of 20 counts per bin using the `grppha` tool.

[1]https://heasarc.gsfc.nasa.gov/cgi-bin/W3Browse/w3browse.pl
[2]https://heasarc.gsfc.nasa.gov/docs/nicer/tools/nicer_bkg_ est_tools.html

Table 4.1: *NICER* observations and sources used in our analysis. Shown are the source name, blazar type, redshift, observation ID, observation start dates, and the exposure times. *1RXS J225146.9-320614*: 38 observations with exposures between $\sim$200s and $\sim$2 ks; *2MASS J09343014-1721215*: 49 observations with exposures between $\sim$200s and $\sim$3 ks; *PKS 2126-15*: 41 observations with exposures between $\sim$150s and $\sim$4 ks; *PKS 0312-770*: 35 observations with exposures between $\sim$100s and $\sim$2 ks. For all sources, observations are spaced across 5 months. The wide range of exposures in the observations is the result of flagging periods of high background according to the `nicerl2` pipeline criteria. The full list of observations can be found in the electronic version and in the HEASARC archive.

Source name	Blazar Type	z	Obs. ID	Start Date	Exposure (s)
1RXS J225146.9-320614	BL Lac	0.2460	4638020101	2021/06/20	663
			4638020201	2021/06/23	1247
			4638020301	2021/06/27	1268
			4638020401	2021/06/29	653
			...	...	...
2MASS J09343014-1721215	BL Lac	0.2499	4638030101	2021/03/03	582
			4638030201	2021/03/06	687
			4638030301	2021/03/10	1192
			4638030501	2021/03/17	675
			...	...	...
PKS 2126-15	FSRQ	3.2680	4638010201	2021/06/22	710
			4638010301	2021/06/26	1480
			4638010401	2021/06/29	4284
			4638010402	2021/06/30	3405
			...	...	...
PKS 0312-770	FSRQ	0.2230	4638040101	2021/04/10	404
			4638041301	2021/04/13	1234
			4638040301	2021/04/17	364
			4638040401	2021/04/20	89
			...	...	...

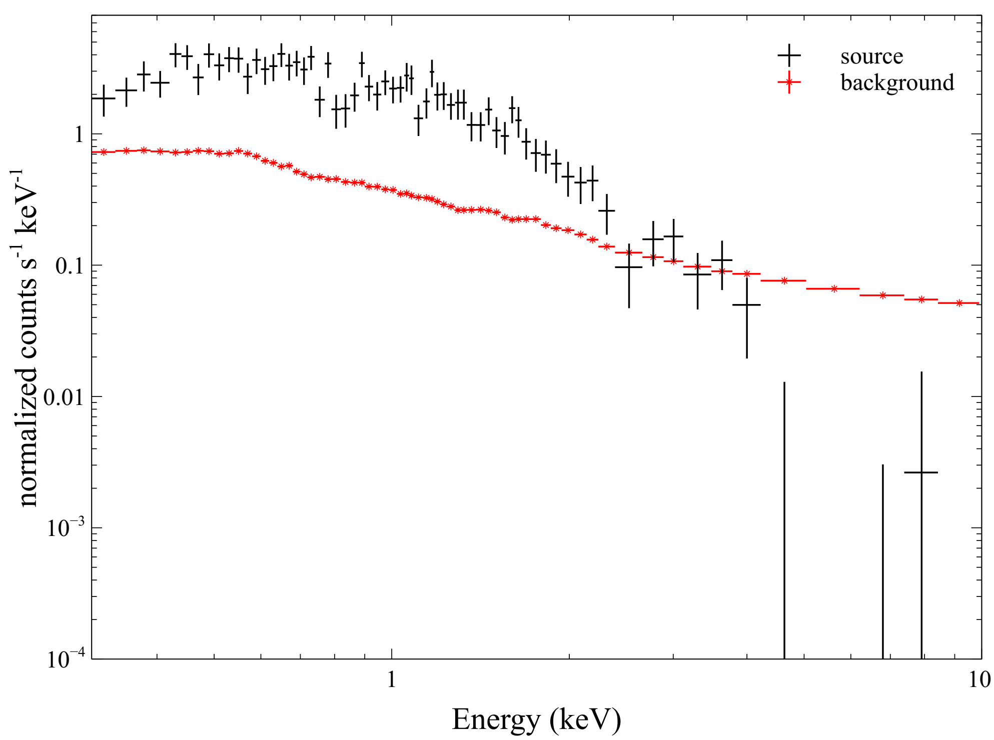

Figure 4.1: Sample spectrum of an individual observation of 2MASS J09343014-1721215 which took place during the second month of the campaign. The background begins to reach the level of the signal between 2-3 keV ($\sim$ 2keV). For consistency across all sources and observations, light curves are extracted in the 0.3-2 keV range for the flux variability analysis.

4.2.2 *Swift*-BAT

To probe the hard X-rays and complete the broadband X-ray spectrum, we make use of the archival observations available in the *Swift*-BAT 105-month catalog[3] from the BAT Hard X-ray Survey (Oh et al., 2018). We include the ready-to-use, eight-channel time-averaged spectra that are provided there in this analysis.

4.3 Results

4.3.1 Time-domain flux variability analysis in the *NICER* band

We begin by performing a time-domain analysis of the flux variability for each source on minute, $\sim$weekly, and monthly timescales, which cover the range of timescales represented by both *NICER* and the BAT. Since *NICER* is not an imaging instrument, we need to rely on the spectrum and the estimated background from each observation to determine which band to extract the light curves from. We find that across all observations, the ratio of the signal to the background reaches $\sim$1 at the very least at $\sim$2 keV (see Figure 4.1 for an example), with some observations showing the background reaching the signal above that energy. In order to have a consistent comparison across all observations and sources, we therefore decide to extract light curves in the 0.3-2 keV range for each source (see e.g. Figure 4.2) and perform our flux variability analysis in this range. (We show the light curves to the additional 3 sources in Figures 1d-1i in the electronic version of Mundo & Mushotzky 2023.)

In order to determine whether we detect variability in our sources, we fit the light curves

[3] https://swift.gsfc.nasa.gov/results/bs105mon/

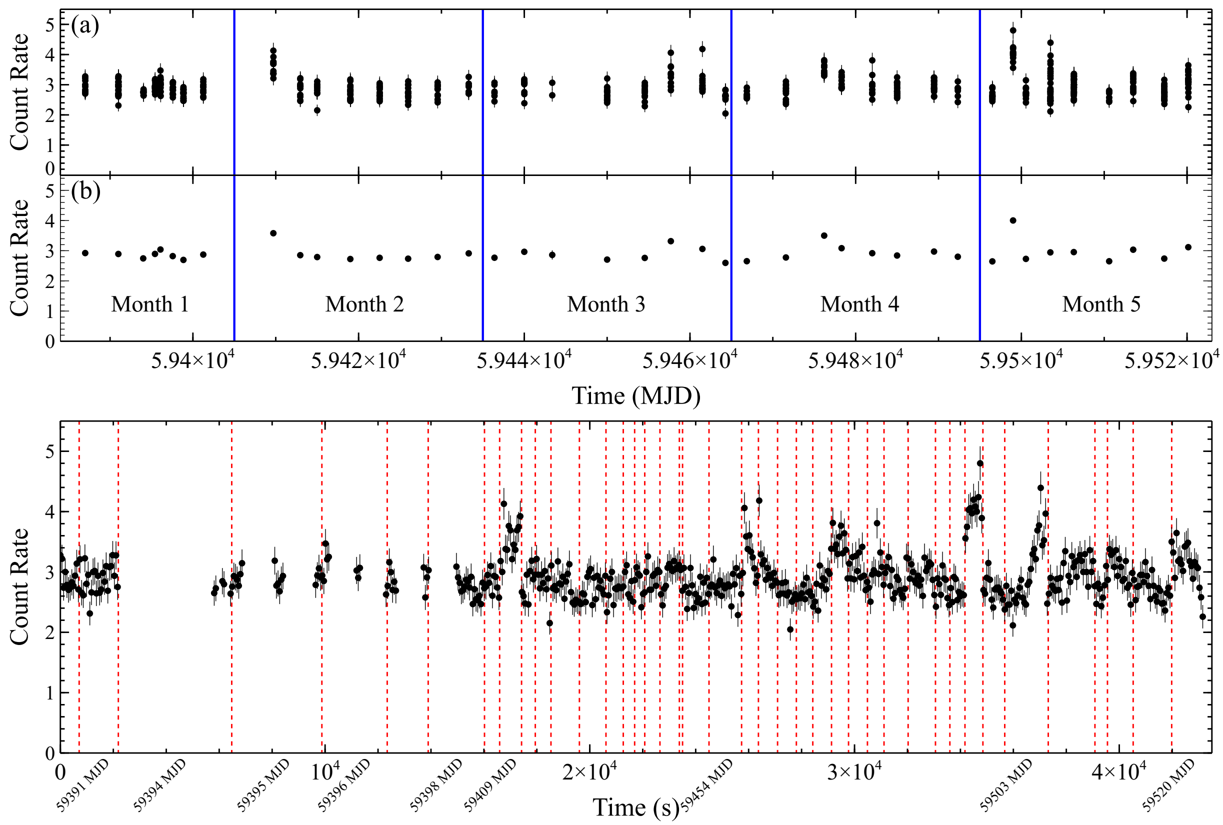

Figure 4.2: *Top panel*: Sample light curve for one of our sources, PKS 2126-15, in two timescales probed in this study: (a) binned to one minute, and (b) binned ∼weekly (by observation). Count rates are in the 0.3-2 keV band. Blue lines are shown to depict the observational campaign structure. *Bottom panel*: The same as top panel (a), but this time plotted over the total exposure time for the source in seconds, as opposed to over the total campaign time, in order to highlight the short timescale variability. Red dashed lines indicate a change from one observation to the next. To connect the bottom panel to top panel (a), the rate at an effective time of e.g.$\sim 1.7\times10^4$ sec in the bottom panel is seen in Month 2 of top panel (a) at 59409.7 MJD. We also include labels on the bottom panel to show when certain observations occur in MJD. As with top panel (a), the data points are ∼60 s wide. *(Similar light curves for the other blazars are shown in Figures 1d-1i in the electronic version of Mundo & Mushotzky 2023.)*

at each timescale with a constant function, and then apply a χ^2 test. We define a significant detection of the variability as occurring whenever $p_{\chi^2} \leq 5\%$, where p_{χ^2} is the null-hypothesis probability of obtaining that value of χ^2 if the source were in fact constant. Furthermore, we quantify the flux variability of our sources by using the methodology described in e.g. Vaughan et al. (2003), which accounts for the contribution of an additional variance from measurement uncertainties. The "excess variance" has been used over the past few decades to estimate the intrinsic source variance (e.g. Nandra et al., 1997; Edelson et al., 2002), and can be normalized to directly compare the variance between different sources. The fractional root mean square (rms) variability amplitude F_{var} is defined as

$$F_{\text{var}} = \sqrt{\frac{S^2 - \overline{\sigma_{\text{err}}^2}}{\overline{x}^2}}, \tag{4.1}$$

i.e. the square root of the normalized excess variance, and is the quantity we will use here.

Thanks to the high sensitivity of *NICER*, we are in fact able to detect and quantify statistically significant variations on each of the 3 timescales we have chosen in the 0.3-2 keV band. However, we find that F_{var} is at most 25% across all sources at all 3 timescales, and appears to decrease on longer timescales, implying low-amplitude variability overall and showing little variability on monthly timescales (highest F_{var} on monthly timescales is $12.9 \pm 0.4\%$ across all sources, see Figure 4.3), with 2 out of 4 sources showing $F_{\text{var}} < 5\%$ on monthly timescales, which is unusual and unexpected for the X-ray emission from blazars. It is possible that this, to a certain extent, may be confirming what we have observed with the lack of variability in the BAT data for these sources. While we detect statistically significant variability, this low-amplitude variability would be deeply at odds with the past general literature that shows that blazars are

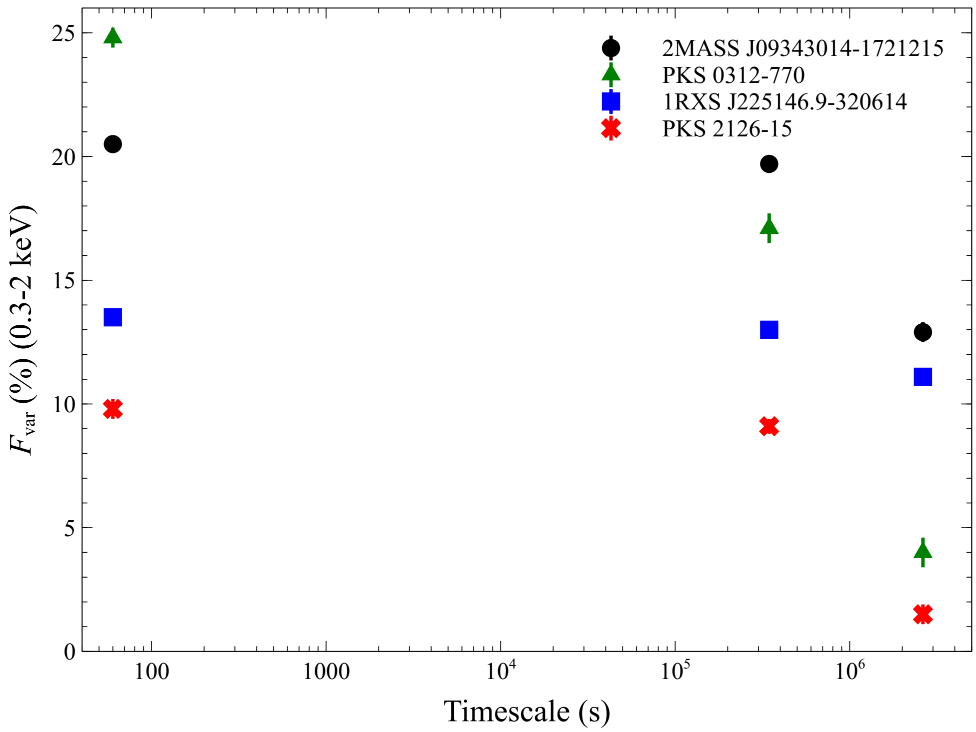

Figure 4.3: Fractional variability as a function of timescale. For each source, the variability amplitude decreases with increasing timescale, a trend that is not expected of blazars and other AGN.

extremely variable objects in the X-rays. Furthermore, the behavior of the fractional variability as a function of timescale is peculiar, since for other AGN such as Seyferts, the opposite trend of variability increasing with timescale is observed (e.g. Edelson & Nandra, 1999; Uttley et al., 2002; Markowitz et al., 2003; McHardy et al., 2004; Uttley & McHardy, 2005).

While on average, the amplitude of the variability in our sources is quite low, we do find that the minute-timescale light curves exhibit occasional short bursts/flare-like events, along with periods of quiescence that last on the order of several weeks (see e.g. Figure 4.2, top panel (a) and bottom panel). This combination of long, low-amplitude components and short, flaring components suggests that the nature of the variability on very short timescales may be non-stationary, as opposed to the expected stationary or "weakly" stationary variability from most other accreting objects (see e.g. Vaughan et al., 2003; Uttley et al., 2005).

4.3.2 Spectral analysis

We fit the *NICER* spectra for each source using XSPEC v12.12.0g (Arnaud 1996). Following our search for variability in the flux, we begin by searching for any signs of spectral variability from observation to observation, i.e. on ∼weekly timescales. In order to do this, we fit the individual observations of each source with a simple power law, using the `tbabs` model (Wilms et al., 2000) and cross-sections from Verner et al. (1996) to model the Galactic absorption (i.e. `tbabs*po`), setting $N_{\rm H,Gal}$ to the appropriate values from the HI4PI survey for each source (HI4PI Collaboration et al., 2016).

The energy range of the spectra used for each source in this step varies slightly, and depends on where the background starts to dominate the signal; as previously mentioned, the lowest energy where this happens, across all sources, is ∼2 keV, due to the generally higher background in these cases. However, some of the brighter sources, such as 1RXS J225146.9-320614 (∼8 counts s^{-1} in the 0.3-2 keV band), have some observations that have good-quality data out to ∼7 keV, so we expand the range used in fitting the individual spectra whenever appropriate, on a per source basis (the lowest energy used in all spectra is always 0.3 keV). We exclude any observations that have very low exposures (i.e. $\lesssim$ 200s) from the spectral variability analysis, so as to maximize the signal-to-noise and be able to constrain relevant parameters. For each of the individual observations, a simple power law modified by absorption (consistent with Galactic absorption for all but PKS 2126-15) is an acceptable fit to the data. We find that PKS 2126-15 requires absorption in excess of the Galactic absorption in order to adequately describe its individual spectra (e.g.

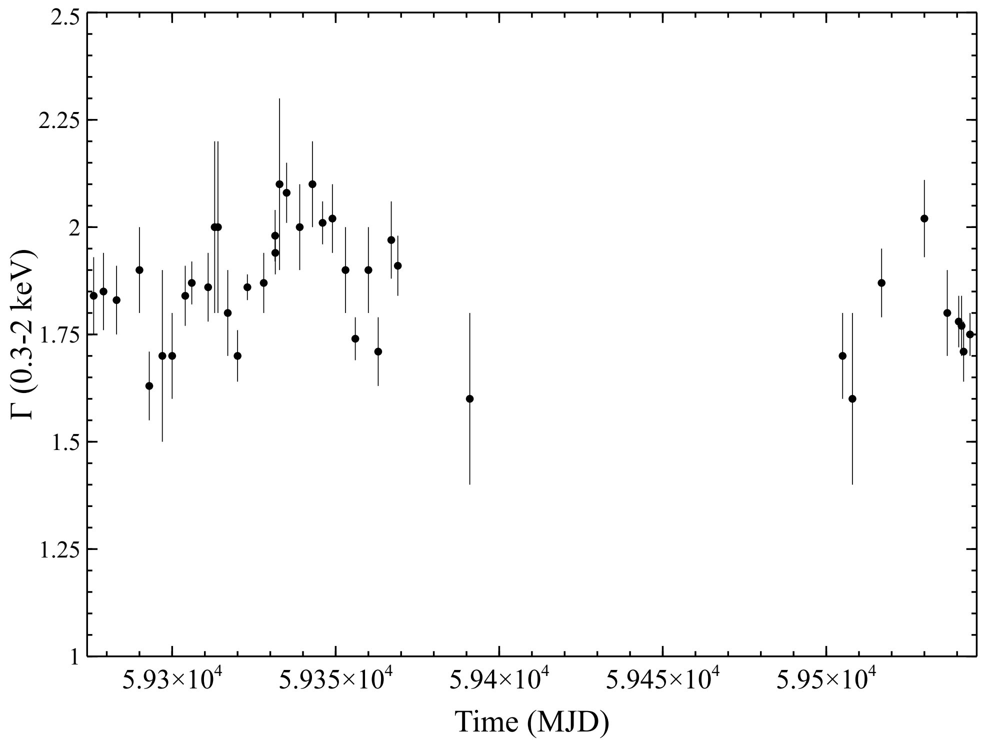

Figure 4.4: Photon index Γ in the 0.3-2 keV range for 2MASS J09343014-1721215, based on spectral fits to individual observations (the gap in the middle is likely due to observing constraints). Observations with very short exposures (i.e. $\lesssim$ 200s) were excluded. Γ varies by only 7% at the 1σ confidence level.

$\Delta\chi^2 = 132$ for one additional free parameter, for a relatively high exposure (~4 ks) observation). Therefore, for the purposes of the search for spectral variability, we include an intrinsic absorber and use the model `tbabs*ztbabs*po` for the individual observations of this source.

We find that overall, the photon index Γ of each source does not vary by more than ~15% at the 1σ confidence level (see Figure 4.4 for an example with 2MASS J09343014-1721215). While statistically significant ($p_{\chi^2} < 5\%$), these variations are much smaller than is usual for blazars, and are again at odds with the literature. However, they are at least consistent with the low flux variability we find, since variations in flux are usually linked to variations in the spectrum. Due to the low spectral variability, we decide to co-add the spectra of each source in order to maximize our signal-to-noise for a more detailed spectral analysis. We also include the

Source name	1RXS J225146.9-320614	2MASS J09343014-1721215	PKS 2126-15	PKS 0312-770
Model	`tbabs*zlogpar`	`tbabs*po`	`tbabs*ztbabs*zlogpar`	`tbabs*po`
$N_{\rm H,Gal}$ (10^{22} cm^{-2})*	0.0104	0.0645	0.0445	0.0783
$N_{\rm H,ex}$ 10^{22} (cm^{-2})	...	...	1.1±0.2	...
z*	0.2460	0.2499	3.2680	0.2230
Γ/α	1.84±0.01	1.81±0.02	1.0±0.1	2.15±0.03
β	0.29±0.03	...	0.16±0.06	...
$K_{\rm NICER}$ (10^{-3})	4.11±0.03	1.49±0.02	$5.7^{+0.7}_{-0.6}$	0.96±0.02
$K_{\rm BAT}$ (10^{-3})	13±3	1.4±0.4	$2.6^{+0.7}_{-0.6}$	4±1
χ^2/d.o.f.	407/422	349/364	645/598	241/236

Table 4.2: 90% confidence level parameters for the broadband X-ray data; all parameters other than the normalization were tied between the two instruments. K's are the normalizations of the respective instruments, and Γ/α are the photon index or the slope at the pivot energy (fixed at 1 keV) in the case of the log-parabola; β is the curvature parameter, with positive values indicating convex curvature. $N_{\rm H,Gal}$ and z were frozen to the corresponding values (parameters with asterisk).

non-contemporaneous, time-averaged 105-month BAT spectrum for each source to obtain a joint fit in the broadband X-rays.

We start by fitting the broadband spectra with a simple power law, as we did with the individual observations, and move towards progressively more complex models when appropriate. We let the normalization vary across the two instruments to allow for any potential long-term variability, and fit with the same values for the rest of the parameters. All spectra are plotted in the rest frame of the observer. We report our results for the individual sources in the following subsections.

4.3.2.1 PKS 0312-770 and 2MASS J09343014-1721215

For PKS 0312-770 and 2MASS J09343014-1721215, the signal of the co-added spectra dominated the background out to 3 keV and 5 keV, respectively, so we use the spectra up to those energies. We also exclude the last 3 channels of the BAT data for 2MASS J09343014-1721215 due to low signal-to-noise. The data for both of these sources are well-described by a simple power law with Galactic absorption (i.e. `tbabs*po`, see Figure 4.5 , top panel), with $\Gamma =$

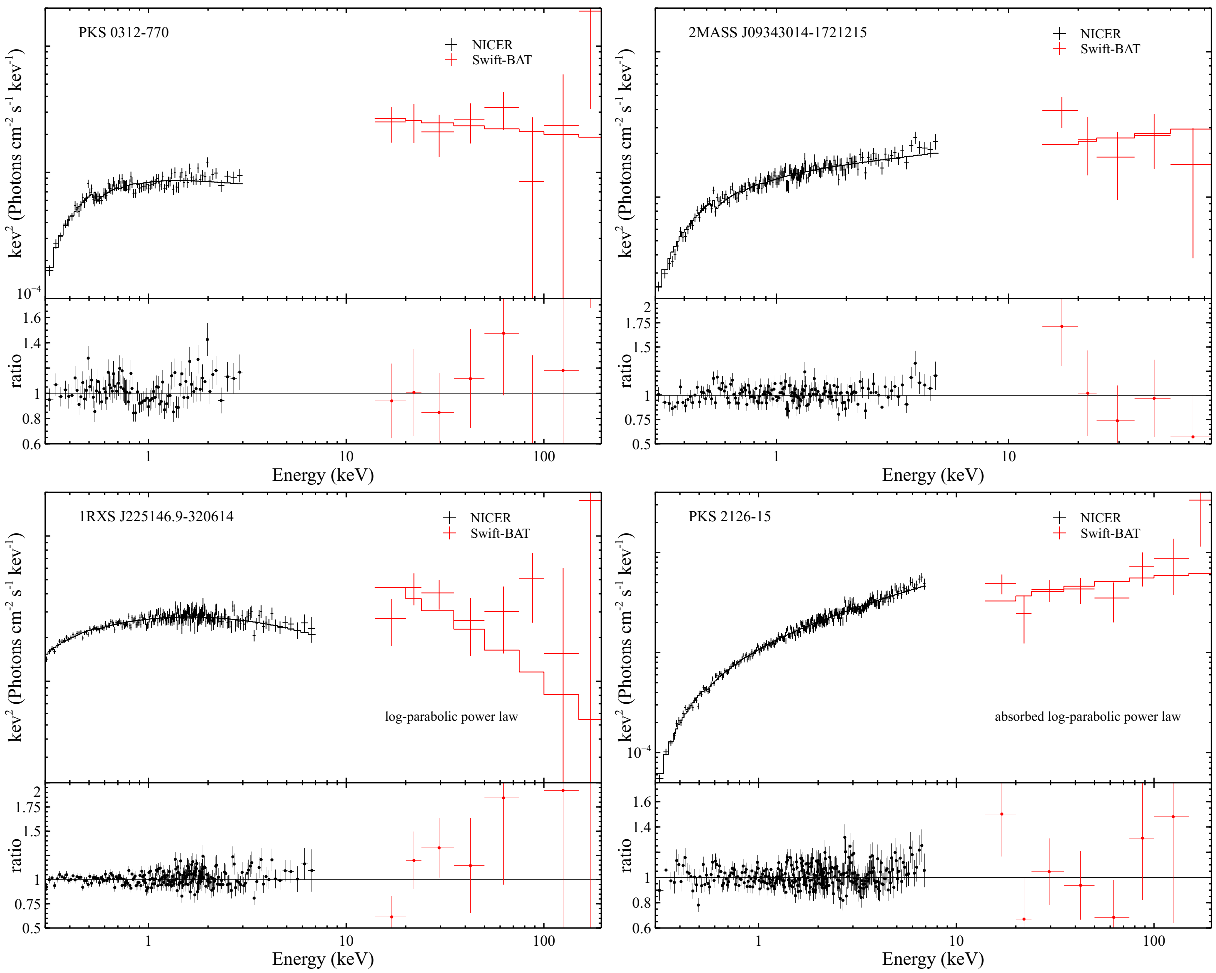

Figure 4.5: Unfolded spectra and best-fit models for the broadband X-rays in our sample. The top two panels are fits with a simple power law.

2.15 ± 0.03 for PKS 0312-770 (χ^2/d.o.f.=241/236) and $\Gamma = 1.81 \pm 0.02$ for 2MASS J09343014-1721215 (χ^2/d.o.f.=349/364). For PKS 0312-770, the normalization of the BAT data is $\sim$4 times larger than that for the *NICER* data, implying some variability on very long timescales. For 2MASS J09343014-1721215, the normalization across the two instruments is practically identical (see Table 4.2), confirming a lack of variability on long timescales.

According to Paliya et al. (2019b), the *NICER* spectrum of the BL Lac 2MASS J09343014-1721215 begins on the rising part of the synchrotron hump in the SED, and the broadband X-rays cover the very peak of the hump. In order to probe this curvature, we therefore also fit this source's spectrum with a log-parabolic power law, but we find that the curvature parameter is not well constrained and that the fit does not yield a statistically significant improvement over a simple power law.

4.3.2.2 1RXS J225146.9-320614

For this source, the signal of the co-added *NICER* spectrum dominates the background up to $\sim$7 keV, so we use the 0.3-7 keV spectrum. When fitting with a simple power law, we find that the residuals show significant curvature. We therefore proceed to fitting with a log-parabolic power law (`tbabs*zlogpar`). This model provides the best fit to the data, improving from the simple power law fit by $\Delta\chi^2 = 233$ for one additional free parameter, with a significance of $> 99.99\%$ evaluated using the F-test (see Figure 4.5, bottom left and Table for fit details), with χ^2/d.o.f.=407/422. We also find variability between the BAT and *NICER* spectra by a factor of $\sim$3 (see normalizations in Table). As with 2MASS J09343014-1721215, the broadband X-ray spectrum for this source also lies on the peak of the synchrotron hump (Paliya et al., 2019b), so we associate the observed curvature with synchrotron emission intrinsic to the source, which is expected of many BL Lac objects.

4.3.2.3 PKS 2126-15

As with 1RXS J225146.9-320614, for PKS 2126-15 the signal dominates the background up to 7 keV. Following our usual procedure, we initially fit the co-added spectrum of PKS 2126-15 with a simple power law and once again observe curvature in the residuals. We thus proceed to fit with a log-parabolic power law. This improves the fit by $\Delta\chi^2 = 642$ for 1 additional free parameter, at a significance of $>$99.99%. However, this is not enough to completely describe the observed curvature, and significant negative residuals remain at the soft X-rays (see Fig. 4.6). We find that an additional absorption component at the redshift of the source (`ztbabs`, assuming solar abundance), in excess of the Galactic absorption, improves the fit by $\Delta\chi^2 = 96$ for 1 additional free parameter, at a significance of $>$99.99%. This results in our best fit, with χ^2/d.o.f.=645/598 (Figure 4.5, bottom right). We are also able to fit the spectrum with a similarly absorbed broken power law, but find that it is not statistically distinct from the absorbed log-parabola. We therefore report the fit with a log-parabolic power law, as it requires fewer free parameters (see Table 4.2).

The absorption required for our best fit is significantly larger than the Galactic absorption, namely $N_{\mathrm{H,ex}} \sim 10^{22}$ cm^{-2} at the redshift of the source (see Table 4.2). This is unusual for blazars, as the jet is expected to remove any material from the host galaxy that may cause absorption along the line of sight. Going back to the individual observations, we find through a χ^2 test (using the same criteria as for the flux variability analysis in Sec. 3.1) that there is no significant

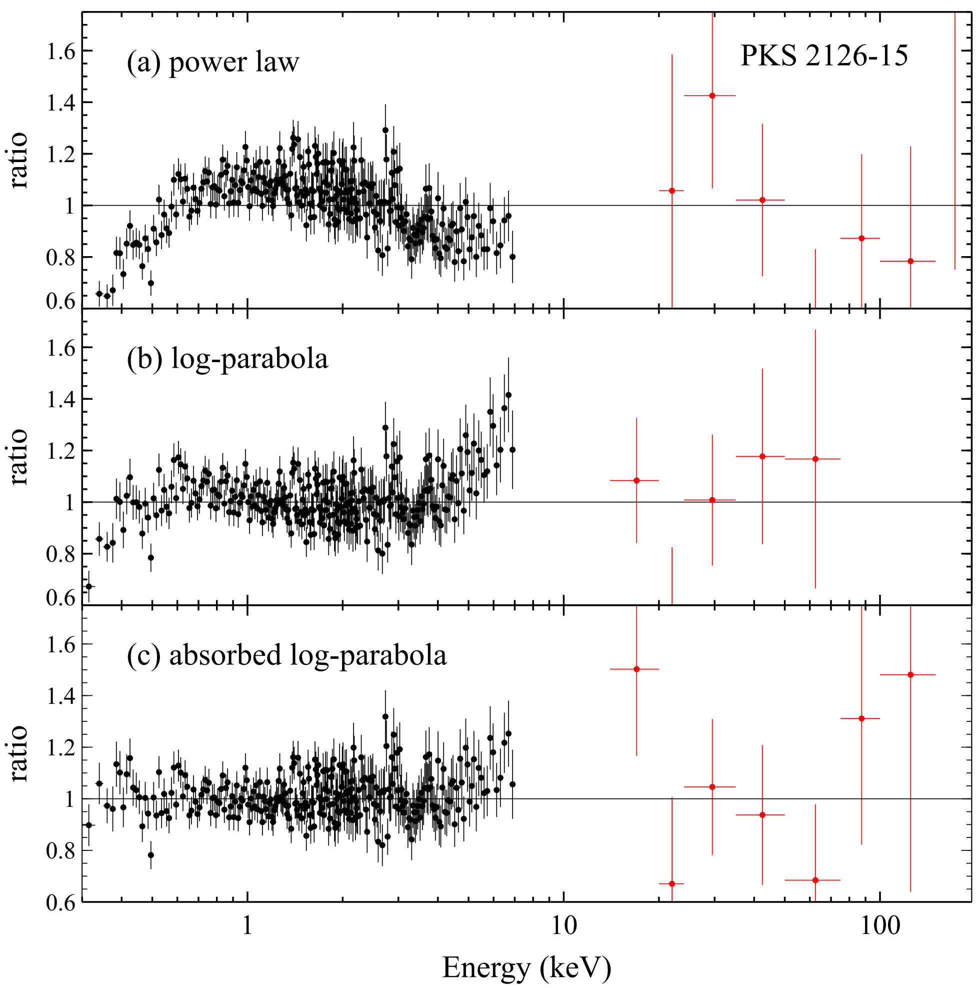

Figure 4.6: The ratio of *NICER* (black) and *Swift*-BAT (red) spectra for PKS 2126-15 to different models. (a) The ratio to a power law. (b) Ratio to a log-parabola. (c) Ratio to an absorbed log-parabola. The fit improves significantly with the latter (significance > 99.99%).

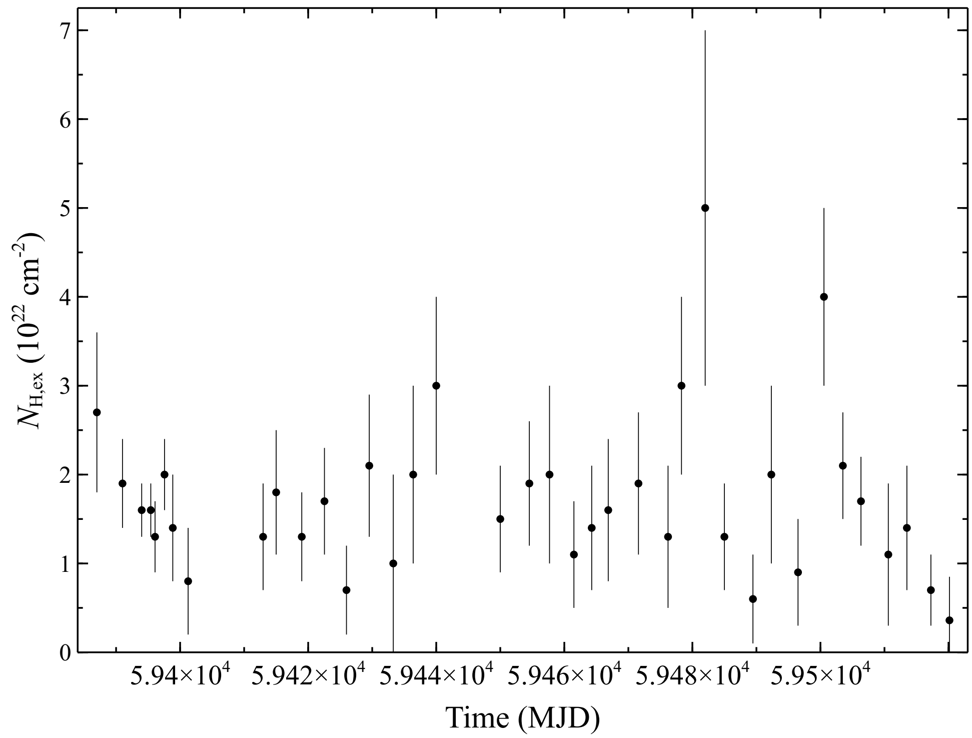

Figure 4.7: Time series for the column density required in excess of Galactic absorption for PKS 2126-15. A χ^2-test indicates there is no significant variability from observation to observation.

variability in the column density from observation to observation, with $p_{\chi^2} > 5\%$ (see Figure 4.7). This may hint at a possible absorption contribution from the intergalactic medium, as its column density should not change with time (see Sec. 4.2.1 for further discussion).

4.4 Discussion

4.4.1 Blazars not ablaze: Non-variable blazars in the broadband X-rays?

Previous studies have shown that the extreme variability often seen in the emission of blazars may be accompanied by periods of relative quiescence. For example, Paliya et al. (2015) and Hayashida et al. (2015) performed multi-wavelength studies of the well-studied FSRQ 3C 279, where they divided the γ-ray and X-ray light curves into flaring states and periods of low activity. Their data imply that at times, 3C 279 exhibits periods of relatively constant emission on timescales close to a year until the source undergoes a flare with extreme variability. Similarly, Chand & Gopal-Krishna (2022) use $\sim$3.5 years' worth of optical data from the Zwicky Transient Facility on 80 FSRQs to show that it is fairly common for transitions between active and quiescent states to occur on year-like timescales.

In another multi-wavelength study aimed at comparing the SED properties of a sample of 33 blazars, Williamson et al. (2014) divide over 4 years of data in the optical, X-rays, and γ-rays into quiescent and active states. Much like the aforementioned studies, their data also show flaring events that are followed by low-activity epochs that last close to a year. More specifically, they find that the sources in their sample of blazars are in a γ-ray quiescent state for a significant percentage of the time, with the sources spending $<$25% of the time in an active period, implying emission that is mostly quiescent with occasional flaring events. Studies such as Soldi et al. (2014) and Chand & Gopal-Krishna (2022) report blazars that seem to not exhibit much variability for even longer periods of time in the hard X-rays and the optical band, respectively, but they exclude these objects from their analysis, as they constitute only a small percentage of their sample. For the purposes of this study, it would be ideal to compare our results to sources with similar quiescent states/behavior in the X-rays. However, similar analyses of the X-ray data of blazars that do not show much variability have not been published (at times due to poor sampling in these states, see e.g. Rani et al. 2013; Hayashida et al. 2015; Rodrigues et al. 2021), with many blazar studies heavily biased towards bright targets and/or active states.

Given that our *NICER* data do not reach yearly timescales, it could very well be the case that the low-amplitude variability behavior observed in our sources is only one part of the bigger picture, and that we are observing our 4 sources in quiescent states. However, we also observe a strange trend of fractional variability amplitude decreasing with increasing timescale, which appears to be in tension with past studies that show that the stochastic variability of AGN, including blazars, is usually best described by a “red noise” power spectrum, implying that the amplitude of the variations should increase on longer timescales (see e.g. Edelson & Nandra 1999; Uttley et al. 2002; Markowitz et al. 2003; McHardy et al. 2004; Uttley & McHardy 2005 for Seyfert-like AGN, and Chatterjee et al. 2008, 2012; Abdo et al. 2010c; Goyal et al. 2022 for blazars). While the variability behavior of our sources seems to contradict these studies, we should stress that our data are likely too limited to constrain this type of behavior at this time. In the future, the acquisition of further data (see Section 4.4.1) may allow us to compare more directly with previous studies and determine whether the nature of the variability is in fact in tension with a “red noise” power spectrum.

The *NICER* data also show very low fractional variability amplitude on the same timescales as the data from the BAT catalog. As previously stated, for each of our sources, the 105-month BAT light curves show no statistically significant variability on monthly timescales, and, consistent with our fits to the broadband X-ray spectra, the *NICER* and BAT bands probably originate from the same physical processes (see Paliya et al., 2019b). This means that, under the assumption that the shape of the spectrum has not changed between the BAT and *NICER* observations, the *NICER* data could possibly serve as a proxy to the BAT data to infer that the broadband X-rays from these objects may not exhibit much variability for the duration of the BAT light curves, which would amount to almost a decade, much longer than the typical year-long duration of the quiescent periods previously cited.

As seen in Figure 4.5 and Table 4.2, for three of our sources, we do observe some variability between the *NICER* and BAT spectra. However, this does not necessarily contradict the trends of low variability that we have observed with the time-domain flux variability analysis. Our *NICER* data are from the last calendar year, and the 105-month BAT spectra are time-averaged over a period from 2004-2013; this means that, while we may observe some variability between the different bands, it would be on very long timescales. These timescales are again much longer than the yearly timescales related to the periods of quiescence that were previously discussed. Therefore, the possibility of blazars with much longer periods of quiescence still remains.

In an attempt to address the very low-amplitude variability we observe, we compare our variability timescales with the cooling timescales of the emitting electrons in the jets of our sources. As previously mentioned, for the BL Lacs in our sample, the X-rays are associated with synchrotron emission (Paliya et al., 2019b), with cooling time

$$t_{\rm syn} = \frac{3m_{\rm e}c}{4\sigma_{\rm T}U'_B\gamma'\Gamma} \sim \frac{7.7\times10^8}{B^2\gamma'}\ {\rm s} \tag{4.2}$$

in the observer's frame (e.g. Sari et al., 1996; Ghisellini, 2013), where Γ is the bulk Lorentz factor, U'_B the magnetic energy density in the co-moving frame, and γ' the Lorentz factor of the relativistic electrons in the frame of the jet. Using values of γ and the magnetic field strength B from the modeling in Paliya et al. (2019b), we find cooling times of $\sim$1 day for 2MASS J09343014-1721215 and 1RXS J225146.9-320614. For the FSRQs in our sample, the X-ray emission ($E_{\rm x}\sim 1$ keV) is caused by external Compton, with cooling time

$$t_{\rm EC} = \frac{3m_{\rm e}c}{4\sigma_{\rm T}u'}[E_0(1+z)/E_{\rm x}]^{1/2} \tag{4.3}$$

in the frame of the observer (see e.g. Saito et al., 2013; Paliya et al., 2015), where E_0 is the characteristic energy of the seed photons, and u' is the total seed photon energy density in the co-moving frame, assuming mostly inverse Compton scattering of BLR and dusty torus photons, and calculated as in e.g. Sikora et al. (2009). We find cooling timescales on the order of $\sim$1 week for PKS 0312-770 and PKS 2126-15.

In general, the cooling times we obtain are relatively short compared to the longest timescales we probe with the *NICER* and BAT data, and as we have shown, we do observe low-amplitude variability on timescales similar to some of the cooling times. Assuming a leptonic model, this could result from very short, shock-related acceleration timescales that would imply almost instantaneous acceleration, with the latter providing a near-constant source of high-energy electrons to the emitting region (see e.g. Tammi & Duffy, 2009). This "continuous" particle injection would then provide a very tight balance with the effects of energetic losses, resulting in an observed flux that is close to constant over time. Studies such as Tavecchio et al. (2009) have in fact suggested similar scenarios to explain the apparent long-timescale stability of the TeV flux in some "extreme" blazars. In these models, there must be very fine tuning between injection and loss processes to produce the observed roughly constant fluxes, a strong constraint on blazar models.

Of course, we also observe variability with slightly higher $F_{\rm var}$ on timescales of a minute. Upon close inspection of the short-timescale light curves, we find that this is likely due to the fact that the variability is characterized by longer periods of relative quiescence with occasional events that are flare-like in nature and which last several minutes. While many accreting objects are believed to show variability behavior that is near time-stationary (i.e., the statistical moments of the underlying process remain fairly constant over time), non-stationary time series involving flares and quiescent periods have been observed in the X-rays before (see e.g. Leighly & O'Brien, 1997; Alston et al., 2019), as well as in the aforementioned studies with Fermi-detected sources, although as previously noted, the studies on the Fermi sources correspond to baselines much longer than the one currently available for our data.

The very short-timescale variability addressed in this study occurs on timescales that are much shorter than the cooling timescales for our sources. This suggests that the variability on these timescales is likely due to other factors that are not related to energetic losses. Generally, blazar emission models assume a single quasi-spherical emission region, however it could be the case that the jets have many localized, X-ray emitting regions that contribute to this short-timescale variability, but whose effects on the emission are smoothed out when observed on longer timescales. Ghisellini et al. (2009a) proposed a multi-region scenario to explain fast, $\sim$minute timescale variability in 2 BL Lacs, with the variability potentially being caused by ultra-relativistic particles continuously flowing along magnetic field lines through magneto-centrifugal acceleration of the particle beams. They proposed this scenario in the context of ultra-fast flaring events, of which we do find some evidence in the data.

It is important to note that in general, it would be premature to draw strong conclusions from these results given our small sample size and the fact that the *NICER* data only go out to monthly timescales. To that end, we have a new follow-up, multi-cycle *NICER* campaign currently underway that increases the sample size by 50% and our temporal baseline by a factor of 3. This campaign will allow us to probe the variability of our sources up to timescales of a year, with the main objectives of characterizing the long-term variability, searching for potential yearly flares, and obtaining high-quality time-averaged spectra (Mundo et al. 2023, in preparation).

4.4.2 Interpreting the Broadband X-ray spectra

The X-ray spectra of blazars can usually be described by a simple power law or some form of curved continuum. Blazar emission models can in fact predict curvature in the emitted spectra that is linked to the shape of the emitting particle energy distribution (e.g. Tavecchio et al., 2007; Sikora et al., 2009; Ghisellini & Tavecchio, 2009, 2015). In other, more extreme cases, blazars may have their synchrotron peak located at frequencies $> 10^{17}$ Hz, implying that the curvature and the broadband X-rays are produced exclusively by synchrotron emission (e.g. Paliya et al., 2019b). Therefore, in many cases a curved spectrum is seen as a quality intrinsic to the physical processes that are at the root of blazar emission.

We observe these spectral characteristics with our sample, with two blazars exhibiting power-law behavior and the remaining two well-described by models that invoke curvature. In particular, 1RXS J225146.9-320614 requires a log-parabolic power law as the best fit for its broadband X-ray spectrum, and we attribute this curvature to synchrotron emission, as according to Paliya et al. (2019b) it is a high-frequency peaked blazar, with the broadband X-rays falling on the synchrotron peak. The latter is also true of 2MASS J09343014-1721215, but we find that a log-parabola does not significantly alter the fit, and that the low curvature parameter is not very well-constrained. Additional data from our previously mentioned follow-up campaign would increase the quality of the spectrum and may reveal the synchrotron peak more clearly.

PKS 2126-15 also shows curvature in the form of a log-parabolic continuum that is likely intrinsic. However, this source is an FSRQ, with the broadband X-rays lying on the rising part of the inverse Compton hump and likely produced by EC effects (Paliya et al., 2019b). Therefore, the observed curvature is likely more directly connected to the shape of the energy distribution of the electrons that are upscattering the external photon fields. However, in order to fully describe the curvature, our fit also requires significant absorption at the soft X-rays in excess of the Galactic absorption, which is unusual for a blazar.

4.4.2.1 The curious case of PKS 2126-15: An absorbed FSRQ?

Generally, blazars are not expected to show significant X-ray absorption in their spectra. This is because the kpc-scale jet points along our line of sight, and thus likely sweeps any potential X-ray absorption component from the host. In particular, FSRQs tend to be the most luminous, powerful blazars (e.g. Fossati et al., 1998; Ghisellini et al., 2017), and are therefore more effective in removing host absorbers in the vicinity, further decreasing the likelihood of any type of contribution from the host galaxy to their X-ray spectra.

Despite this, over the past two decades, several blazars have shown hardening at the soft X-rays that can in fact be modeled by absorption (e.g. Cappi et al., 1997; Tavecchio et al., 2000; Fabian et al., 2001a,b; Worsley et al., 2004a,b, 2006; Page et al., 2005; Grupe et al., 2004, 2006; Sambruna et al., 2007; Eitan & Behar, 2013). In these studies, the absorption was usually described by a neutral absorber intrinsic to the host galaxy. However, this is inconsistent with the significantly lower absorption seen at optical and UV wavelengths (see discussions in e.g. Cappi et al. 1997; Fabian et al. 2001a; Worsley et al. 2004a,b; Page et al. 2005). As a result, several studies thereafter preferred explaining the curvature with intrinsic spectral breaks (e.g. Tavecchio et al., 2007).

As shown in Eitan & Behar (2013), high redshift blazars, most of which are FSRQs, are often absorbed. Two recent studies by Arcodia et al. (2018) and Dalton et al. (2021) find that absorption in excess to the Galactic absorption, as opposed to intrinsic breaks, is preferred to fully explain the hardening in their respective samples of FSRQs. They successfully describe the excess X-ray absorption as occurring due to the highly ionized "warm-hot" intergalactic medium (WHIM), which would also account for the lack of absorption seen in the optical/UV. In their analyses, they directly model the WHIM and perform simultaneous fits with their sources to measure its properties. They both calculate mean hydrogen densities of $n_0 \sim 10^{-7}$ cm^{-3} (at $z = 0$) in the WHIM and temperatures of log(T/K)~6, which are consistent with the quantities expected of such a medium (see simulations in e.g. Cen & Ostriker 1999, 2006; Davé & Oppenheimer 2007; Schaye et al. 2015; Martizzi et al. 2019. Dalton et al. (2021) also combine their blazar data with that of gamma-ray bursts to find that their results agree over a wide range in redshift, and show that the WHIM column density is not related to variations in the flux or spectra of their sources.

The high signal to noise of the *NICER* data, combined with the broad bandwidth of including the BAT data, allow us to both measure curvature in the continuum and require "excess" absorption in PKS 2126-15. In other words, even with a more sophisticated treatment of the continuum of PKS 2126-15 (i.e. accounting for intrinsic curvature), we still require absorption that is consistent with the results of Arcodia et al. (2018) and Dalton et al. (2021). While such rigorous studies are beyond the scope of this chapter, excess absorption in the WHIM could be one way to interpret what we observe for PKS 2126-15 in the soft X-rays, given that it is a high-z FSRQ. Absorption in the intergalactic medium would not change over time, since it should not depend on the source's environment, and we observe a lack of variability in the column density at the redshift of PKS 2126-15, over many observations. While this of course does not present definitive evidence, it might point towards a scenario involving the WHIM. In addition, since the

WHIM is expected to be diffuse and smeared over redshift, it is possible for its signature to also appear at or near the redshift of the source. In the future, and especially with the arrival of the data from our new multi-cycle *NICER* campaign, we hope to robustly probe this scenario with more physically motivated models.

4.5 Conclusions

We have presented X-ray spectral and time-domain variability analyses of 4 "quiescent" blazars from the *Swift*-BAT catalog using *NICER* data from a recent 5-month long campaign, as well as archival BAT data. Our main results are as follows:

1. We detect statistically significant, but very low-amplitude ($F_{\rm var} < 25\%$) variations in the flux of our sources on three distinct timescales, which is at odds with the expected high-amplitude variability of blazars.

2. For each source, the fractional variability decreases with increasing timescale, in general showing low variability on monthly timescales ($F_{\rm var} \lesssim 13\%$), which is in tension with the "red noise" variability usually observed in AGN. This could imply a very constrained scenario where near-continuous particle injection balances the effects from energetic losses.

3. The minute-timescale variability appears to be characterized by non-stationary behavior involving long periods of quiescence with occasional bursts, with the latter possibly caused by processes similar to those that lead to ultra-fast flares.

4. As is customary with blazars, we are able to fit the broadband X-ray spectra with different power law models, with two sources that are well-described with a simple power law and

two sources that require curvature in the form of at least a log-parabola.

5. For PKS 2126-15, a high-z FSRQ, we require a column density significantly higher than that for Galactic absorption ($N_{\rm H,ex} \sim 10^{22}$ cm^{-2}). We posit that this may be due to a possible absorption contribution from the warm-hot intergalactic medium.

Chapter 5: Future Work

The work in this thesis represents only a small part of the type of research that can be conducted to study the variable emission from blazars and AGN. In this chapter, I outline a few avenues that can be taken in both the near and distant future that would expand on the research presented here.

5.1 Monitoring the variability of “quiescent” *Swift*-BAT blazars with *NICER*

One project for the immediate future involves a follow-up multi-cycle *NICER* campaign that would be a direct continuation of the study presented in Chapter 4. As mentioned in that chapter, the low-amplitude variability behavior observed in our sources may not be telling the entire story, since for instance some beamed AGN do exhibit emission that is mostly quiescent with occasional flaring events in the γ-rays, implying periods of relatively constant emission on yearly timescales until the source undergoes a flare with extreme variability. If this is also occurring in the X-rays for the blazars we have studied, we would not be able to notice such behavior using the first *NICER* campaign, since those observations only go out to monthly timescales.

We therefore proposed a multi-cycle monitoring campaign of these sources with *NICER* for 2 years, as well as of 2 additional faint, “quiescent” blazars as seen by the BAT, to determine whether or not these sources exhibit variability in the 0.3-10 keV band on yearly timescales.

We once again plan on combining these data with the BAT data for a variability analysis in the broadband, as well as utilizing them in an analysis of the spectral variability. This is an ongoing campaign that is currently still collecting data on the sample of 6 blazars proposed. The primary goals of this investigation would be to follow up on our previous campaign and determine, over a longer baseline, whether or not these sources are variable and by how much, to describe the form of the variability (e.g. rare flares or smooth long term changes), and to find a physical interpretation if we find that they indeed exhibit little or no variability.

5.2 Investigating the hard X-ray variability of AGN with *NuSTAR* and *Swift*-BAT

Another project for the near future involves data that was recently acquired from the *NuSTAR* observatory, and is comprised of a Fourier-based, frequency-domain timing analysis of blazar and non-blazar AGN from the BAT catalog. Fourier-based timing analyses of X-ray time series are extremely common and have been pivotal in understanding the variability behavior of both galactic black holes and AGN (see e.g. Nowak et al. 1999, Vaughan et al. 2003, and Uttley et al. 2014 for reviews). There are a few reasons these techniques are so popular in the analysis of time series. Firstly, the Fourier power spectral density function (PSD) clearly describes the dependence of variability on timescale (or temporal frequency), given that it measures the contribution to the total variance by each temporal frequency, and it is not difficult to model due to errors that are almost independent across frequency bins. Since Fourier techniques easily decompose data in terms of variations on different timescales, light curves do not have to be filtered by timescale beforehand. Furthermore, due to potentially fast variability, some of the relevant timescales in X-ray time series are on the order of minutes to hours, which implies that photon count rates will be limited. For this reason, it is at times more useful and insightful to turn to an analysis that directly tackles the stochastic nature of the variability.

As mentioned, the most basic and common tool used for these analyses is the PSD, defined as

$$P_n = \frac{2\Delta t}{\overline{x}^2 N}|X_n|^2, \tag{5.1}$$

where $\overline{x}$ is the mean of a particular time series, Δt the time bin, N the number of time bins, and X_n the discrete Fourier transform of the time series. The PSD above is written in the fractional rms-squared normalization, which allows for direct comparison of PSDs across different AGN and whose integral over a certain frequency band results in the fractional rms-squared variance (the square of F_{var}) of the timescales in question (see e.g. Miyamoto et al. 1991 and van der Klis 1997). Measurement errors introduce a level of variability that manifests itself as "white noise" that can cause the PSD to flatten at high frequencies. Vaughan et al. 2003 give the expected noise level as $P_{\mathrm{noise}} = \frac{2\Delta t \overline{\sigma_{\mathrm{err}}^2}}{\overline{x}^2}$, with $\overline{\sigma_{\mathrm{err}}^2}$ described as in Chapters 3 and 4.

Several studies have been able to measure PSDs for non-blazar AGN and have found that they are usually well-described by a broken power law, with $P \propto \nu^{-\alpha}$, where ν is the frequency, $\alpha \sim 1$ below a certain break frequency ν_b, and $\alpha \sim 2$ above the break frequency (Edelson & Nandra 1999; Uttley et al. 2002; Markowitz et al. 2003; McHardy et al. 2004; Uttley & McHardy 2005). In addition, correlations have been found between the timescale of the break frequency and the black hole mass and accretion rate (Markowitz et al. 2003; Kelly et al. 2011; McHardy et al. 2006; Körding et al. 2007), and as such the break frequency has come to be recognized as a vital quantity to describe accretion processes and specific timescales of accretion, such as the viscous timescale or specific orbital timescales for accreting matter (McHardy et al. 2006; González-Martín & Vaughan 2012; Smith et al. 2018). The fact that these correlations have also been found for galactic black holes (Papadakis 2004; Done & Gierliński 2005) and span the whole range of observed black hole masses suggests that this PSD property is important for all black hole accretion systems.

Other studies have analyzed the PSDs of blazars and beamed AGN, albeit in a different context. The emission and variability of blazars are generally associated with the non-thermal processes occurring in the jet, namely synchrotron emission and inverse Compton processes (see e.g. Ghisellini et al. 2017 and references therein). Past studies have found that, in general, the PSDs of blazars can be described by a simple power law with a slope of $\alpha \sim 2$ (Chatterjee et al. 2008; Abdo et al. 2010c). However, more recent studies suggest that the slope may depend on the process causing the emission, with e.g. Goyal et al. (2022) characterizing the variability of the synchrotron and inverse Compton components as red noise ($\alpha \sim 2$) and flicker noise ($\alpha \sim 1$), respectively. Furthermore, there is evidence that breaks in the PSDs of blazars are possible (e.g. Kataoka et al. 2001; Finke & Becker 2014; Chen et al. 2016; Chatterjee et al. 2018). These breaks could represent timescales related to the size of the emitting region in the jet, particle cooling, and particle escape (e.g. Finke & Becker 2014; Chen et al. 2016) and as such can provide insight into the nature of jetted processes, and they have been detected in the $\sim 10^{-6} - 10^{-5}$ Hz range in the X-rays (e.g. Kataoka et al. 2001; Chatterjee et al. 2018). In addition, some studies suggest that if potential emission from the disk is detected in a blazar (e.g. off-axis blazar-like AGN), then the PSD could have characteristics similar to those of non-blazar AGN, which could serve as a probe of the disk-jet connection (see e.g. Chatterjee et al. 2018).

While the aforementioned studies have been successful in characterizing the variability of AGN, the best X-ray data available in the vast majority of them was in the 2-10 keV band, which is susceptible to absorption in Seyferts, leading to a potential contribution to the variability from changes in the column density (absorption is not an issue for blazars). However, this does not need to be considered for energies $>$10 keV, as absorption will not obscure intrinsic emission at these energies. The *Swift*-BAT is the first instrument that provides data on long timescales at these energies.

In addition to the hard X-ray survey, the *Swift*-BAT monitors bright hard X-ray objects (over $\sim$1000 sources, $>9\sigma$ detection) on timescales of a day (Krimm et al. 2013) in the 15-50 keV band. While the hard X-ray survey mentioned in previous chapters focuses on combining data over many years of observation in order to detect as many AGN as possible and to generate time-averaged spectra of the sources, the transient monitor aims to detect flux variations from bright hard X-ray sources closer to real time, as opposed to over longer timescales. The BAT monitor observes 88% of the sky each day with a sensitivity of 5.3 mCrab for an observation with a 1-day duration, and with a time resolution of up to 64s (see Krimm et al. 2013 for more details on data processing and products). For column densities $\lesssim 10^{24}$ cm^{-2}, the 15-50 keV band of the BAT transient monitor is relatively unaffected by absorption and thus variability that is intrinsic to the source would remain.

Despite the benefits of the PSD, obtaining a broad-range PSD can be difficult due to a lack of data over sufficiently long timescales, and there are often gaps in timescale between the light curves that do exist. Shimizu & Mushotzky (2013) performed one of the first PSD analyses with BAT data using the 58-month catalog for 30 non-blazar AGN. They were able to fit most sources with an unbroken power law with $\alpha \sim 1$, which is consistent with PSDs at low frequencies from previous studies. However, they found that white noise dominated on timescales shorter than 5 days, so the analysis was restricted to a range spanning two orders of magnitude in frequency that was below $\sim 10^{-6}$ Hz, where breaks are expected to start to occur (e.g. Kataoka et al. 2001; Markowitz et al. 2003; McHardy et al. 2006; Rothschild et al. 2011; Chatterjee et al. 2018).

Given its much higher sensitivity per unit time compared to the BAT, and due to the fact that it has significant energy overlap with the BAT transient monitor (15-50 keV), *NuSTAR* would be able to push this analysis to higher frequencies. Due to the high sensitivity, *NuSTAR* can produce high-quality light curves extending to timescales of minutes. This data can be combined with data from the BAT to form a broadband PSD that covers ~ 5 orders of magnitude in frequency, which would in turn likely allow for a proper search of the break frequency, among other characteristics.

Before this project's inception, only ∼10 BAT AGN (∼3 blazars, ∼7 non-blazar) existed in the *NuSTAR* archive with enough observations to cover a wide range of timescales (the combined *NuSTAR* and BAT data for these 10 sources have not been published). Figure 5.1 (by Dr. Taro Shimizu) shows an example of what this analysis would look like using two sources that have enough archival data to make such a PSD construction and break frequency estimation possible, following procedures in e.g. Shimizu & Mushotzky (2013). While the vast majority of the 100 brightest BAT AGN indeed have *NuSTAR* observations, most of these observations are not sampled well enough to produce PSDs that will accurately determine the break frequency. I therefore proposed a recently accepted observing campaign for 4 bright *Swift*-BAT AGN (2 non-blazar, 2 blazars) with *NuSTAR* to allow for a calculation of the PSDs at higher frequencies, increasing the number of sources with adequate data to 14. The plan is to combine this short-timescale data with long-timescale archival *Swift*-BAT data in order to calculate a broadband PSD for each source and thus characterize the variability of what would be the first well-sampled light

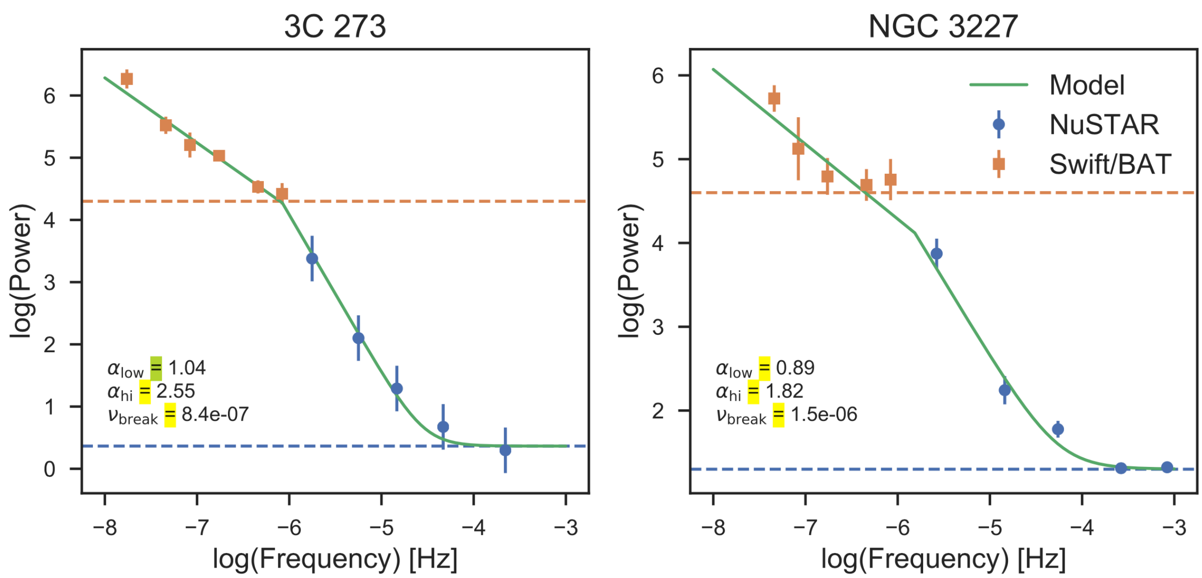

Figure 5.1: Examples of PSDs constructed with archival *NuSTAR* and BAT data by Dr. Shimizu, for 3C 273 and NGC 3227. The green line is a fit to the PSD to calculate the high and low frequency PSD slopes and the break frequency. White noise is represented by the dashed lines.

curves in the hard X-rays from timescales of minutes to 15 years.

While the proposed sample size is small, for the non-blazar AGN in our sample the total sample of sources would end up spanning $\sim$3 orders of magnitude in black hole mass as well as a significant range in Eddington ratio. The main goal would be to compare the results to the previous work done in the classical 2-10 keV band and see if the same correlations between ν_b and black hole mass and accretion rate exist in the 15-50 keV band for the relevant sources. In addition, certain studies (Zhou et al. 2010; Kelly et al. 2011, 2013) suggest that the black hole masses derived from the high-frequency PSD have potentially smaller uncertainty than those calculated using the $M_{\rm BH}$-σ relation or optical analyses involving broad emission lines. Therefore, this Fourier-based timing analysis could be instrumental for black hole mass estimation.

The project could also provide further insight into the nature of the variability of the non-thermal processes responsible for much of the X-ray emission of beamed AGN. For example, Goyal et al. (2022) recently found differences in the slopes of the PSDs produced by the synchrotron and inverse Compton components on timescales of decades to days. It would be interesting to investigate if the same differences in the PSDs hold at the higher frequencies probed by *NuSTAR*. Measurements of the break frequency for the blazars in our sample would involve characterizing the variability in the context of timescales related to energy losses (i.e. electron cooling) and electron escape that arise due to an emitting region located in the relativistic jet, which would improve our understanding of jet processes contributing to the hard-X-rays. It could also serve as a stepping stone for future studies of e.g. off-axis, blazar-like AGN and thus possibly probe the disk-jet connection.

5.3 Prospective Multi-wavelength Studies and Future X-ray Observatories

A step for the more distant future would be to extend some of the studies presented in this thesis to other wavelengths. In particular, it would be interesting to see if some of the results shown in Chapters 3 and 4 on the blazars that show little variability also hold in other energy bands. One possible starting point for such a project could make use of the copious amounts of long-term optical data from the Zwicky Transient Facility (ZTF, Bellm et al. 2019; Masci et al. 2019), which span nearly 4 years with measurements made every few days. The ZTF has over 2500 blazars in its database, and its archival data would be an ideal resource with which to enter into a multi-wavelength study of the long-timescale variability of the blazars studied in this thesis.

Figure 5.2 shows an example of the long-term optical variability (r and g bands generated with the SNAD ZTF viewer, Malanchev et al. 2023) for one of the blazars for which we detect low variability in the X-rays, PKS 2126-15. It is already evident from these light curves that

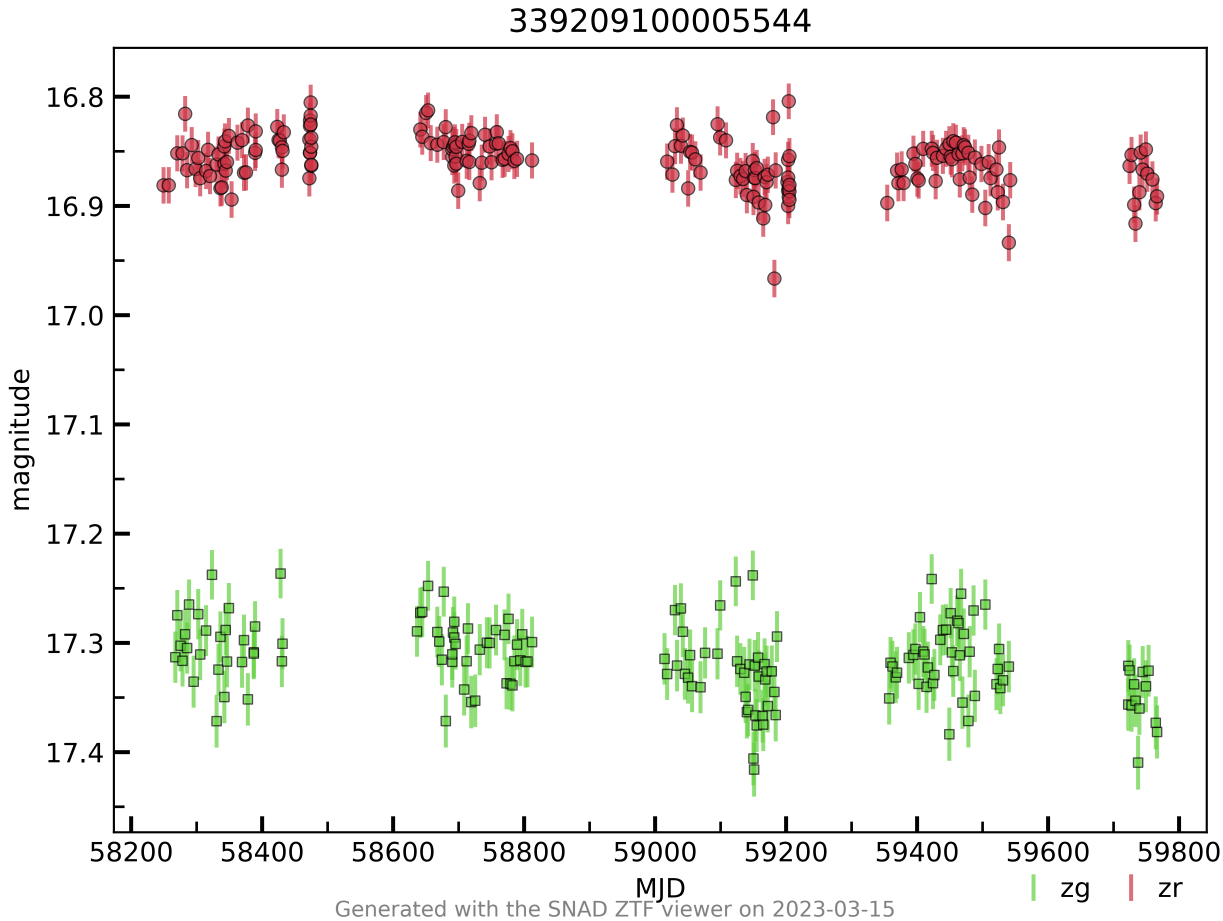

Figure 5.2: r and g band light curves for PKS 2126-15 showing low-amplitude variability for this source over a $\sim$4 year baseline.

this source also shows fairly low-amplitude variability in these optical bands, and it would be interesting if for some objects correlations in the variability were found between the optical and X-ray data. Another new direction in which to take the research would be to also directly compare the X-ray data from the blazars in this thesis with their respective γ-ray data and possibly perform cross-correlation analyses between the two energy bands. The $Fermi$-LAT catalog has detected over 3000 AGN in its first 8 years of operation, 98% of which are classified as blazars (Ajello et al. 2020). This database would therefore be yet another extremely useful resource to establish a more complete multi-wavelength picture of these objects.

Certain aspects of the research presented here would also be relevant to investigate with future X-ray telescopes. For instance, one branching avenue from Chapter 4 would involve using high-redshift blazars as a way to possibly probe the warm-hot intergalactic medium. The high-resolution spectroscopy from a telescope such as *XRISM* would be an extremely useful tool for this, as it would be able to resolve absorption features in the spectra of distant blazars that arise from intervening intergalactic media. In addition, simulations for the *Athena* observatory have already shown that absorption lines from ions in the WHIM can be detected in the spectra of GRB afterglows (Brand et al. 2016); these absorption features could also be searched for in the spectra of high-redshift FSRQs.

Appendix A: Appendix for Chapter 2

A.1 Checking for a potential absorption feature between 8 and 10 keV

The background spectrum reveals a peak that corresponds to the energies where we observe negative residuals (Figure A.1). This is likely the Cu-Kα complex in EPIC-pn, and our negative residuals are therefore the result of over-subtraction of these features. To be more thorough, we perform an exercise to make sure that the negative residuals are not the result of a physical absorption process. We fit the EPIC-pn spectrum, without the background subtracted, to a power law; in this case, if there is indeed absorption from an outflow, for instance, the residuals should remain negative, indicating that the feature is not just an artifact.

We show this spectrum in Figure A.2, and we find that the residuals are not present, suggesting that background over-subtraction is at fault. We also perform this exercise for our individual high and low-flux observations, and still the negative residuals do not show up. In addition, none of the individual MOS spectra show these residuals.

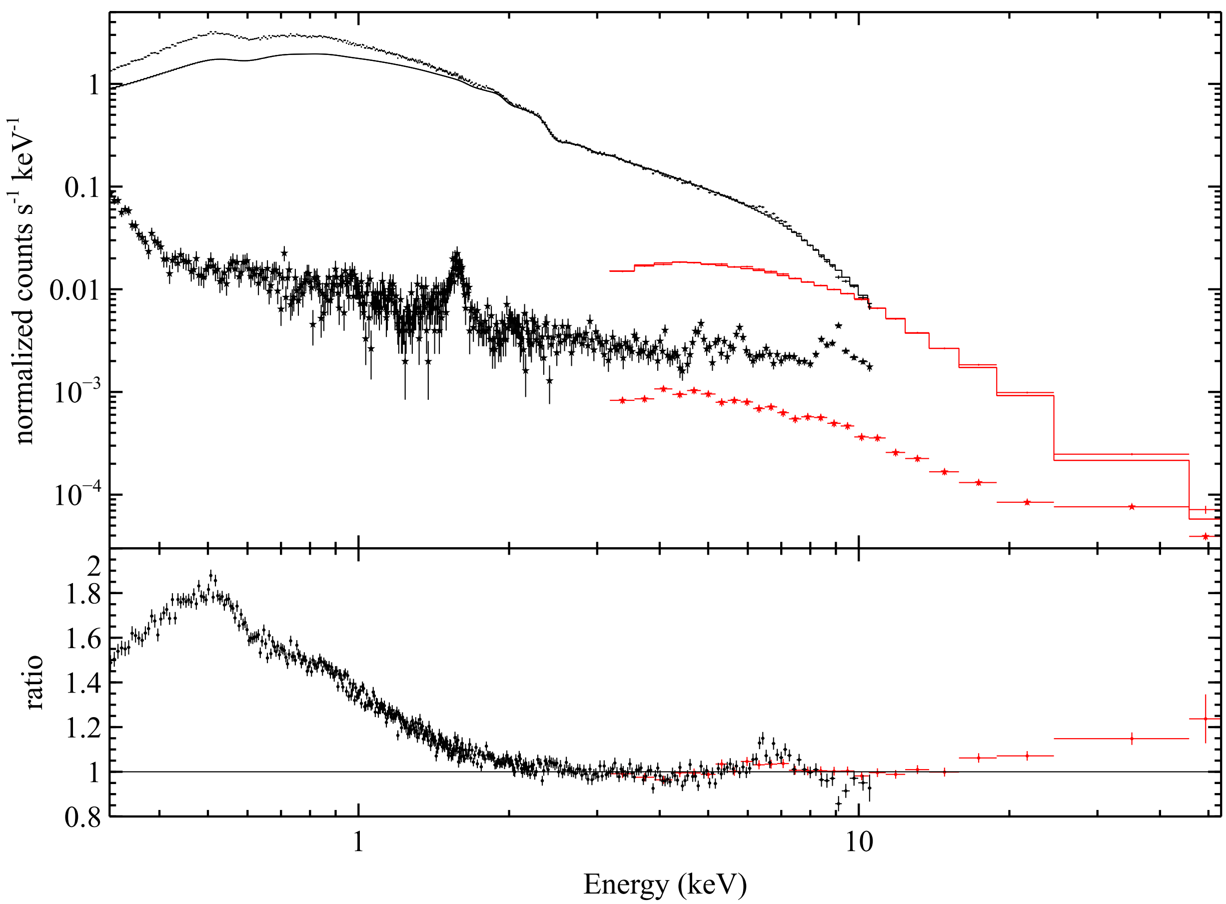

Figure A.1: 2-79 keV fit with a power law, extrapolated to lower energies. The corresponding background spectrum is also shown, with a peak at the same energies as our negative residuals.

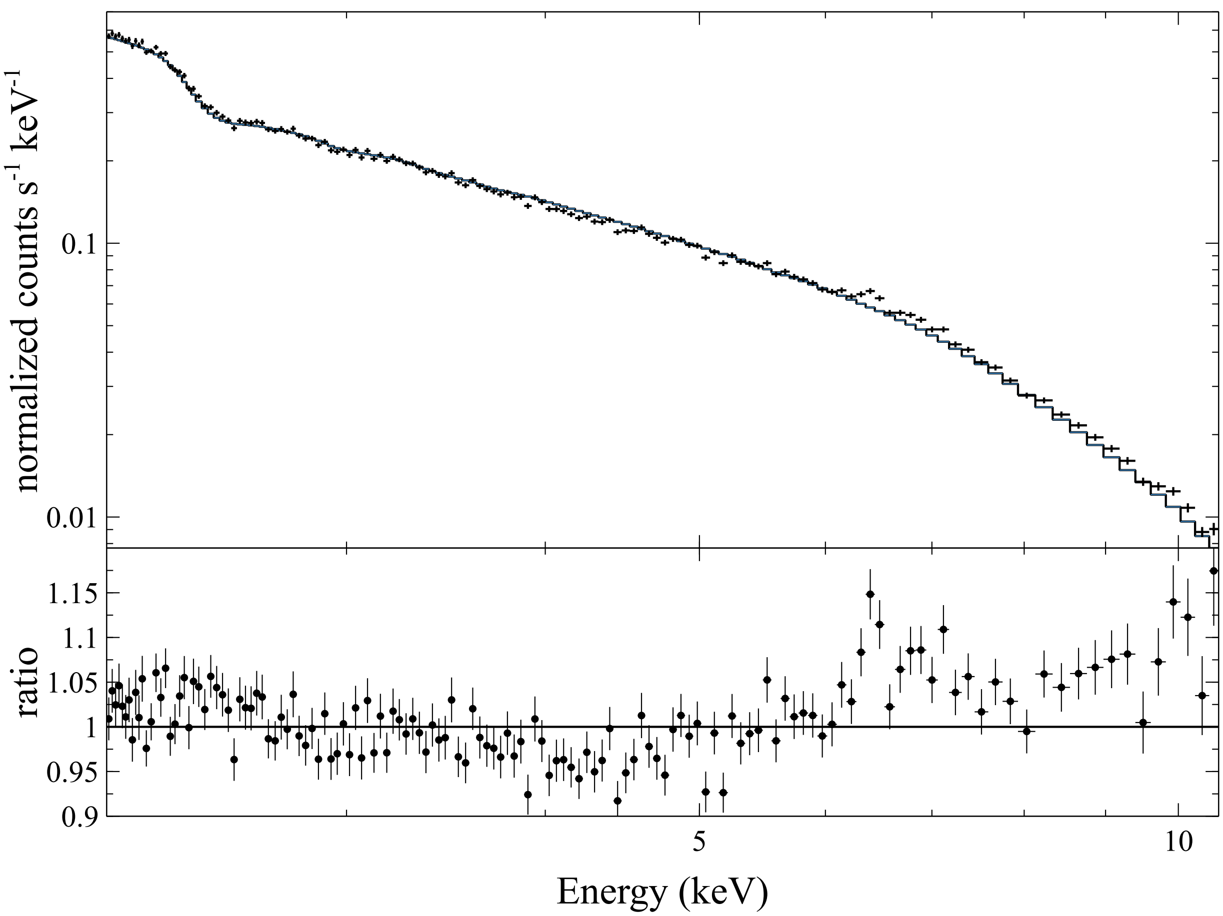

Figure A.2: 2-10 keV spectrum, with no background subtraction, fit to a power law. The negative residuals we observe in our main analysis are not present, suggesting that they are an artifact caused by background over-subtraction.

Bibliography

Abdo A. A., et al., 2009, , 707, L142

Abdo A. A., et al., 2010a, Science, 328, 725

Abdo A. A., et al., 2010b, , 716, 30

Abdo A. A., et al., 2010c, , 722, 520

Ajello M., et al., 2020, , 892, 105

Alston W. N., 2019, , 485, 260

Alston W. N., et al., 2019, , 482, 2088

Andruchow I., Romero G. E., Cellone S. A., 2005, A&A, 442, 97

Angel J. R. P., Stockman H. S., 1980, Ann. Rev. Astron. Astrophys, 18, 321

Arcodia R., Campana S., Salvaterra R., Ghisellini G., 2018, , 616, A170

Arnaud K. A., 1996, in Jacoby G. H., Barnes J., eds, Astronomical Society of the Pacific Conference Series Vol. 101, Astronomical Data Analysis Software and Systems V. p. 17

Astropy Collaboration et al., 2013, , 558, A33

Barr P., Mushotzky R. F., 1986, , 320, 421

Baumgartner W. H., Tueller J., Markwardt C. B., Skinner G. K., Barthelmy S., Mushotzky R. F., Evans P. A., Gehrels N., 2013, , 207, 19

Beckmann V., Shrader C. R., 2012, Active Galactic Nuclei

Begelman M. C., Blandford R. D., Rees M. J., 1984, Reviews of Modern Physics, 56, 255

Behar E., Dado S., Dar A., Laor A., 2011, , 734, 26

Bellm E. C., et al., 2019, , 131, 018002

Bhatta G., Mohorian M., Bilinsky I., 2018, , 619, A93

Bhattacharyya S., Bhatt H., Bhatt N., Singh K. K., 2014, , 440, 106

Blandford R. D., Rees M. J., 1978, Physica Scripta, 17, 265

Błażejowski M., Sikora M., Moderski R., Madejski G. M., 2000, , 545, 107

Brand T., et al., 2016, in den Herder J.-W. A., Takahashi T., Bautz M., eds, Vol. 9905, Space Telescopes and Instrumentation 2016: Ultraviolet to Gamma Ray. SPIE, p. 99055F, doi:10.1117/12.2234442, https://doi.org/10.1117/12.2234442

Butcher H. R., van Breugel W., Miley G. K., 1980, , 235, 749

Campana S., et al., 2012, , 421, 1697

Campana S., Salvaterra R., Ferrara A., Pallottini A., 2015, , 575, A43

Cappi M., Matsuoka M., Comastri A., Brinkmann W., Elvis M., Palumbo G. G. C., Vignali C., 1997, , 478, 492

Cen R., Ostriker J. P., 1999, , 514, 1

Cen R., Ostriker J. P., 2006, , 650, 560

Chand K., Gopal-Krishna 2022, arXiv e-prints, p. arXiv:2206.11938

Chatterjee R., et al., 2008, , 689, 79

Chatterjee R., et al., 2012, , 749, 191

Chatterjee R., Roychowdhury A., Chandra S., Sinha A., 2018, , 859, L21

Chen X., Pohl M., Böttcher M., Gao S., 2016, , 458, 3260

Comastri A., Fossati G., Ghisellini G., Molendi S., 1997, , 480, 534

Connors R. M. T., et al., 2019, , 882, 179

Costamante L., et al., 2001, , 371, 512

Crummy J., Fabian A. C., Gallo L., Ross R. R., 2006, , 365, 1067

D'Ammando F., et al., 2013, , 436, 191

Dalton T., Morris S. L., Fumagalli M., Gatuzz E., 2021, , 508, 1701

Dauser T., García J., Walton D. J., Eikmann W., Kallman T., McClintock J., Wilms J., 2016, , 590, A76

Davé R., Oppenheimer B. D., 2007, , 374, 427

De Marco B., Ponti G., Cappi M., Dadina M., Uttley P., Cackett E. M., Fabian A. C., Miniutti G., 2013, , 431, 2441

Deo R. P., Crenshaw D. M., Kraemer S. B., 2006, , 132, 321

Done C., Gierliński M., 2005, , 364, 208

Edelson R., Nandra K., 1999, , 514, 682

Edelson R., Turner T. J., Pounds K., Vaughan S., Markowitz A., Marshall H., Dobbie P., Warwick R., 2002, ApJ, 568, 610

Eitan A., Behar E., 2013, , 774, 29

Esposito V., Walter R., Jean P., Tramacere A., Türler M., Lähteenmäki A., Tornikoski M., 2015, , 576, A122

Event Horizon Telescope Collaboration et al., 2019, , 875, L1

Fabian A. C., 1979, Proceedings of the Royal Society of London Series A, 366, 449

Fabian A. C., Rees M. J., Stella L., White N. E., 1989, , 238, 729

Fabian A. C., Celotti A., Iwasawa K., McMahon R. G., Carilli C. L., Brandt W. N., Ghisellini G., Hook I. M., 2001a, , 323, 373

Fabian A. C., Celotti A., Iwasawa K., Ghisellini G., 2001b, , 324, 628

Fabian A. C., et al., 2009, , 459, 540

Feigelson E. D., et al., 1986, ApJ, 302, 337

Finke J. D., Becker P. A., 2014, , 791, 21

Foffano L., Prandini E., Franceschini A., Paiano S., 2019, , 486, 1741

Fossati G., Maraschi L., Celotti A., Comastri A., Ghisellini G., 1998, , 299, 433

Fuhrmann L., et al., 2016, Research in Astronomy and Astrophysics, 16, 176

Furniss A., Fumagalli M., Falcone A., Williams D. A., 2013, , 770, 109

GRAVITY Collaboration et al., 2020, , 643, A154

Gallo L. C., Tanaka Y., Boller T., Fabian A. C., Vaughan S., Brandt W. N., 2004, , 353, 1064

García J. A., Fabian A. C., Kallman T. R., Dauser T., Parker M. L., McClintock J. E., Steiner J. F., Wilms J., 2016, , 462, 751

Ghisellini G., 2013, Radiative Processes in High Energy Astrophysics. Springer International Publishing, doi:10.1007/978-3-319-00612-3, `https://doi.org/10.1007%2F978-3-319-00612-3`

Ghisellini G., Tavecchio F., 2009, , 397, 985

Ghisellini G., Tavecchio F., 2015, , 448, 1060

Ghisellini G., Tavecchio F., Bodo G., Celotti A., 2009a, , 393, L16

Ghisellini G., Maraschi L., Tavecchio F., 2009b, , 396, L105

Ghisellini G., Tavecchio F., Foschini L., Ghirlanda G., 2011, MNRAS, 414, 2674

Ghisellini G., Righi C., Costamante L., Tavecchio F., 2017, , 469, 255

Ghosh R., Dewangan G. C., Mallick L., Raychaudhuri B., 2018, , 479, 2464

Gierliński M., Done C., 2004, , 349, L7

González-Martín O., Vaughan S., 2012, , 544, A80

Goyal A., et al., 2022, , 927, 214

Gravity Collaboration et al., 2018, , 563, 657

Green A. R., McHardy I. M., Lehto H. J., 1993, , 265, 664

Grupe D., Mathur S., 2004, , 606, L41

Grupe D., Mathur S., Wilkes B., Elvis M., 2004, , 127, 1

Grupe D., Mathur S., Wilkes B., Osmer P., 2006, , 131, 55

HI4PI Collaboration et al., 2016, , 594, A116

Harris C. R., et al., 2020, Nature, 585, 357

Hayashida M., et al., 2015, , 807, 79

Ho L. C., 1999, , 516, 672

Hunter J. D., 2007, Computing in Science & Engineering, 9, 90

Jiang J., et al., 2018, , 477, 3711

Jiang J., et al., 2019, , 489, 3436

Jorstad S. G., et al., 2005, The Astronomical Journal, 130, 1418

Kalberla P. M. W., Burton W. B., Hartmann D., Arnal E. M., Bajaja E., Morras R., Pöppel W. G. L., 2005, , 440, 775

Kapanadze B., Gurchumelia A., 2022, , 668, A75

Kara E., Miller J. M., Reynolds C., Dai L., 2016, , 535, 388

Kara E., García J. A., Lohfink A., Fabian A. C., Reynolds C. S., Tombesi F., Wilkins D. R., 2017, , 468, 3489

Kataoka J., et al., 2001, , 560, 659

Kataoka J., Tanihata C., Kawai N., Takahara F., Takahashi T., Edwards P. G., Makino F., 2002, , 336, 932

Kelly B. C., Sobolewska M., Siemiginowska A., 2011, , 730, 52

Kelly B. C., Treu T., Malkan M., Pancoast A., Woo J.-H., 2013, , 779, 187

Körding E. G., Migliari S., Fender R., Belloni T., Knigge C., McHardy I., 2007, , 380, 301

Krimm H. A., et al., 2013, , 209, 14

Kubo H., Takahashi T., Madejski G., Tashiro M., Makino F., Inoue S., Takahara F., 1998, , 504, 693

Kynoch D., et al., 2018, , 475, 404

Landt H., et al., 2017, , 464, 2565

Leighly K. M., O'Brien P. T., 1997, , 481, L15

Lichti G. G., et al., 2008, A&A, 486, 721

Lister M. L., et al., 2013, , 146, 120

Lu Y., Yu Q., 2001, , 324, 653

Lynden-Bell D., 1969, , 223, 690

Madsen K. K., et al., 2015, , 812, 14

Malanchev K., et al., 2023, , 135, 024503

Mallick L., et al., 2018, , 479, 615

Marinucci A., et al., 2014, , 440, 2347

Markowitz A., Edelson R., 2004, , 617, 939

Markowitz A., et al., 2003, , 593, 96

Marscher A. P., Gear W. K., 1985, , 298, 114

Marshall H. L., et al., 2005, , 156, 13

Martizzi D., et al., 2019, , 486, 3766

Masci F. J., et al., 2019, , 131, 018003

Massaro E., Perri M., Giommi P., Nesci R., 2004, , 413, 489

Massaro E., Tramacere A., Perri M., Giommi P., Tosti G., 2006, , 448, 861

Massaro E., Giommi P., Leto C., Marchegiani P., Maselli A., Perri M., Piranomonte S., Sclavi S., 2009, , 495, 691

Massaro E., Maselli A., Leto C., Marchegiani P., Perri M., Giommi P., Piranomonte S., 2015, , 357, 75

McHardy I. M., Papadakis I. E., Uttley P., Page M. J., Mason K. O., 2004, , 348, 783

McHardy I. M., Koerding E., Knigge C., Uttley P., Fender R. P., 2006, , 444, 730

McKinney J. C., Dai L., Avara M. J., 2015, , 454, L6

Miyakawa T., Ebisawa K., Inoue H., 2012, , 64, 140

Miyamoto S., Kimura K., Kitamoto S., Dotani T., Ebisawa K., 1991, , 383, 784

Mizumoto M., Ebisawa K., Sameshima H., 2014, , 66, 122

Morini M., Chiappetti L., Maccagni D., Maraschi L., Molteni D., Tanzi E. G., Treves A., Wolter A., 1986, ApJ Letters, 306, L71

Mundo S. A., Mushotzky R., 2023, , 520, 1044

Mushotzky R. F., Done C., Pounds K. A., 1993, , 31, 717

Mutel R. L., Phillips R. B., Su B., Bucciferro R. R., 1990, ApJ, 352, 81

Nandra K., George I. M., Mushotzky R. F., Turner T. J., Yaqoob T., 1997, ApJ, 476, 70

Nowak M. A., Vaughan B. A., Wilms J., Dove J. B., Begelman M. C., 1999, , 510, 874

Oh K., et al., 2018, , 235, 4

Ojha V., Chand H., Dewangan G. C., Rakshit S., 2020, , 896, 95

Osterbrock D. E., Pogge R. W., 1985, , 297, 166

Page K. L., Reeves J. N., O'Brien P. T., Turner M. J. L., 2005, , 364, 195

Paggi A., Massaro F., Vittorini V., Cavaliere A., D'Ammando F., Vagnetti F., Tavani M., 2009, , 504, 821

Paliya V. S., Sahayanathan S., Parker M. L., Fabian A. C., Stalin C. S., Anjum A., Pandey S. B., 2014, , 789, 143

Paliya V. S., Sahayanathan S., Stalin C. S., 2015, , 803, 15

Paliya V. S., Parker M. L., Jiang J., Fabian A. C., Brenneman L., Ajello M., Hartmann D., 2019a, , 872, 169

Paliya V. S., et al., 2019b, , 881, 154

Paliya V. S., Domínguez A., Ajello M., Franckowiak A., Hartmann D., 2019c, , 882, L3

Pan H.-W., Yuan W., Yao S., Komossa S., Jin C., 2018, , 866, 69

Pandey A., Gupta A. C., Wiita P. J., 2017, , 841, 123

Papadakis I. E., 2004, , 348, 207

Papadakis I. E., McHardy I. M., 1995, , 273, 923

Peterson B. M., et al., 2000, , 542, 161

Pian E., 2002, , 19, 49

Ponti G., Papadakis I., Bianchi S., Guainazzi M., Matt G., Uttley P., Bonilla N. F., 2012, , 542, A83

Rajput B., Stalin C. S., Rakshit S., 2020, , 634, A80

Rani B., et al., 2013, , 552, A11

Rani P., Stalin C. S., Rakshit S., 2017, , 466, 3309

Rani B., Mundo S. A., Mushotzky R., Lien A. Y., Gurwell M. A., Kim J. Y., 2022, , 932, 104

Remillard R. A., et al., 2022, , 163, 130

Reynolds C. S., Nowak M. A., 2003, , 377, 389

Rodrigues X., Garrappa S., Gao S., Paliya V. S., Franckowiak A., Winter W., 2021, , 912, 54

Rothschild R. E., Markowitz A., Rivers E., Suchy S., Pottschmidt K., Kadler M., Müller C., Wilms J., 2011, , 733, 23

Saito S., Stawarz Ł., Tanaka Y. T., Takahashi T., Madejski G., D'Ammando F., 2013, , 766, L11

Sambruna R. M., Chou L. L., Urry C. M., 2000, , 533, 650

Sambruna R. M., Tavecchio F., Ghisellini G., Donato D., Holland S. T., Markwardt C. B., Tueller J., Mushotzky R. F., 2007, , 669, 884

Sari R., Narayan R., Piran T., 1996, , 473, 204

Saxton R., Read A., Esquej P., Miniutti G., Alvarez E., 2011, in Foschini L., Colpi M., Gallo L., Grupe D., Komossa S., Leighly K., Mathur S., eds, Narrow-Line Seyfert 1 Galaxies and their Place in the Universe. p. 8, doi:10.22323/1.126.0008

Sbarrato T., et al., 2016, , 462, 1542

Sądowski A., Narayan R., 2015, , 453, 3213

Schaye J., et al., 2015, , 446, 521

Scott D. W., 1992, Multivariate Density Estimation

Shakura N. I., Sunyaev R. A., 1973, , 24, 337

Shimizu T. T., Mushotzky R. F., 2013, , 770, 60

Sikora M., Begelman M. C., Rees M. J., 1994, , 421, 153

Sikora M., Madejski G., Moderski R., Poutanen J., 1997, , 484, 108

Sikora M., Stawarz Ł., Moderski R., Nalewajko K., Madejski G. M., 2009, , 704, 38

Smith K. L., Mushotzky R. F., Boyd P. T., Malkan M., Howell S. B., Gelino D. M., 2018, , 857, 141

Soldi S., et al., 2008, , 486, 411

Soldi S., et al., 2014, A&A, 563, A57

Spada M., Ghisellini G., Lazzati D., Celotti A., 2001, , 325, 1559

Starling R. L. C., Willingale R., Tanvir N. R., Scott A. E., Wiersema K., O'Brien P. T., Levan A. J., Stewart G. C., 2013, , 431, 3159

Stawarz Ł., 2004, , 613, 119

Stein W. A., Odell S. L., Strittmatter P. A., 1976, Ann. Rev. Astron. Astrophys, 14, 173

Steiner J. F., García J. A., Eikmann W., McClintock J. E., Brenneman L. W., Dauser T., Fabian A. C., 2017, , 836, 119

Stickel M., Padovani P., Urry C. M., Fried J. W., Kuehr H., 1991, ApJ, 374, 431

Takahashi T., et al., 1996, , 470, L89

Tammi J., Duffy P., 2009, , 393, 1063

Tanaka Y., Boller T., Gallo L., Keil R., Ueda Y., 2004, , 56, L9

Tavecchio F., Ghisellini G., 2008, , 386, 945

Tavecchio F., et al., 2000, , 543, 535

Tavecchio F., Maraschi L., Ghisellini G., Kataoka J., Foschini L., Sambruna R. M., Tagliaferri G., 2007, , 665, 980

Tavecchio F., Ghisellini G., Ghirlanda G., Costamante L., Franceschini A., 2009, , 399, L59

Thomsen L. L., Lixin Dai J., Ramirez-Ruiz E., Kara E., Reynolds C., 2019, , 884, L21

Tomsick J. A., et al., 2018, , 855, 3

Tueller J., Mushotzky R. F., Barthelmy S., Cannizzo J. K., Gehrels N., Markwardt C. B., Skinner G. K., Winter L. M., 2008, ApJ, 681, 113

Tueller J., et al., 2010, , 186, 378

Ulrich M.-H., Maraschi L., Urry C. M., 1997, , 35, 445

Urry C. M., Padovani P., 1995, , 107, 803

Urry C. M., Sambruna R. M., Worrall D. M., Kollgaard R. I., Feigelson E. D., Perlman E. S., Stocke J. T., 1996, , 463, 424

Uttley P., McHardy I. M., 2001, , 323, L26

Uttley P., McHardy I. M., 2005, , 363, 586

Uttley P., McHardy I. M., Papadakis I. E., 2002, , 332, 231

Uttley P., McHardy I. M., Vaughan S., 2005, , 359, 345

Uttley P., Cackett E. M., Fabian A. C., Kara E., Wilkins D. R., 2014, , 22, 72

Vasudevan R. V., Fabian A. C., 2007, , 381, 1235

Vaughan S., Edelson R., Warwick R. S., Uttley P., 2003, , 345, 1271

Vermeulen R. C., Cohen M. H., 1994, ApJ, 430, 467

Verner D. A., Ferland G. J., Korista K. T., Yakovlev D. G., 1996, , 465, 487

Virtanen P., et al., 2020, Nature Methods, 17, 261

Wagner S. J., Witzel A., 1995, Ann. Rev. Astron. Astrophys, 33, 163

Walton D. J., Nardini E., Fabian A. C., Gallo L. C., Reis R. C., 2013, , 428, 2901

Wilkins D. R., Gallo L. C., 2015, , 448, 703

Williamson K. E., et al., 2014, , 789, 135

Wilms J., Allen A., McCray R., 2000, , 542, 914

Woo J.-H., Urry C. M., 2002, , 579, 530

Woo J.-H., Urry C. M., van der Marel R. P., Lira P., Maza J., 2005, , 631, 762

Worrall D. M., Wilkes B. J., 1990, , 360, 396

Worsley M. A., Fabian A. C., Turner A. K., Celotti A., Iwasawa K., 2004a, , 350, 207

Worsley M. A., Fabian A. C., Celotti A., Iwasawa K., 2004b, , 350, L67

Worsley M. A., Fabian A. C., Pooley G. G., Chandler C. J., 2006, , 368, 844

Yao S., Yuan W., Komossa S., Grupe D., Fuhrmann L., Liu B., 2015, , 150, 23

Zhang Y.-H., 2011, , 726, 21

Zhang Y. H., Treves A., Celotti A., Qin Y. P., Bai J. M., 2005, , 629, 686

Zhang Y. H., Bai J. M., Zhang S. N., Treves A., Maraschi L., Celotti A., 2006, , 651, 782

Zhou H., et al., 2007, , 658, L13

Zhou X.-L., Zhang S.-N., Wang D.-X., Zhu L., 2010, , 710, 16

van der Klis M., 1997, in Babu G. J., Feigelson E. D., eds, Statistical Challenges in Modern Astronomy II. p. 321 (`arXiv:astro-ph/9704273`), doi:10.48550/arXiv.astro-ph/9704273